Eulerian Formulation of Spatially Constrained Elastic Rods

A DISSERTATION SUBMITTED TO
THE FACULTY OF THE GRADUATE SCHOOL
OF THE UNIVERSITY OF MINNESOTA
AND TO
THE FACULTÉ DES SCIENCES APPLIQUÉES
OF THE UNIVERSITÉ DE LIÈGE BY

Alexandre Huynen

IN PARTIAL FULFILLMENT OF THE REQUIREMENTS
FOR THE DEGREE OF
DOCTOR OF PHILOSOPHY
AND
DOCTOR IN ENGINEERING SCIENCES

Co-Advisors
Emmanuel Detournay, Vincent Denoël

November, 2015

Examining committee

Olivier Brüls (President)
Professor of Mechanical Engineering, Université de Liège

Vincent Denoël (Co-Advisor)
Associate Professor of Structural Engineering, Université de Liège

Emmanuel Detournay (Co-Advisor)
Professor of Civil Engineering, University of Minnesota

Jean-François Demonceau
Senior Researcher, Université de Liège

Yoichiro Mori
Associate Professor of Mathematics, University of Minnesota

Henryk Stolarski
Professor of Civil Engineering, University of Minnesota

Abstract

Slender elastic rods are ubiquitous in nature and technology. For a vast majority of applications, the rod deflection is restricted by an external constraint and a significant part of the elastic body is in contact with a stiff constraining surface. The research work presented in this doctoral dissertation formulates a computational model for the solution of elastic rods constrained inside or around frictionless tube-like surfaces.

The segmentation strategy adopted to cope with this complex class of problems consists in sequencing the global problem into, comparatively simpler, elementary problems either in continuous contact with the constraint or contact-free between their extremities. Within the conventional Lagrangian formulation of elastic rods, this approach is however associated with two major drawbacks. First, the boundary conditions specifying the locations of the rod centerline at both extremities of each elementary problem lead to the establishment of isoperimetric constraints, *i.e.*, integral constraints on the unknown length of the rod. Second, the assessment of the unilateral contact condition requires, in principle, the comparison of two curves parametrized by distinct curvilinear coordinates, *viz.* the rod centerline and the constraint axis. Both conspire to burden the computations associated with the method. To streamline the solution along the elementary problems and rationalize the assessment of the unilateral contact condition, the rod governing equations are reformulated within the Eulerian framework of the constraint. The methodical exploration of both types of elementary problems leads to specific formulations of the rod governing equations that stress the profound connection between the mechanics of the rod and the geometry of the constraint surface.

The proposed Eulerian reformulation, which restates the rod local equilibrium in terms of the curvilinear coordinate associated with the constraint axis, describes the rod deformed configuration by means of either its relative position with respect to the constraint axis (contact-free segments) or its angular position on the constraint surface (continuous contacts.) This formulation circumvents both drawbacks that afflict the conventional Lagrangian approach associated with the segmentation strategy. As the a priori unknown domain, *viz.* the rod length, is substituted for the known constraint axis, the free boundary problem and the associated isoperimetric constraints are converted into a classical two-point boundary value problem. Additionally, the description of the rod deflection by means of its eccentricity with respect to the constraint axis trivializes the assessment of the unilateral contact condition. Along continuous contacts, this formulation expresses the strain variables, measuring the rod change of shape, in terms of the geometric invariants of the constraint surface, and emphasizes the influence of the constraint local geometry on the reaction pressure.

Formalizing the segmentation strategy, a computational model that exploits the Eulerian formulation of the rod governing equations is devised. To solve the quasi-static deflection of elastic rods constrained inside or around a tube-like surface, this computational model identifies the number of contacts, their nature (either discrete or continuous), and the rod configuration at the connections that satisfies the unilateral contact condition and preserves the rod integrity along the sequence of elementary problems.

Keywords elastic rod, elastica, unilateral contact, surface constraint, Eulerian parameterization, torque-and-drag, angioplasty, endoscopy

Acknowledgements

First and foremost, I am grateful to my advisors, Vincent Denoël and Emmanuel Detournay, for their confidence and the complete liberty they have granted me to conduct this research. Despite their busy agendas, they always had time for guidance and suggestions (well, most of the time.) Your high scientific standards and hard work set an example, the productive but always convivial atmosphere you established made me feel a friend. For that, I thank you.

I wish to convey my gratitude to the members of the examining committee for accepting the invitation to review my research work and their participation to my thesis defense. Hopefully, they will appreciate this manuscript and find its reading stimulating.

There are many people that have earned my gratitude for their contribution to my time in graduate school: colleagues, friends and family members. More particularly, I am beholden to Catalina, Julien and Luc with whom I shared sometimes an office, sometimes a house but most often laughs and coffees during the cold winters in Minneapolis. I am also indebted to Benjamin, Nicolas and Thomas. Since my return in Belgium, I have always looked forward to our Monday lunches punctuated by our ardent conversations, scientific or not. Nico, your humour and perpetual enthusiasm greatly contributed to make the redaction of this document less tedious, enjoyable even. We started classmates, became officemates, I am now proud to say that we are mates.

A particular thanks to my parents and my brother for their love, unconditional support and encouragements in all my endeavors. Maman, Papa, merci pour votre soutien, votre tendresse et votre amour mais surtout pour avoir fait de moi ce que je suis aujourd'hui.

As it is custom to save the best for last, I conclude this note by expressing my deepest acknowledgement to my fiancée and best friend, Oriane, for her love, patience and understanding. You have been with me all this years and shared all of the ups and downs of my research, I could never have accomplished this dissertation without your support. Finally, thank you for keeping me sane over the past few months.

This research would not have been possible without the financial assistance of the Fund for Training and Research in Industry and Agriculture (FRIA, F.R.S. – FNRS), Brussels, Belgium.

Contents

List of Figures

List of Algorithms

Chapter I

Introduction

I.1 Constrained deformation of elastic rods

A wide scope of disciplines ranging from biology to medical sciences and engineering is concerned with the deformation of slender elastic structures. For a vast majority of applications, these flexible structures are however restrained inside or outside constraints of various shapes and lengths. Kilometers-long drillstrings are, for instance, commonly operated in the oil and gas industry to transmit the drilling forces to the bottom of boreholes that are only a few centimeters wider than the pipes (Inglis, 1988; Sampaio, 2008). Related to the medical field and therefore concerned with much smaller dimensions, the endoscopic examination of internal organs (e.g. colonoscopy, fibroscopy, rhinoscopy) as well as the treatment of vascular and cerebrovascular pathologies through angioplasty (e.g. abdominal and thoracic aortic aneurism, stroke) or stenting (Schneider, 2003) constitute further applications of this broad class of problems. Even smaller, crumpling and wrinkling of long molecular chains inside cavities emerges in biology (Donato et al., 2003; Gomes et al., 2008) as DNA filaments are densely packed in viral capsids or cell nucleus (LaMarque et al., 2004; Odijk, 2004; Travers and Thompson, 2004; Stoop et al., 2011). Other applications involve the non-destructive inspection of ducts or other pipe systems by means of industrial endoscope (e.g. borescope or fiberscope), the insertion of artificial fibers in industrial crimpers (Cooke, 2000), or the dissipation of energy through the progressive buckling and folding of a flexible beam that is laterally confined inside a rigid enclosure (Chai, 2002, 2006).

The constraint may alternatively work as a support for the elastic structure. Driven by internal and/or external forces, it may then be coiled/wound around another slender body as in the wrapping of DNA around histone cores (Swigon et al., 1998; Tobias et al., 2000; da Fonseca and de Aguiar, 2003) or carbon nanotubes (Tu et al., 2009). Twining plants, which achieve vertical growth through the friction generated by revolving around poles or other supports (Goriely and Neukirch, 2006; Goriely et al., 2008), constitute a further natural manifestation of

this general problem.

Despite spanning multiple disciplines and lengthscales, these phenomena share fundamental features that legitimate their modeling through the rod theory. Observation and simulation indeed reveal that, in most circumstances, the transverse dimensions of the elastic structure may be disregarded with respect to its length and the constraint dimensions. The slender structure then reduces to a one-dimensional elastic body that will henceforth be generically referred to as a *rod*. Although this thin rod may suffer large deflections or large rotations, the strains generally remain small over its entire length. Due to the presence of the constraint, the rod is subjected to a unilateral contact condition, which ensures that, depending on the context, it remains either inside or outside the constraining surface. Hence, a significant part of the rod usually contacts the constraint and the global solution considerably reflects the geometry of the constraint. Additionally, along contacts, the constraining surface exerts on the rod an *a priori* unknown reaction force and, potentially, a tangential friction force. These forces as well as the position and number of contacts are of key concern to most applications listed here and collected under the *constrained elastic rods* denomination.

I.1.1 Motivations

Clearly, this class of problems encompasses a wealth of fascinating applications, each associated with its own scientific and economic challenges. Specifically, the necessity to drill deeper and more complex well profiles as well as the realization of extended reach boreholes lead the oil and gas industry to develop means to evaluate the transmission of forces from the rig to the bit. This question, known as the *torque-and-drag problem*, plays an essential role in drilling and well design as the friction appearing at the contacts between the drillstring and the borehole may dramatically increase the costs or, even, be a limiting factor in some configurations. The completion of deviated wells with up to 10 kilometers of horizontal reach, as presently achieved, may indeed lead to a considerable increase of the surface torque required at the rig to overcome the frictional effects and rotate the entire drillstring together with the bit at its bottom. In extreme situations, these frictional effects may even lead to serious well damages, drillstring failures or other catastrophic issues (Macdonald and Bjune, 2007). As the extremely low data-rates achieved through mud-pulse telemetry[1] prevent the transmission of comprehensive information and measures from the bit to the rig, the drilling conditions at the bottom of the borehole generally remain unknown until the drillstring is pulled out the well to replace the bit or other piece of the drillstring. Hence, to track a predefined well path and limit the borehole tortuosity, the driller relies on its training as well as the accuracy of models predicting the drilling tendency (Perneder and Detournay, 2013; Marck et al., 2014). Oilfield drilling operations being extremely costly, the accurate prediction as well as the real-time simulation and analysis of the forces involved therefore became a crucial issue for the oil and gas industry in the last decades.

[1] Although considerably higher data-rates may be achieved with wired drillpipe, also referred to as wireline, mud-pulse telemetry is the most common method of data transmission.

Interestingly, the medical field is confronted with sensibly similar challenges. In particular, percutaneous coronary intervention, commonly known as coronary angioplasty, is an endovascular procedure requiring only a small incision to treat coronary arteries stenosis. During this minimally invasive surgery, a guiding catheter and a guidewire are introduced in a major blood vessel, typically the femoral artery. The guidewire, which is an extremely thin wire designed to undergo large deformations and remain perfectly elastic, is then guided by a cardiologist through the coronary artery to the site of the stenosis or blockage and, eventually, passed across. An angioplasty catheter is then slid over the guidewire, which acts as a pathway to the stenosis, and a balloon is inflated in order to stretch the artery wall open and restore blood flow to the heart muscle; a stent may or may not be implanted at the time of ballooning to prop the vessel open. The balloon is then deflated, possibly leaving the stent to support the new stretched open position of the artery (Morgan and Walser, 2010). Considering that the physician has exclusively access to the proximal end of the guidewire, its insertion into the coronary artery requires considerable efforts and, certainly, core skills. Relying on radiographic snapshots of the guidewire configuration in the patient's blood vessels, the physician has indeed to thread this device through narrow passageways by only pushing/pulling, twisting or rotating its end (Schneider, 2003; Baim, 2005). As any others surgical interventions, this procedure is not devoid of risks and the rigorous training of the physician is of paramount importance. To this end, procedural simulators providing hands-on practice without consequence to the patient safety have recently flourished. Similarly, to reduce the recurrent exposition of physicians to X-rays (Smilowitz et al., 2013) and their noxious effects, the appeal for telesurgery and robotically-assisted surgery has increasingly been growing[2] . To effectively mimic actual clinical conditions and develop haptic interfaces providing physicians with realistic tactile feedback, considerable efforts have been dedicated to the analysis of how guidewires interact and deform within arteries as well as how forces are carried along their length.

The discovery of the double-helical structure of DNA by Watson and Crick (1953), based on the experimental work by R. Franklin and R. Gosling (Watson, 2010), transformed the foundations of biology and medicine. The knowledge about this extremely long biopolymer, its properties and function, has been constantly growing ever since. With the advent of disciplines such as molecular biology and genetic engineering, questions about the geometrical and mechanical states of DNA inside the cell of a living organism became crucial. To fit inside viral capsids or cell nucleus, DNA filaments are necessarily tightly bent and folded (with length compaction factors up to 10^4) yielding large elastic deformation energies. The associated packing/unpacking processes are, for instance, known to control the production of proteins, promote genetic recombination and regulate gene expression by bringing the sites into close spatial proximity (Travers and Thompson, 2004). In eukaryotic cells, the nuclear DNA is wrapped around histone cores to form chromatin. The determination of its configuration along these cores is therefore essential

[2] At the time of writing these lines, the U.S. Food and Drug Administration approved a device that performs robotic angioplasty in the optic of reducing radiation for cardiologists (Hicks, 2015).

to the understanding of intricate multilevel folding and its biological functions in replication and transcription (Yang and Couchman, 1997). Additionally, because a typical DNA molecule consists of two complementary polynucleotide chains that are multiply interwound, its topological properties (*e.g.* knotting, catenation, supercoiling, etc.) profoundly influence most genetic processes (Deweese et al., 2008).

To gain understanding of these real-world phenomena, mathematical models have been elaborated by scientists and engineers. This task, often iterative, is destined to provide a representation of the essential features of a system from the *actual world* in terms of mathematical concepts or ideas. Breaking up the complexity of the system under consideration, the resulting mathematical models are then used as explicative or predictive tools to answer questions about the system. For constrained elastic rods, the ubiquitous question concerns the transmission of the internal forces along the rod and how contacts with the constraint, continuous and discrete, affect this transmission. Besides the absolute joy resulting from formulating and solving mathematical problems, the underlying objective is to provide a methodology for the prediction and simulation of the rod configuration restrained inside or outside a constraint. The quality and clarity of a model involving a trade-off between simplicity and accuracy, the identification of the degree of abstraction and complexity required to capture the essential features of the real-world phenomenon under consideration is a fundamental step conditioned by the objectives of the model.

I.1.2 Objectives

The general class of problems collected under the *constrained elastic rods* denomination is extraordinarily broad and complex as it may involve a multitude of intricate effects such as deformation of the constraint due to contacts, vibration of the rod or time-varying definition of the constraint. We are not aiming at resolving all the aspects of this generic question but desire to significantly contribute to the modeling and understanding of a particular subclass applicable to the torque-and-drag problem experienced by the drilling industry and, to some extent, to the simulation of minimally invasive medical interventions. The mechanics of DNA packing involving numerous additional details and specific features, this aspect of constrained elastic rods is only superficially tackled in this study.

The main objective of the present research consists in the development of a versatile computational model that resolves the quasi-static deflection of an elastic rod inside or around a perfectly rigid sinuous conduit under various loading and boundary conditions. The formulation of such a model is a significant task requiring the construction of an algorithm that performs *(i)* the identification of the number of contacts and their nature, *viz.* either discrete or continuous, *(ii)* the determination of the positions of these contacts along the constraint, and *(iii)* the determination of the rod configuration along continuous contacts and between two neighboring contacts. Additionally, as the loading applied to the rod or its boundary conditions evolve,

one must consider multiple configurations and transitions including, among others, the emergence/disappearance of contacts, the passage from discrete to continuous contacts as well as its reciprocal, or the merging of two contacts. The resulting algorithm should, for instance, be able to treat insertion/extraction problems in which a thin rod is introduced in or withdrawn from a tortuous conduit of known geometry. The output should include the precise description of the contacts along the conduit as well as the rod configuration between contacts, the reactions arising from both continuous and discrete contacts with the constraint and how they affect the transmission of the internal forces along the rod.

As emphasized in the following Section, conventional tools such as the finite element method generally result in computational times unsuitable for real-time simulations or prove to be ineffective in describing continuous interactions with the constraint. The large deflection possibly encountered by the rod and the nonpenetration condition with the constraint indeed conspire to make this relatively broad class of problems nonlinear in many respects. Buckling phenomena due to lateral and torsional instabilities are also susceptible to occur for the range of loads applied in most medical and industrial applications. Additionally, the problem involves an *a priori* unknown number of contacts between the rod and the constraint which, for some formulations, may be particularly challenging from an algorithmic standpoint. Finally, in a large majority of phenomena that fall within this class of problem, the rod configuration at its extremities is dictated by the environment or application under consideration while the length of the rod is *a priori* unknown. The formulation of such problems leads to the establishment of isoperimetric constraints (Denoël and Detournay, 2011), *i.e.*, integral constraints on the unknown length of the rod.

I.2 Related efforts

The considerable financial interest associated with both industrial and medical fields lead to significant research on constrained elastic rods. However, despite being concerned with sensibly similar challenges and overlapping objectives, research groups have mostly restricted their investigation to one particular phenomenon and remarkably few synchronized efforts have been made. The following paragraphs summarize the main methods conventionally proposed to model these problems as well as the associated limitations.

Oil and gas industry

The interest for a complete torque-and-drag model has been growing since the early eighties, shortly after the commercial viability of deviated wells was recognized by the oil and gas industry. The first contribution is due to Johancsik et al. (1984), who proposed a *soft string model* that ignores the bending stiffness of the drillstring as well as the clearance between the borehole and the drillstring. This simplified model, resulting in a continuous contact along the entire drillstring, was then used by Sheppard et al. (1987), who incorporated the effects of the mud

pressure and addressed the issue of optimal well path design previously introduced by McClendon (1985). Due to the simplicity of the soft string model and its ability to provide reasonably good approximations for the contact forces and loads for relatively smooth well trajectories, this model has been extensively used by the industry and several torque-and-drag analysis of field cases have been performed (Maidla and Wojtanowicz, 1987; Brett et al., 1989; Wilson and Yalcin, 1992; Aadnøy and Andersen, 2001). These studies however emphasize the lumped-parameter nature of the friction coefficient which typically differ between drag and torque analyses as well as between pick-up and slack-off operations (Mitchell and Samuel, 2007). As the borehole (micro and macro) tortuosity increases and the trajectories complicate, the effects of the drillstring bending stiffness become more significant and the soft string model, therefore, loses its accuracy. The first *stiff string model* was proposed by Ho (1988) who concluded that the effects of stiffness are dominant in the collar and heavy weight drillpipe sections. Introducing two distinct friction coefficients depending on the angular and axial velocities, Zifeng et al. (1993) later incorporated into Ho's model the effects of the drillstring motion state as well as the drilling fluid properties. These stiff string models, assuming continuous contact along the wellbore, have been applied advantageously to coiled tubing (McSpadden and Newman, 2002; Yi et al., 2004).

Although the significance of the drillstring bending stiffness in torque-and-drag analysis is commonly acknowledged, the substantial complexity associated with the stiff string model led the industry to favor its soft string counterpart until relatively recently. The ability to accurately account for the effects of hole size, clearance and post-buckling behavior have additionally been identified as central requirements for the next generation of torque-and-drag models (Mason and Chen, 2007; Menand et al., 2009). Conscious of this reflection, various research groups have been using advanced numerical methods with built-in management of the contacts to tackle the interactions between the drillstring and the borehole. Rezmer-Cooper et al. (1999) for instance employed the finite element method to quantify the forces experienced by the drillstring in an attempt to aid planning decisions and reduce costs. Similarly, Newman and Procter (2009) and Wu et al. (2011) combined a finite element analysis of the drillstring with a finite difference scheme to obtain a dynamical model of the drillstring behavior inside the borehole. These finite element analyses generally require, however, dense meshes to properly capture the response of the system in the vicinity of contacts and, therefore, result in computational times inappropriate for real-time simulations. As an alternative approach, Menand et al. (2006) coupled a contact algorithm and a numerical integration scheme in an effort to reduce computational times.

Special care has also been devoted to the helical buckling as well as the post-buckling behaviors of drillstrings inside boreholes (Huang and Pattillo, 2000; van der Heijden, 2001; Cunha, 2004). These studies are however confined to a straight conduit and very little work (Wu and Juvkam-Wold, 1995) has been dedicated to curved wellbores.

Medical industry

The medical industry has developed diverse commercial environments (*e.g.* VIST or ANGIO Mentor) which propose to cardiologists and interventional radiologists a safe framework to acquire ample expertise or specific skills while patient safety is not at risk. In an educational environment, these simulators may facilitate or improve the learning of new procedures as well as increase the surgical experience of trainees before practicing on humans (Dawson, 2006). Such simulators however suffer from a lack of realism in the instrument behavior since little physics-based modeling is generally involved (Weill et al., 2007; Luboz et al., 2010). Aiming at a more realistic modeling of the instruments behavior, various academic research group have simultaneously been investigating the topic using different strategies. Chui et al. (2002) employed, for instance, a finite element method to capture the interaction of the catheters and guidewires with the vascular system. Similarly, Cotin et al. (2000) and Cotin et al. (2005) proposed an incremental finite element approach associated with a substructure decomposition algorithm which results in computational times suitable for real-time simulations. However the approach may be ineffective in describing continuous interactions with the environment. To circumvent this serious drawback and enhance accuracy, Konings et al. (2003) and Alderliesten et al. (2007) resorted to a Cosserat model of the guidewire which, however, results in computational times inappropriate for real-time simulations. As an alternative approach, Luboz et al. (2009) and Luboz et al. (2010) proposed a hybrid mass-spring particle system approach. Modeling the guidewire by means of a planar elastica inside a curved channel, Chen and Li (2007) carried out both experimental and analytical works to investigate lagging phenomenon in the longitudinal motion of the wire that physicians may encounter.

I.3 Methodology

More than focusing on one particular real-world phenomenon, this thesis intends to propose a computational model that may be applied to a class of problems. It may however be beneficial to consider a representative, yet versatile, canonical problem serving as a backbone for its description. In this context, we consider here an elastic rod deforming inside or around a generic constraint defined as a perfectly stiff, frictionless, normal ringed surface (Bastl et al., 2014). The axis or spine curve associated therewith, referred to as *reference curve* independently of the constraint nature, is further presumed to be known and regular (*i.e.*, its tangent vector being everywhere well defined.) The rod, initially straight, is assumed to behave as a one-dimensional elastic body according to the special Cosserat theory of rods. Although readily extensible to encompass effects of shear, the present formulation is, for the sake of brevity, restricted to unshearable rods that can undergo large deformations in space by experiencing bending, torsion and extension. Variants of this general problem may be defined depending on the nature of the boundary conditions at the rod extremities or on whether the length of the rod is known or not. We opt here for one of these variants, which may actually be considered

as foundational to the approach proposed to solve any other constrained elastic rod problem. In this optic, we focus our efforts on a two-point boundary value problem specifying both the position and inclination of the rod at its extremities and which distinguishes by its unknown domain, that is the rod length.

I.3.1 Canonical problem

Specifically, let us define the right-handed orthonormal basis $\{\boldsymbol{e}_j\}$ for the Euclidean space $\mathbb{E}^3$ and denote by $\boldsymbol{R}(S) = X_j\,\boldsymbol{e}_j$ the parameterization of the reference curve $\mathscr{C}$. The parameter S, referred to as the *Eulerian coordinate*, identifies a section along $\mathscr{C}$ which consists of all points whose reference position is on the plane perpendicular to the reference curve at S. Without loss of generality, the parameterization of this curve is assumed to be natural (or arc-length), so that its tangent is a unit vector. The constraint surface, considered frictionless and undeformable, is defined as the normal ringed surface generated by sweeping a circle of radius $Q(S)$ centered on the reference curve and in the normal plane to $\mathscr{C}$.

The rod, materialized by its centerline $\mathscr{E}$, is subjected to a body force $\boldsymbol{f}$ and a body couple $\boldsymbol{m}$. Assuming cylindrical symmetry and homogeneous properties, the rod is characterized by its axial stiffness A, bending stiffness B and torsional stiffness C. Although the length of the rod is unknown, both its position and inclination with respect to the reference curve are prescribed at the extremities of the canonical problem. In terms of standard support conditions, this configuration may be obtained by imposing on extremity of the rod to be clamped while the other may be seen as moving freely through a frictionless sliding sleeve. The rod length is therefore free adjust to its external loading and boundary conditions. This feature is referred to as *self-feeding* in the following. To close this formulation, this extremity is further subjected to the combined action of known axial force and twisting moment.

I.3.2 Segmentation strategy

As already emphasized, the determination of the position of the contacts between the rod and the constraint as well as the extent of these contacts constitutes a central concern of this work. When dealing with the insertion of a thin rod in a tube-like constraint, it is natural to treat this process as an evolutive problem. Starting from a contact-free configuration, the introduction of the rod is simulated by incrementally translating the distal extremity of the rod along the constraint axis while maintaining the position of the other at the inlet of the constraint, the length of the rod being free to adjust to the new configuration. As discrete and/or continuous contacts develop between the rod and the constraint, a commonly adopted strategy consists in partitioning the global problem into a set of boundary value problems (Chen and Li, 2007; Denoël, 2008) specifying both the position and inclination of the rod at its extremities. Accordingly, each elementary problem corresponds to a segment of rod either in continuous contact with the constraint or free of contact between its extremities.

The equilibrium of the global problem is reached by identifying the correct contact pattern, *i.e.*, which satisfies the non-penetration condition as well as the global boundary conditions, and preserving the integrity of the rod. From an algorithmic standpoint, this segmentation strategy may be conceptualized as three nested loops. The outer loop, concerned with the identification of the contact pattern, establishes the number of contacts and their nature. Considering a contact pattern, the median loop ascertains the position and extent of these contacts by ensuring the continuity of the rod between elementary problems. Evidently, these loops require the evaluation of the rod configuration along the global problem and, therefore, necessitate to solve each elementary problem. This procedure, which constitutes the inner loop, may be organized such that the set of elementary problems is solved sequentially, that is by propagating the solution from one extremity to the other.

For non-evolutive problems, which do not involve the displacement of the rod extremities or varying boundary conditions, a similar approach may be adopted. Ignoring the constraint, the algorithm is initialized by evaluating the unconstrained configuration of the rod. The non-penetration condition is then progressively reestablished by segmenting the global problem once (where the penetration is the largest) in each region of contiguous penetration. With this estimate of the number of contacts (assumed to be discrete) and their approximate positions along the constraint, the rod configuration is reevaluated along each elementary problem (inner loop) and the positions of the contacts updated (median loop.) New cycles of calculations, involving the reassessment of the contact pattern (outer loop), follow until convergence is reached on the number, type, and position of contacts.

I.3.3 Elementary problems

This segmentation strategy is constructed around the systematic resolution of a sequence of elementary problems. These building blocks consists in segments of rod, either in continuous contact with the constraint or free of contact, that are forced to go through two fixed points in space while being subjected to a distributed body force and, potentially, a body couple, see Figure I.3.1. The continuous contact and contact-free configurations essentially differ by the nature of the body force acting on the rod. While, in the absence of additional loads, solely subjected to its own weight along a contact-free problem, the rod is additionally compelled to lay on the constraint surface along a continuous contact. Assuming frictionless interactions between the rod and the constraint surface, the resulting contact pressure acts as an additional distributed body force oriented normally to the frictionless constraint surface, its magnitude being however *a priori* unknown.

As for the global problem, the length (in both deformed and undeformed configurations) of the rod spanning each elementary problem and satisfying the associated boundary conditions is unknown and, therefore, constitutes an inherent part of the solution. This feature, specific to (one dimensional) free boundary problems (Friedman, 2000), is encountered in other applications as well, *e.g.* the continuous casting process and the extrusion of plastic through a draw

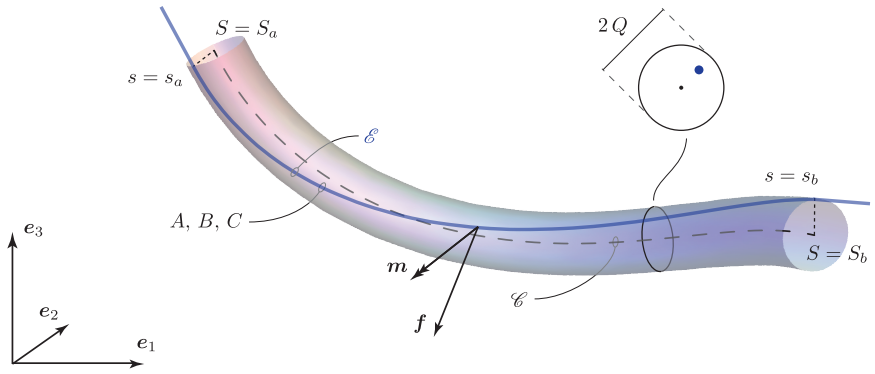

Figure I.3.1: Description of the elementary problem. The rod, materialized by its centerline $\mathscr{E}$, is subjected to the body force $\boldsymbol{f}$ and body couple $\boldsymbol{m}$ between its extremities s_a and s_b. It is characterized by its axial stiffness A, bending stiffness B and torsional stiffness C. The constraint is the swept surface generated by a circle of radius Q centered on the reference curve $\mathscr{C}$ and in its normal plane.

plate (Donea et al., 2004), the laying of subsea cables and pipelines (Guarracino and Mallardo, 1999; Stump and van der Heijden, 1999) or, in slightly different configurations, the elastically deformable arm scale (Bosi et al., 2014) and the self-encapsulation of elastic rods (Bosi et al., 2015). Resorting to a conventional Lagrangian approach, the axially unconstrained nature of these problems, namely the *self-feeding* feature, combined with the boundary conditions specifying the rod location at both extremities lead to the establishment of isoperimetric constraints, namely, integral constraints on the unknown length of the rod. Additionally, the assessment of the unilateral contact condition requires, in principle, the comparison of two curves parametrized by distinct curvilinear coordinates (*i.e.*, the rod and the constraint axis), an intensive computational task contributing to the numerical burden associated with conventional approaches.

To optimize the resolution of the rod configuration along these elementary problems, a significant part of this thesis focuses on the adaptation of the equations governing the rod deflection to this particular class of problems. For planar elastica, the above-mentioned difficulties have been circumvented by adopting an Eulerian description of the rod in terms of the curvilinear coordinate associated with the constraint (Denoël and Detournay, 2009b; Chen and Ro, 2010) and by describing its deformed configuration by means of the signed distance between the rod and the axis of the constraint (Denoël and Detournay, 2011). This approach has been shown to drastically simplify the resolution of the constrained problem by trivializing the assessment of the unilateral contact condition and limiting the degeneracy of the governing equations with diminishing clearance or bending stiffness. Generalizing these concepts, the Eulerian formulation is extended to three-dimensional configurations by reformulating the special Cosserat rod theory within the framework of a generic constraint defined as a perfectly stiff canal normal

ringed surface. This approach not only trivializes the detection of new contacts but also suppresses the isoperimetric constraints resulting from the self-feeding feature of these elementary problems and the imposition of the rod position at the extremities of each rod segment.

I.4 Personal contributions

This work is driven by the wealth of biological, medical and engineering applications concerned by the constrained deformation of elastic rods and the need to efficiently solve this class of problems. Building on the work by Denoël and Detournay (2011), the concept of *segmentation strategy* is generalized and the *Eulerian formulation* extended to three-dimensional configurations. With the ambition to shed new lights on real world-phenomena, the methodical approach presented in this dissertation emphasizes the profound connection between mechanics and differential geometry associated with this class of problems. The most notable contributions of this thesis are:

- The **Eulerian formulation** of the rod governing equations (Huynen et al., 2014; submitted). Valid for both the continuous contact and contact-free configurations, this approach hinges on describing the rod deformed configuration by means of its relative position with respect to a reference curve and on restating the rod local equilibrium in terms of the curvilinear coordinate parameterizing this curve, rather than the rod.
- The particularization of the rod governing equations to **surface bound configurations** (Huynen et al., 2015). The continuous contact of an elastic rod with a smooth surface is studied from a geometrical perspective and the rod flexural as well as torsional strains are re-expressed in terms of intrinsic and extrinsic properties of the constraining surface along its centerline. This formulation emphasizes the influence of the constraint geometry on the rod deformed configuration and the reaction pressure.
- The adaptation of the latter formulation to rods in **continuous contact with a normal ringed surface** and the formulation of a specific Eulerian description of the rod configuration in terms of its angular position along the constraint surface.
- The implementation of a **collocation method** for the systematic solution of the elementary problems.
- The development of a **complete algorithm** for the resolution of the canonical problem under consideration.

I.5 Outline

The computational model proposed in this thesis rests on the systematic resolution of rod segments, either in continuous contact with the constraint or contact-free between its extremities.

A significant part of this work is therefore devoted to the study and analysis of these elementary problems. **Chapter II** starts with a succinct introduction to the theory of elastic rods and a description of the shortcomings associated with the conventional Lagrangian formulation of the elementary problem. An Eulerian formulation of the rod governing equations is then proposed in Section II.2. The validity of this formulation, which may be applied to both the continuous contact and contact-free configurations, is finally assessed by comparison with known analytical results and numerical solutions.

This structure is carried to **Chapter III**. Particularizing the rod governing equations to surface bound configurations, a Lagrangian formulation for rods in continuous contact with a smooth constraining surface of arbitrary geometry is obtained. These equations are then adapted to normal ringed surfaces and an Eulerian formulation is again derived in Section III.2. Both formulations are validated on constraining surfaces of simple geometry, yet resulting in surprisingly complex equilibrium configurations.

The segmentation strategy adopted to solve the canonical problem is described in **Chapter IV**. Before illustrating this procedure, the numerical method implemented to solve the sequence of elementary problems (within the Eulerian framework) as well as details about the complete algorithm, *viz.* the identification and validation of the contact pattern, are presented.

Chapter V closes this thesis. It summarizes the main results, discusses conclusions, limitations and directions for future research.

"The best model is the simplest model that still serves its purpose, [...]"
Velten (2009)

Chapter II

Eulerian Formulation of Elastic Rods Deforming in Space

Before exposing the details and the scope of the proposed formulation, a brief introduction to the theory of rods is presented and the shortcomings of the conventional Lagrangian formulation are emphasized.

This theory, central to the problem under consideration, provides approximate solutions of the three-dimensional equations of elasticity which are satisfactory for slender bodies, *i.e.*, bodies that are characterized by two dimensions sufficiently small compared to the third one. The foundations of such theory of *one-dimensional bodies* were laid by J. Bernoulli (1694) who provided the moment balance for the planar deformation of an (inextensible and unshearable) elastica. Assuming each fiber of the cross section to obey Hooke's law, Euler derived the classic linear constitutive equation relating bending moment to curvature and, later, published in the addendum *De curvis elasticis* of his landmark book on variational techniques all the possible planar equilibrium configurations of a uniform, initially straight elastica under terminal loads (1744).

Lacking the concept of strain and especially the notion of twist density later introduced by Saint-Venant (1843), Euler could not extend his theory from planar to spatial deformations. Kirchhoff (1859), Clebsch (1862) and Love (1927) successively refined the notion of strain and thereby founded a remarkable framework for the deformation of elastic filaments in space. This approach also led to Kirchhoff's kinetic analogy which connects the static deformations of unshearable and inextensible, weightless, rods to the dynamics of spinning tops; see Nizette and Goriely (1999) for a complete classification of the shapes adopted by the elastic filament. A generalization of Kirchhoff's theory was later proposed by Cosserat and Cosserat (1909), who abandoned the assumptions of unshearable and inextensible nature of the filaments. In the following sections, the equations governing the static deformation of rods are derived using this

special Cosserat theory, see Antman (2005) or Audoly and Pomeau (2010) for more details.

II.1 Lagrangian formulation

Consider a long, slender, elastic body that can undergo large deformations in space by experiencing bending, twisting and extension but no shear deformation. The special Cosserat theory formulates a versatile model of a *rod* to describe the deformation of such a three-dimensional object. Ignoring its transverse dimensions compared to its length, the slender elastic solid is reduced to a one-dimensional body endowed with mechanical properties that are suitably averaged over its cross section. Hence, at large scale, a thin rod is described by the path of its centerline in the Euclidean space and, to keep track of the twist, a material frame that follows the elastic body upon deformation. Together, the centerline and the material frame, form what is commonly called a *Cosserat rod*, a *Cosserat curve* or simply a rod.

Let us define the right-handed orthonormal basis $\{\boldsymbol{e}_j\}$ for the Euclidean space $\mathbb{E}^3$ and consider a straight reference configuration with cylindrical symmetry and homogeneous properties as shown in Figure (II.1.1). The rod deformed configuration is entirely defined by the three vector-valued functions

$$[s_a, s_b] \ni s \mapsto \boldsymbol{r}(s), \boldsymbol{d}_1(s), \boldsymbol{d}_2(s) \in \mathbb{E}^3, \tag{II.1.1}$$

where the parameter s, which is referred to as the *Lagrangian coordinate* in contrast to the Eulerian coordinate S, identifies a material cross section in the arc-length parameterization $\boldsymbol{r}^0(s)$ of the rod centerline in its reference configuration. The vector $\boldsymbol{r}(s) = x_j\, \boldsymbol{e}_j$ parameterizes the space curve $\mathscr{E}$ that represents the rod centerline in its deformed configuration; the pair of orthogonal unit vectors $\boldsymbol{d}_1(s), \boldsymbol{d}_2(s)$ characterizes the configuration of two material lines of the cross section. Similarly, the rod in its reference configuration is identified by the (straight) curve $\mathscr{E}^0$ materializing its centerline together with a pair of unit vectors, that is the three vector-valued functions $\boldsymbol{r}^0(s), \boldsymbol{d}_1^0(s), \boldsymbol{d}_2^0(s) \in \mathbb{E}^3$. We will henceforth assume that the parameterization of the rod centerline is at least C^4–continuous.

II.1.1 Kinematics

Setting $\boldsymbol{d}_3(s) = \boldsymbol{d}_1 \times \boldsymbol{d}_2$, the triplet of *directors* $\{\boldsymbol{d}_j(s)\}$ constitutes, for each cross section s, a material frame in which the deformed state of the elastic rod is naturally described. The twist vector $\boldsymbol{u}(s) = u_j\, \boldsymbol{d}_j$, which relates the rotation of the directors to the strains, and stretch vector $\boldsymbol{v}(s) = v_j\, \boldsymbol{d}_j$ are defined through the following kinematic relations

$$\frac{\mathrm{d}\boldsymbol{d}_j}{\mathrm{d}s} = \boldsymbol{u} \times \boldsymbol{d}_j, \tag{II.1.2}$$

$$\frac{\mathrm{d}\boldsymbol{r}}{\mathrm{d}s} = \boldsymbol{v}. \tag{II.1.3}$$

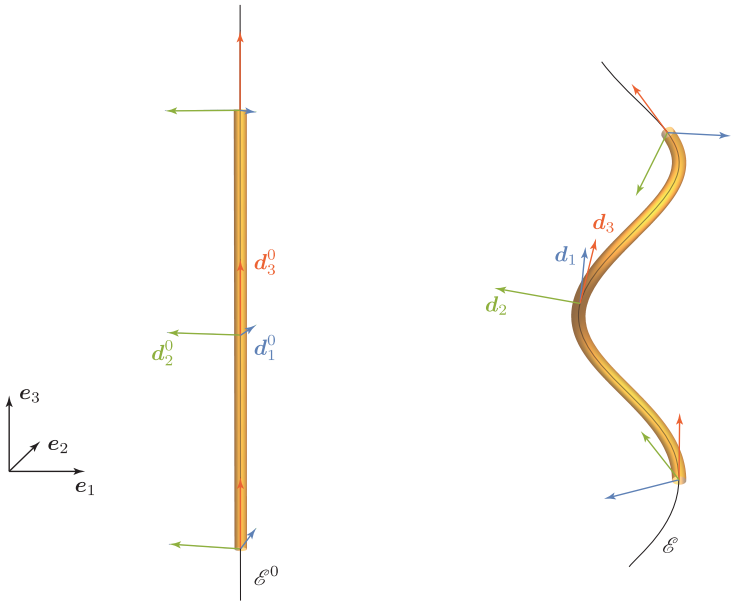

Figure II.1.1: Initial and deformed configurations of a Cosserat rod. In the deformed configuration, the rod is defined by its centerline $\mathscr{C}$ and the director basis $\{\boldsymbol{d}_j\}$ describing the orientation of the material cross section.

Their components, entering into the constitutive equations, are generally referred to as the strain variables: u_1 and u_2 characterize the local material curvatures, u_3 is a kinematic measure of the twist density, v_1 and v_2 are associated with transverse shearing, and v_3 corresponds to stretching or compression. Mathematically, unshearability is expressed as $v_1 = v_2 = 0$ stating that the stretch vector is everywhere aligned with the normal to the rod cross section and, therefore, reduces to $\boldsymbol{v} = \alpha\, \boldsymbol{d}_3$. The stretch $\alpha(s) > 0$, measuring the rod elongation/shortening, may be interpreted as the Jacobian of the mapping $s \mapsto \bar{s}(s)$ between the Lagrangian coordinate s identifying a rod cross section in its unstressed configuration and the stretched coordinate $\bar{s}$ parameterizing the rod in its deformed configuration. The stretch, the material curvatures and the twist density account for change of shape and are referred to as the strain variables. The associated local modes of deformation – stretching, bending and twisting – are illustrated in Figure II.1.2. It can be shown that the strains are invariant under rigid body motions, and that $\boldsymbol{u}(s)$ and $\boldsymbol{v}(s)$ determine a configuration to within a rigid motion (Antman, 2005).

Under the unshearability assumption, the normal to the rod cross section is everywhere aligned with the tangent vector to the rod centerline. The directors therefore form what is called an adapted frame, that is a frame with members either tangent to or perpendicular to $\mathscr{C}$ (Bishop, 1975). It is, however, not to be confounded with the Frenet-Serret trihedron $\{\boldsymbol{t}, \boldsymbol{n}, \boldsymbol{b}\}$

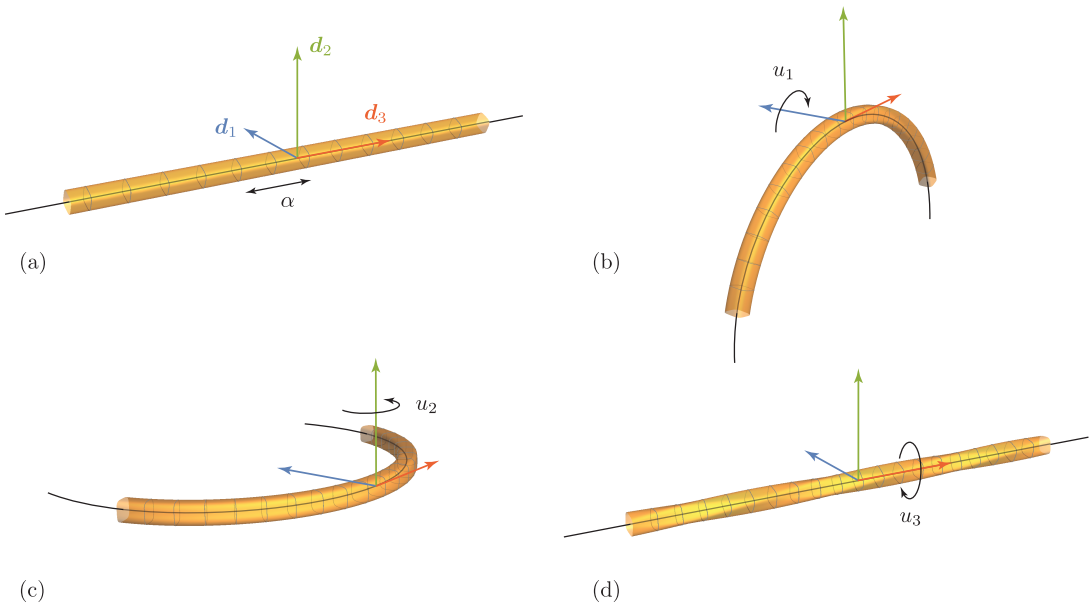

Figure II.1.2: Local modes of deformation of an unshearable elastic rod. (a) Stretching identified by the stretch α. (b,c) Bending associated with the material curvatures u_1 and u_2 that measure the rotation of the material frame about the directors $\boldsymbol{d}_1$ and $\boldsymbol{d}_2$, respectively. (d) Twisting characterized by the twist density u_3 that measures the rotation of the material frame about the unit tangent $\boldsymbol{d}_3$.

defined to be the unit tangent, normal and binormal vectors to $\mathscr{E}$

$$\boldsymbol{t}(s) = \frac{\mathrm{d}\boldsymbol{r}}{\mathrm{d}s} \Big/ \left\| \frac{\mathrm{d}\boldsymbol{r}}{\mathrm{d}s} \right\|, \qquad \boldsymbol{n}(s) = \frac{\mathrm{d}\boldsymbol{t}}{\mathrm{d}s} \Big/ \left\| \frac{\mathrm{d}\boldsymbol{t}}{\mathrm{d}s} \right\|, \qquad \boldsymbol{b}(s) = \boldsymbol{t} \times \boldsymbol{n}, \tag{II.1.4}$$

and which ceases to be valid at singular points, *i.e.*, points where $\boldsymbol{r}''(s) = 0$. This right-handed orthonormal basis satisfies the Frenet-Serret formulae

$$\frac{\mathrm{d}\boldsymbol{t}}{\mathrm{d}s} = \alpha\,\kappa\,\boldsymbol{n}, \qquad \frac{\mathrm{d}\boldsymbol{n}}{\mathrm{d}s} = -\alpha\,\kappa\,\boldsymbol{t} + \alpha\,\tau\,\boldsymbol{b}, \qquad \frac{\mathrm{d}\boldsymbol{b}}{\mathrm{d}s} = -\alpha\,\tau\,\boldsymbol{n}, \tag{II.1.5}$$

with the curvature κ and torsion τ defined as

$$\kappa(s) = \left\| \frac{\mathrm{d}\boldsymbol{r}}{\mathrm{d}s} \times \frac{\mathrm{d}^2\boldsymbol{r}}{\mathrm{d}s^2} \right\| \Big/ \left\| \frac{\mathrm{d}\boldsymbol{r}}{\mathrm{d}s} \right\|^3, \qquad \tau(s) = \left(\frac{\mathrm{d}\boldsymbol{r}}{\mathrm{d}s} \times \frac{\mathrm{d}^2\boldsymbol{r}}{\mathrm{d}s^2} \right) \cdot \frac{\mathrm{d}^3\boldsymbol{r}}{\mathrm{d}s^3} \Big/ \left\| \frac{\mathrm{d}\boldsymbol{r}}{\mathrm{d}s} \times \frac{\mathrm{d}^2\boldsymbol{r}}{\mathrm{d}s^2} \right\|^2, \tag{II.1.6}$$

respectively. The curvature κ measures the departure of the curve from the original straight line, while the torsion τ quantifies the degree to which it twists out of a plane (rate of change of the curve's osculating plane) and must therefore be distinguished from the twist density u_3 which can be interpreted as a measure of the angle of rotation between two adjacent sections of the rod (Love, 1927). Provided the rod centerline does not have inflection points, the Frenet-Serret trihedron and the directors basis are related through a rotation about $\boldsymbol{t} = \boldsymbol{d}_3$ that defines the internal twist angle ϕ (also referred to as the *register angle*)

$$\boldsymbol{d}_1(s) = \cos\phi\,\boldsymbol{n} + \sin\phi\,\boldsymbol{b}, \tag{II.1.7}$$

$$\boldsymbol{d}_2(s) = -\sin\phi\,\boldsymbol{n} + \cos\phi\,\boldsymbol{b}. \tag{II.1.8}$$

The twist vector may therefore be rewritten in terms of the curvature κ and torsion τ (Moulton et al., 2012) describing the local geometry of the space curve $\mathscr{E}$

$$\boldsymbol{u}(s) = \alpha\,\kappa\,\sin\phi\,\boldsymbol{d}_1 + \alpha\,\kappa\,\cos\phi\,\boldsymbol{d}_2 + \left(\alpha\,\tau + \frac{\mathrm{d}\phi}{\mathrm{d}s} \right) \boldsymbol{d}_3, \tag{II.1.9}$$

where $\mathrm{d}\phi/\mathrm{d}s$ is the rate of rotation of the directors $\{\boldsymbol{d}_1, \boldsymbol{d}_2\}$ with respect to the normal and binormal, the internal twist angle being given by $\tan\phi = u_1/u_2$.

II.1.2 Mechanical equilibrium

Considering only local interactions between adjacent cross sections of the rod, the internal force $\boldsymbol{F}(s) = F_j\,\boldsymbol{d}_j$ and moment $\boldsymbol{M}(s) = M_j\,\boldsymbol{d}_j$ are defined as the resultant of the contact forces and the resultant couple of these forces, respectively, acting on the cross section s. A small rod element of length $\mathrm{d}s$ is therefore submitted to the contact forces $\boldsymbol{F}(s + \mathrm{d}s)$ and $-\boldsymbol{F}(s)$ from the neighboring material as well as the resultant contact torques $\boldsymbol{M}(s + \mathrm{d}s) + \boldsymbol{r}(s + \mathrm{d}s) \times \boldsymbol{F}(s + \mathrm{d}s)$ and $-\boldsymbol{M}(s) - \boldsymbol{r}(s) \times \boldsymbol{F}(s)$, see Figure II.1.3. Acting on this element are also the resultant of all

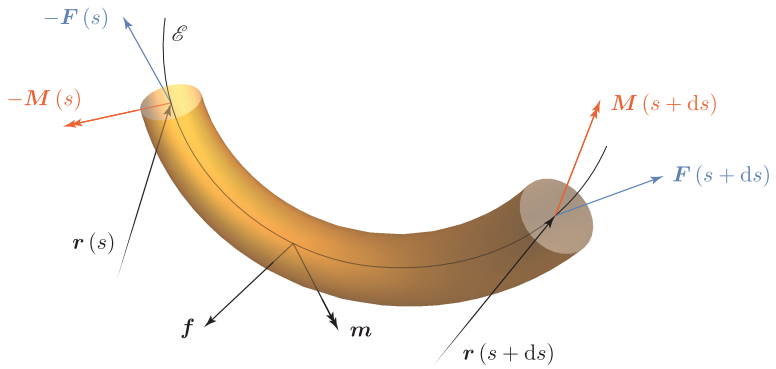

Figure II.1.3: Forces (arrows) and moments (double arrows) acting on a small rod element of length $\mathrm{d}s$. The body force $\boldsymbol{f}(s)$ and body couple $\boldsymbol{m}(s)$ per unit reference length are balanced by the internal forces $\boldsymbol{F}(s)$ and moment $\boldsymbol{M}(s)$ transmitted by the neighboring material.

other forces $\boldsymbol{f}\,\mathrm{d}s$ and the resultant of all other torques $(\boldsymbol{m}+\boldsymbol{r}\times\boldsymbol{f})\,\mathrm{d}s$ where $\boldsymbol{f}$ and $\boldsymbol{m}$ are the body force and body couple per unit reference length at $s+\mathrm{d}s/2$, respectively. At equilibrium, one must therefore have

$$\boldsymbol{F}(s+\mathrm{d}s)-\boldsymbol{F}(s)+\boldsymbol{f}\,\mathrm{d}s=0, \quad \text{(II.1.10)}$$

$$\boldsymbol{M}(s+\mathrm{d}s)-\boldsymbol{M}(s)+\boldsymbol{r}(s+\mathrm{d}s)\times\boldsymbol{F}(s+\mathrm{d}s)-\boldsymbol{r}(s)\times\boldsymbol{F}(s)+(\boldsymbol{m}+\boldsymbol{r}\times\boldsymbol{f})\,\mathrm{d}s=0 \quad \text{(II.1.11)}$$

such that, taking the limit for $\mathrm{d}s\to 0$, the balance of linear and angular momenta read (Dill, 1992; Antman, 2005)

$$\frac{\mathrm{d}\boldsymbol{F}}{\mathrm{d}s}+\boldsymbol{f}=\boldsymbol{0}, \quad \text{(II.1.12)}$$

$$\frac{\mathrm{d}\boldsymbol{M}}{\mathrm{d}s}+\boldsymbol{v}\times\boldsymbol{F}+\boldsymbol{m}=\boldsymbol{0}, \quad \text{(II.1.13)}$$

with $\boldsymbol{f}(s)$ and $\boldsymbol{m}(s)$ the body force and body couple per unit reference length at s, respectively. The potential reaction pressure $\boldsymbol{p}(s)$ acting along continuous contacts is treated as a body force.

II.1.3 Constitutive relations

The system formed by equations (II.1.2–II.1.3) and (II.1.12–II.1.13) is closed by expressing that the internal force $\boldsymbol{F}(s)$ and moment $\boldsymbol{M}(s)$, defined as the resultant of the contact forces and the resultant couple of these forces, are related to the strain variables $u_j(s), v_j(s)$. Such constitutive relations may be obtained under suitable assumptions (commonly referred to as the Kirchhoff-Love hypotheses although none of them made such hypotheses) on the rod mechanical and kinematical behavior: *(i)* every cross section deforms in a rigid-body manner, *(ii)* the transverse stress is zero, and *(iii)* the bending and twisting moments are proportional to the local material

curvature and twist density, respectively. The resulting relations read

$$\boldsymbol{F} = F_1\,\boldsymbol{d}_1 + F_2\,\boldsymbol{d}_2 + A\,(\alpha - 1)\,\boldsymbol{d}_3, \tag{II.1.14}$$

$$\boldsymbol{M} = B\,(u_1\,\boldsymbol{d}_1 + u_2\,\boldsymbol{d}_2) + C\,u_3\,\boldsymbol{d}_3, \tag{II.1.15}$$

with the axial stiffness A, the bending stiffness B and the torsional stiffness C.

Alternatively, following the classical theory of finite displacements of thin rods developed by Kirchhoff (1859, 1876), Clebsch (1862) and reformulated by Love (1927), a satisfactory approximation of the three-dimensional equations of nonlinear elasticity may be derived. The original objective of Kirchhoff and Clebsch was to achieve a reduction of the three dimensional body to a one dimensional rod by expressing that two dimensions are very small compared to the third. Considering only small strains with respect to the reference configuration but accounting for large rotations, they derived an asymptotic decomposition of the rod motion without making any assumptions about the global constitutive relations. Restricting ourselves to rods of circular cross section, the Appendix A.1 is a summary of the general ideas of Kirchhoff-Clebsch-Love as presented by Dill (1992) in the framework of modern continuum mechanics.

II.1.4 Shortcomings of the Lagrangian formulation

Classic boundary value problems for $\{\boldsymbol{r}\,(s)\,,\boldsymbol{d}_1\,(s)\,,\boldsymbol{d}_2\,(s)\}$ consist of the kinematic equations (II.1.2–II.1.3), the equilibrium equations (II.1.12) and (II.1.13), the constitutive relations (II.1.14–II.1.15) and a combination of kinematic and mechanical boundary conditions (Antman, 2005, pp. 322–328). Considering the orthonormality of the directors, the resulting system consists of fifteen first order differential equations which requires a set of fifteen boundary conditions. See Antman and Kenney (1981, pp. 297–300) for an exhaustive description of the various families and possible combinations of boundary conditions associated with elastic rods. The regular boundary value problems associated with a fixed length $\ell = s_b - s_a$ have been investigated from various perspectives and closed form solutions have been obtained under particular sets of boundary conditions and loadings (Shi and Hearst, 1994; Tan and Witz, 1995; Kehrbaum and Maddocks, 1997). These configurations can however be regarded as exceptional and one must generally resort to numerical techniques (van der Heijden et al., 2003; Goyal et al., 2005; Bergou et al., 2008) to solve the general problem.

In the context under consideration, cf. Section I.3.3, one extremity of the rod is clamped while the other may be seen as moving freely through a frictionless sliding sleeve under the combined action of known axial force and twisting moment. One may assume, without loss of generality, the extremity s_a to be clamped such that the triplet

$$\{\boldsymbol{r}\,(s_a)\,,\boldsymbol{d}_1\,(s_a)\,,\boldsymbol{d}_2\,(s_a)\}\,, \tag{II.1.16}$$

is prescribed at this point. At the end s_b of the boundary value problem, the position of the rod

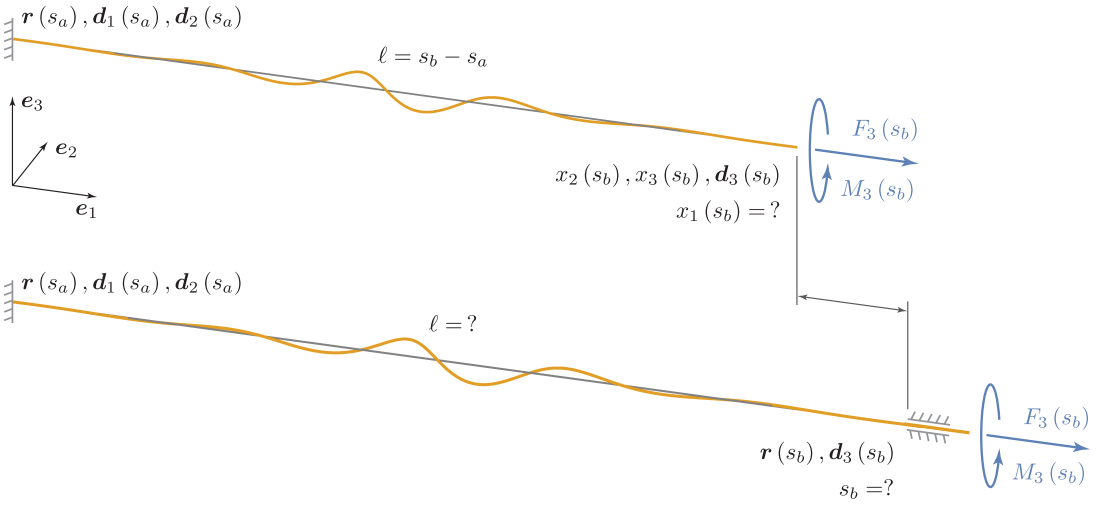

Figure II.1.4: Boundary conditions of the elementary problem. The clamped-sliding sleeve boundary conditions, responsible for self-feeding, are compared to conventional boundary conditions associated with rods of known length.

and the unit tangent are imposed together with the axial force and twisting moment, that is

$$\{\boldsymbol{r}(s_b), \boldsymbol{d}_3(s_b), F_3(s_b), M_3(s_b)\}, \tag{II.1.17}$$

The unstressed length $\ell = s_b - s_a$ being *a priori* unknown, the resulting free boundary value problem is well-posed. This set of boundary conditions is exemplified in Figure II.1.4 where it is compared to its conventional counterpart associated with a rod of fixed length.

The boundary conditions specifying the locations $\boldsymbol{r}(s_a)$ and $\boldsymbol{r}(s_b)$ of the rod centerline at both extremities of the domain however lead to the establishment of isoperimetric constraints. Indeed, although the rod spatial configuration has been specified through the position vector of the rod centerline and the director $\boldsymbol{d}_1(s)$, the parameterization $\boldsymbol{r}(s)$ of the space curve $\mathscr{E}$ does not explicitly appear in the governing equations. The coordinates $x_j(s)$ of the rod centerline in the absolute reference frame $\{\boldsymbol{e}_j\}$ therefore require the integration of the kinematic relation (II.1.3), that is

$$x_j(s) = x_j(s_a) + \int_{s_a}^{s} \boldsymbol{v} \cdot \boldsymbol{e}_j \, \mathrm{d}s. \tag{II.1.18}$$

The boundary conditions and the associated set of integral constraints, on the *a priori* unknown domain $[s_a, s_b]$, result in ill-conditioned equations contributing to the numerical burden associated with the conventional Lagrangian formulation (Denoël and Detournay, 2009b).

As noted in Chapter I, the assessment of the unilateral contact condition constitutes an additional source of difficulties. To ensure that the rod remains either in continuous contact or

free of contact along the whole domain of the problem under consideration, this supplementary constraint necessitates the evaluation of the distance between the rod centerline $\mathscr{E}$ and the reference curve $\mathscr{C}$. However, these two curves being naturally parameterized by the Lagrangian and Eulerian curvilinear coordinates, s and S respectively, the evaluation of this distance reveals to be computationally intensive as it requires the identification of the mapping $s \mapsto S(s)$, from Lagrangian to Eulerian coordinates.

Finally, the ill-conditioning of the governing equations for small bending stiffness, the existence of spurious solutions associated with curling of the rod as well as the demand for increasing accuracy of the solutions with decreasing clearance, are sources of various additional complications or other bottlenecks. Consequently, the Lagrangian formulation of the problem is particularly ineffective and laborious to solve in most circumstances (Denoël and Detournay, 2011).

II.2 Eulerian formulation

The proposed reformulation hinges on describing the rod deformed configuration by means of its relative position about the reference curve $\mathscr{C}$ and restating the rod local equilibrium in terms of the Eulerian curvilinear coordinate associated with the arc-length parameterization $\boldsymbol{R}(S)$ of $\mathscr{C}$ rather than the natural Lagrangian coordinate of the rod.

By analogy with the director basis, one may arbitrarily define a triplet $\{\boldsymbol{D}_j(S)\}$ constituting a right-handed orthonormal basis for each cross section S along the reference curve and such that $\boldsymbol{D}_3 = \mathrm{d}\boldsymbol{R}/\mathrm{d}S$ is the unit vector tangent to $\mathscr{C}$. The kinematics of this adapted frame along the reference curve can, therefore, be described by means of a vector $\boldsymbol{U}(S) = U_j\,\boldsymbol{D}_j$ (Cartan, 1937) as

$$\frac{\mathrm{d}\boldsymbol{D}_j}{\mathrm{d}S} = \boldsymbol{U} \times \boldsymbol{D}_j. \tag{II.2.1}$$

Although theoretically appealing, the identification of this frame with the Frenet-Serret apparatus attached to $\mathscr{C}$ may lead to existence and continuity issues for reference curves with vanishing curvature. While it is not a requisite for the present formulation, defining the $\{\boldsymbol{D}_j\}$–basis such that it constitutes a Bishop frame (Bishop, 1975) is advocated as it results in substantially simpler expressions. Also referred to as the *parallel transport frame*, this adapted frame constitutes an alternative approach to defining a moving frame that is everywhere well defined. Its construction is based on the concept of relatively parallel fields and the observation that, while the tangent vector $\boldsymbol{D}_3$ is unique for any given curve, the pair of orthonormal vectors $\{\boldsymbol{D}_1, \boldsymbol{D}_2\}$ may be chosen arbitrarily provided it remains perpendicular to the tangent vector. In particular, the pair $\{\boldsymbol{D}_1, \boldsymbol{D}_2\}$ may be defined such that the $\{\boldsymbol{D}_j\}$–basis smoothly varies along $\mathscr{C}$ and has zero twist uniformly, *i.e.*, $U_3(S) = 0$, by requiring $\mathrm{d}\boldsymbol{D}_1/\mathrm{d}s \cdot \boldsymbol{D}_2 = 0$ and $\mathrm{d}\boldsymbol{D}_2/\mathrm{d}s \cdot \boldsymbol{D}_1 = 0$.

As presented in Figure II.2.1(a), the parameterization $\boldsymbol{r}(s) = x_j\,\boldsymbol{e}_j$ of the rod centerline can,

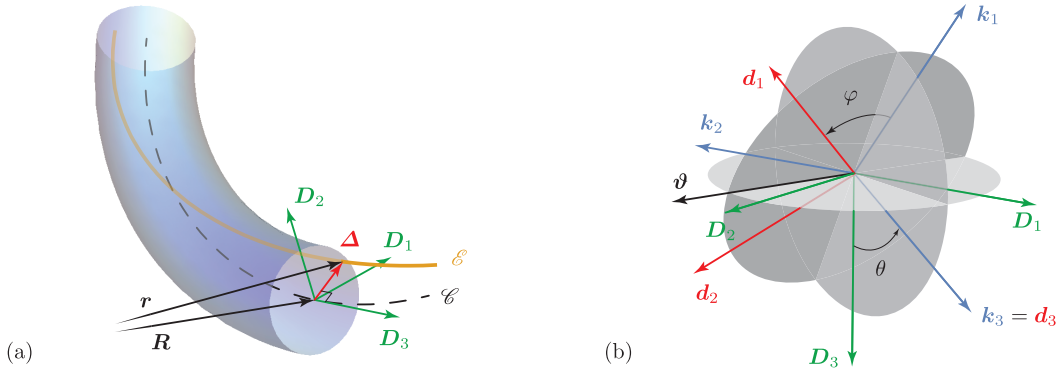

Figure II.2.1: Definition of the eccentricity vector and description of the intermediate $\{\boldsymbol{k}_j\}$–basis. (a) The parameterization of of the rod centerline may be rewritten as $\boldsymbol{r}(s(S)) = \boldsymbol{R}(S) + \boldsymbol{\Delta}(S)$ where the eccentricity, measuring the rod relative position with respect to the reference curve $\mathscr{C}$, vector is such that $\boldsymbol{\Delta} \cdot \boldsymbol{D}_3 = 0$. (b) The intermediate $\{\boldsymbol{k}_j\}$–basis is defined as the image of the $\{\boldsymbol{D}_j\}$-basis through the rotation about the axis $\boldsymbol{\vartheta} = \boldsymbol{D}_3 \times \boldsymbol{d}_3$ and mapping $\boldsymbol{D}_3$ on $\boldsymbol{d}_3$. The rotation of the rod cross section about $\boldsymbol{d}_3 = \boldsymbol{k}_3$ is then described by means of the angle φ.

naturally, be decomposed into

$$\boldsymbol{r}(s(S)) = \boldsymbol{R}(S) + \boldsymbol{\Delta}(S), \tag{II.2.2}$$

where the *eccentricity vector* $\boldsymbol{\Delta}(S) = \Delta_1 \boldsymbol{D}_1 + \Delta_2 \boldsymbol{D}_2$ is a measure of the rod relative position in the cross section of abscissa S. Besides describing the space curve $\mathscr{E}$ with respect to the reference curve $\mathscr{C}$, this decomposition of the position vector $\boldsymbol{r}(s)$ connects the Eulerian and Lagrangian formulations through the mapping $S \mapsto s(S)$.

In the remaining of this Chapter, derivatives of scalar and vector valued functions with respect to the Eulerian coordinate S will be denoted by the apposition of a prime while derivatives with respect to the Lagrangian coordinate s and the stretched coordinates $\bar{s}$ are explicitly specified.

II.2.1 Mappings and Jacobians

Substituting the Lagrangian curvilinear coordinate s by the mapping $S \mapsto s(S)$, the reformulation of the local equilibrium (II.1.12–II.1.13) within the Eulerian framework requires to express the natural derivatives $\mathrm{d}\cdot/\mathrm{d}s$ in terms of Eulerian derivatives $\mathrm{d}\cdot/\mathrm{d}S$. While the Jacobian of the mapping $s \mapsto \bar{s}(s)$ from Lagrangian to stretched coordinates has already been identified as the stretch of the rod $\alpha = \mathrm{d}\bar{s}/\mathrm{d}s$, the Jacobian of the mapping $S \mapsto s(S)$, from Eulerian to Lagrangian coordinates, is obtained by inserting the decomposition (II.2.2) of the rod centerline

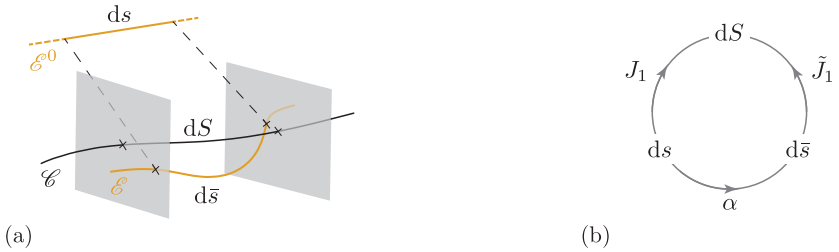

(a) (b)

Figure II.2.2: Mappings and Jacobians. (a) An elementary segment of the reference curve ($\mathrm{d}S$) compared to the corresponding elementary segment of rod in its undeformed ($\mathrm{d}s$) and stretched configurations ($\mathrm{d}\bar{s}$). (b) Correspondence between these three elementary segments and relations between the Jacobians of the respective mappings.

in the definition (II.1.3) of the stretch vector and applying the chain rule differentiation

$$s'(S) = \pm \left\| \boldsymbol{D}_3 + \boldsymbol{\Delta}' \right\| / \left\| \boldsymbol{v} \right\|. \tag{II.2.3}$$

As $\boldsymbol{D}_3$ is a unit vector, this expression emphasizes that the origin of the drift existing between the two curvilinear coordinates is two-fold: *(i)* the eccentricity $\boldsymbol{\Delta}$ between the rod and the reference curve, and *(ii)* the stretch $\|\boldsymbol{v}\| = \alpha$ of the rod itself. This result is emphasized in Figure II.2.2(a), which compares an elementary segment of rod, in its undeformed and stretched configurations, with an elementary segment of the reference curve. Although limiting the range of potential configurations adopted by the rod, selecting the positive sign in this expression and, therefore, imposing the mapping $s(S)$ to be increasing prevents the appearance of parasitic solutions associated with curling, writhing or other configurations involving self-contact and which are unlikely to occur in most applications under consideration.

Similarly, the derivatives of the inverse mapping $s \mapsto S(s)$, from Lagrangian to Eulerian coordinates, as well as the derivatives of the mapping $\bar{s} \mapsto S(\bar{s})$, from stretched to Eulerian coordinates, can be explicitly written in terms of the Eulerian functions $\alpha(S)$, $\Delta_i(S)$ and $U_j(S)$ (with $i = 1, 2$ and $j = 1, 2, 3$.) Defining the Eulerian functions $J_k(S)$ and $\bar{J}_k(S)$ as

$$J_k(S) = \left. \frac{\mathrm{d}^k S}{\mathrm{d}s^k} \right|_{s=s(S)}, \qquad \bar{J}_k(S) = \left. \frac{\mathrm{d}^k S}{\mathrm{d}\bar{s}^k} \right|_{\bar{s}=\bar{s}(S)}, \tag{II.2.4}$$

with $J_1(S) = 1/s'(S)$ and $\bar{J}_1 = 1/\bar{s}'(S)$, the recursive relations

$$J_k(S) = J'_{k-1} J_1, \qquad \bar{J}_k(S) = \bar{J}'_{k-1} \bar{J}_1, \tag{II.2.5}$$

are obtained for $k > 1$. Finally, note that the Jacobians of these mappings are related through the circular relation $J_1 = \alpha \bar{J}_1$, see Figure II.2.2(b), and that $\boldsymbol{r}' \cdot \boldsymbol{r}' = \bar{J}_1^{-2}$ and $\boldsymbol{r}' \cdot \boldsymbol{r}'' = -\bar{J}_2 / \bar{J}_1^4$.

II.2.2 Directors and strain variables

Through the introduction of the eccentricity vector, the space curve $\mathscr{E}$ characterizing the rod centerline in its deformed configuration is expressed by reference to the space curve $\mathscr{C}$. Differentiating (II.2.2) with respect to the Eulerian coordinate, the rod local inclination reads

$$\boldsymbol{d}_3 = \bar{J}_1 \left(\boldsymbol{D}_3 + \boldsymbol{\Delta}' \right), \tag{II.2.6}$$

which emphasizes its representation in terms of the tangent vector to the reference curve. Projecting this relation in the $\{\boldsymbol{D}_j\}$–basis and accounting for the definition (II.2.1) of the vector $\boldsymbol{U}(S)$, the components of $\boldsymbol{d}_3$ in the frame attached to the reference curve are

$$g_1(S) = \boldsymbol{d}_3 \cdot \boldsymbol{D}_1 = \bar{J}_1 \left(\Delta_1' - \Delta_2 U_3 \right), \tag{II.2.7}$$

$$g_2(S) = \boldsymbol{d}_3 \cdot \boldsymbol{D}_2 = \bar{J}_1 \left(\Delta_2' + \Delta_1 U_3 \right), \tag{II.2.8}$$

$$g_3(S) = \boldsymbol{d}_3 \cdot \boldsymbol{D}_3 = \bar{J}_1 \left(1 - \Delta_1 U_2 + \Delta_2 U_1 \right), \tag{II.2.9}$$

with $g_1^2 + g_2^2 + g_3^2 = 1$. Provided the $\{\boldsymbol{D}_j\}$'s be defined such that they constitute a Bishop frame, the former two expressions considerably simplify as $U_3(S) = 0$.

The attitude of the rod cross section being uniquely defined by the director $\boldsymbol{d}_3$, the knowledge of the angle between either director $\boldsymbol{d}_1$ or $\boldsymbol{d}_2$ and a specified direction is sufficient to fully characterize the rod spatial configuration. Although straightforward, the characterization of this rotation by means of the register angle ϕ between the pair $\{\boldsymbol{d}_1, \boldsymbol{d}_2\}$ and the normal and binormal to the space curve $\mathscr{E}$, *cf.* equations (II.1.7–II.1.8), may lead to uniqueness and continuity issues as the Frenet-Serret apparatus ceases to be defined at inflection points, *i.e.*, where $\kappa = 0$. Alternatively, the rotation of the rod cross section about the director $\boldsymbol{d}_3$ can be described with respect to the pair $\{\boldsymbol{k}_1, \boldsymbol{k}_2\}$

$$\boldsymbol{d}_1 = \cos\varphi\, \boldsymbol{k}_1 + \sin\varphi\, \boldsymbol{k}_2, \tag{II.2.10}$$

$$\boldsymbol{d}_2 = -\sin\varphi\, \boldsymbol{k}_1 + \cos\varphi\, \boldsymbol{k}_2, \tag{II.2.11}$$

where the unit vectors $\boldsymbol{k}_1$ and $\boldsymbol{k}_2$ are the images of $\boldsymbol{D}_1$ and $\boldsymbol{D}_2$, respectively, through the rotation mapping $\boldsymbol{D}_3$ on $\boldsymbol{d}_3$, see Figure II.2.1(b). Rodrigues formula (Cheng and Gupta, 1989) yields

$$\boldsymbol{k}_j = \boldsymbol{D}_j + \boldsymbol{\vartheta} \times \boldsymbol{D}_j + \boldsymbol{\vartheta} \times (\boldsymbol{\vartheta} \times \boldsymbol{D}_j) / (1 + \cos\theta), \tag{II.2.12}$$

where $\cos\theta = g_3$ and $\boldsymbol{\vartheta} = \boldsymbol{D}_3 \times \boldsymbol{d}_3$, with $\|\boldsymbol{\vartheta}\| = \sin\theta$, is the vector describing the axis of rotation. Additionally defining $\boldsymbol{k}_3 = \boldsymbol{d}_3$, the triplet $\{\boldsymbol{k}_j\}$ constitutes a right-handed orthonormal basis that coincides with the directors for $\cos\varphi = 1$ and degenerates into the $\boldsymbol{D}_j$–basis for $\cos\theta = 1$, *i.e.*, for $\boldsymbol{\vartheta} = \boldsymbol{0}$. The rotation axis indeed reads $\boldsymbol{\vartheta}(S) = g_1\, \boldsymbol{D}_2 - g_2\, \boldsymbol{D}_1$ such that equation (II.2.12)

leads to

$$\boldsymbol{k}_1(S) = \left(1 - \frac{g_1^2}{1+g_3}\right)\boldsymbol{D}_1 - \frac{g_1\, g_2}{1+g_3}\boldsymbol{D}_2 - g_1\,\boldsymbol{D}_3, \tag{II.2.13}$$

$$\boldsymbol{k}_2(S) = -\frac{g_1\, g_2}{1+g_3}\boldsymbol{D}_1 + \left(1 - \frac{g_2^2}{1+g_3}\right)\boldsymbol{D}_2 - g_2\,\boldsymbol{D}_3, \tag{II.2.14}$$

$$\boldsymbol{k}_3(S) = g_1\,\boldsymbol{D}_1 + g_2\,\boldsymbol{D}_2 + g_3\,\boldsymbol{D}_3. \tag{II.2.15}$$

Entirely defined by the three Eulerian functions g_j, this *intermediate* basis attached to $\mathscr{C}$ provides a simple way to describe the orientation of the directors with respect to the known $\{\boldsymbol{D}_j\}$–basis as well as the rudiments to re-express the strain variables in terms of Eulerian functions. Henceforth, tildes will be used to distinguish components of vectorial quantities in the $\{\boldsymbol{k}_j\}$–basis from their counterpart in the directors basis, *e.g.* $u_j = \boldsymbol{u}\cdot\boldsymbol{d}_j$ and $\widetilde{u}_j = \boldsymbol{u}\cdot\boldsymbol{k}_j$.

Analogously to relation (II.1.2) for the directors, the kinematic of the intermediate $\{\boldsymbol{k}_j\}$–basis along the rod centerline is described by a *fictitious* twist vector $\boldsymbol{w} = \widetilde{w}_j\,\boldsymbol{k}_j$ defined such that

$$\frac{\mathrm{d}\boldsymbol{k}_j}{\mathrm{d}s} = \boldsymbol{w}\times\boldsymbol{k}_j, \tag{II.2.16}$$

and which differs from the actual twist vector $\boldsymbol{u}$ as a result of the relative rotation φ of the directors $\{\boldsymbol{d}_1, \boldsymbol{d}_2\}$ with respect to the pair $\{\boldsymbol{k}_1, \boldsymbol{k}_2\}$. Hence, in view of the kinematic relations (II.1.2) and (II.2.16), differentiation of expressions (II.2.10–II.2.11) leads to $\boldsymbol{u} = \boldsymbol{w} + J_1\,\varphi'\,\boldsymbol{d}_3$ for the twist vector and

$$u_1(S) = \widetilde{w}_1\cos\varphi + \widetilde{w}_2\sin\varphi, \tag{II.2.17}$$

$$u_2(S) = -\widetilde{w}_1\sin\varphi + \widetilde{w}_2\cos\varphi, \tag{II.2.18}$$

$$u_3(S) = \widetilde{w}_3 + J_1\,\varphi', \tag{II.2.19}$$

for the strain variables. The components $\widetilde{w}_1(S)$ and $\widetilde{w}_2(S)$ are the projections of $\mathrm{d}\boldsymbol{d}_3/\mathrm{d}s = \alpha\,\kappa\,\boldsymbol{n}$ on $\boldsymbol{k}_1$ and $\boldsymbol{k}_2$, respectively, while $\widetilde{w}_3(S) = w_3$ may be interpreted as the twist density associated with the rotation of the pair $\{\boldsymbol{k}_1, \boldsymbol{k}_2\}$ about $\boldsymbol{k}_3$. Their expressions, in terms of the Eulerian quantities, are obtained by substituting the definition (II.2.12) for the $\boldsymbol{k}_j$'s in the projection of equation (II.2.16) on the $\{\boldsymbol{k}_j\}$–basis

$$\widetilde{w}_1(S) = \frac{\mathrm{d}\boldsymbol{k}_2}{\mathrm{d}s}\cdot\boldsymbol{k}_3 = J_1\left(\widetilde{U}_1 - g_2' + \frac{g_2\, g_3'}{1+g_3}\right), \tag{II.2.20}$$

$$\widetilde{w}_2(S) = \frac{\mathrm{d}\boldsymbol{k}_3}{\mathrm{d}s}\cdot\boldsymbol{k}_1 = J_1\left(\widetilde{U}_2 + g_1' - \frac{g_1\, g_3'}{1+g_3}\right), \tag{II.2.21}$$

$$\widetilde{w}_3(S) = \frac{\mathrm{d}\boldsymbol{k}_1}{\mathrm{d}s}\cdot\boldsymbol{k}_2 = J_1\left(\widetilde{U}_3 - \frac{g_1\, g_2' - g_1'\, g_2}{1+g_3}\right). \tag{II.2.22}$$

These relations emphasize that the kinematics of the $\{\boldsymbol{k}_j\}$–basis may be decomposed into the kinematics of the $\{\boldsymbol{D}_j\}$–basis, characterized by the Darboux vector $\boldsymbol{U}(S)$, and its rotation with respect to this basis. The components $\widetilde{U}_j(S)$ of $\boldsymbol{U}(S)$ in the $\{\boldsymbol{k}_j\}$–basis read

$$\widetilde{U}_1(S) = \left(1 - \frac{g_1^2}{1+g_3}\right) U_1 - \frac{g_1\, g_2\, U_2}{1+g_3} - g_1\, U_3, \tag{II.2.23}$$

$$\widetilde{U}_2(S) = -\frac{g_1\, g_2\, U_1}{1+g_3} + \left(1 - \frac{g_2^2}{1+g_3}\right) U_2 - g_2\, U_3, \tag{II.2.24}$$

$$\widetilde{U}_3(S) = g_1\, U_1 + g_2\, U_2 + g_3\, U_3, \tag{II.2.25}$$

with $U_j(S) = \boldsymbol{U} \cdot \boldsymbol{D}_j$ and the g_j's given in equations (II.2.7–II.2.9).

In conclusion, through substitution of equations (II.2.10–II.2.11) and (II.2.17–II.2.19), the internal force and moment (II.1.14–II.1.15) read

$$\boldsymbol{F}(S) = \widetilde{F}_1\, \boldsymbol{k}_1 + \widetilde{F}_2\, \boldsymbol{k}_2 + A\,(\alpha - 1)\, \boldsymbol{k}_3, \tag{II.2.26}$$

$$\boldsymbol{M}(S) = B\,(\widetilde{w}_1\, \boldsymbol{k}_1 + \widetilde{w}_2\, \boldsymbol{k}_2) + C\,(\widetilde{w}_3 + J_1\, \varphi')\, \boldsymbol{k}_3, \tag{II.2.27}$$

where the $\widetilde{w}_j(S)$ are given in equations (II.2.20–II.2.22). Provided that the body force and body couple per unit reference length may be expressed as functions of the Eulerian curvilinear coordinate, *viz.* $\boldsymbol{f}(S) = \boldsymbol{f}(S(s))$ and $\boldsymbol{m}(S) = \boldsymbol{m}(S(s))$, the balance of linear and angular momenta (II.1.12–II.1.13) may be expressed as

$$J_1 \frac{\mathrm{d}\boldsymbol{F}}{\mathrm{d}S} + \boldsymbol{f} = \boldsymbol{0}, \tag{II.2.28}$$

$$J_1 \frac{\mathrm{d}\boldsymbol{M}}{\mathrm{d}S} + \alpha\, \boldsymbol{k}_3 \times \boldsymbol{F} + \boldsymbol{m} = \boldsymbol{0}, \tag{II.2.29}$$

where, according to relations (II.2.3) and (II.2.4), the Jacobian reads

$$J_1(S) = \frac{\alpha}{\sqrt{(\Delta_1' - \Delta_2\, U_3)^2 + (\Delta_2' + \Delta_1\, U_3)^2 + (1 - \Delta_1\, U_2 + \Delta_2\, U_1)^2}}, \tag{II.2.30}$$

which complete the Eulerian formulation. Eventually, the clamped-sliding sleeve boundary conditions (II.1.16–II.1.17) are reformulated within the Eulerian framework as

$$\{\boldsymbol{\Delta}(S_a), \boldsymbol{k}_1(S_a), \boldsymbol{k}_2(S_a)\}, \tag{II.2.31}$$

and

$$\{\boldsymbol{\Delta}(S_b), \boldsymbol{k}_3(S_b), F_3(S_a), M_3(S_b)\}, \tag{II.2.32}$$

at the extremities $S_a < S_b$ of the elementary boundary value problem corresponding to the rod extremities s_a and s_b, respectively. In the following Section, we proceed to the nondimensionalization of this Eulerian formulation.

II.2.3 Dimensionless governing equations and boundary conditions

Both the Eulerian coordinate S and the components of the eccentricity vector are naturally scaled by the known length of the boundary value problem, $L = S_b - S_a$, leading to the introduction of the dimensionless curvilinear coordinate $\xi = (S - S_a)/L$ and eccentricity vector $\boldsymbol{\delta}(\xi) = \delta_1 \boldsymbol{D}_1 + \delta_2 \boldsymbol{D}_2$ with

$$\delta_1(\xi) = \Delta_1(S(\xi))/L, \qquad \delta_2(\xi) = \Delta_2(S(\xi))/L. \tag{II.2.33}$$

Analogously scaling the Lagrangian and stretched curvilinear coordinates by L, the stretch is redefined as $\alpha(\xi) \coloneqq \alpha(S(\xi))$ while the Jacobians derivatives (II.2.5) read

$$\mathcal{J}_k(\xi) = L^{k-1} J_k(S(\xi)), \qquad \bar{\mathcal{J}}_k(\xi) = L^{k-1} \bar{J}_k(S(\xi)), \tag{II.2.34}$$

for $k \geq 1$. Considering the previous definitions and denoting the characteristic force $F^\star = B/L^2$, the scaling leads to the introduction of the following vector fields

$$\boldsymbol{\mathcal{F}}(\xi) = \boldsymbol{F}(S(\xi))/F^\star, \qquad \boldsymbol{\mathcal{M}}(\xi) = \boldsymbol{M}(S(\xi))/LF^\star, \tag{II.2.35}$$

$$\boldsymbol{\sigma}(\xi) = L\,\boldsymbol{f}(S(\xi))/F^\star, \qquad \boldsymbol{\mu}(\xi) = \boldsymbol{m}(S(\xi))/F^\star, \tag{II.2.36}$$

for the scaled internal force and moment, body force and body couple, respectively. According to this scaling and the constitutive relation (II.1.15), the dimensionless strain variables are analogous to the components of the scaled internal moment in the directors basis, that is

$$\mathcal{M}_1(\xi) = L\,u_1, \qquad \mathcal{M}_2(\xi) = L\,u_2, \qquad \mathcal{M}_3(\xi) = L\,u_3\,(1+\nu)^{-1}, \tag{II.2.37}$$

with $1 + \nu = B/C$ where, for rods with a circular cross section, ν is Poisson's ratio. Similarly, the fictitious twist vector and the Darboux vector scale as

$$\boldsymbol{\omega}(S) = L\,\boldsymbol{w}(S(\xi)), \qquad \boldsymbol{\mathcal{U}}(\xi) = L\,\boldsymbol{U}(S(\xi)), \tag{II.2.38}$$

such that the components (II.2.7–II.2.9) of the unit tangent $\boldsymbol{d}_3$ in the $\{\boldsymbol{D}_j\}$–basis become

$$g_1(\xi) = \bar{\mathcal{J}}_1(\delta_1' - \delta_2\,\mathcal{U}_3), \tag{II.2.39}$$

$$g_2(\xi) = \bar{\mathcal{J}}_1(\delta_2' + \delta_1\,\mathcal{U}_3), \tag{II.2.40}$$

$$g_3(\xi) = \bar{\mathcal{J}}_1(1 - \delta_1\,\mathcal{U}_2 + \delta_2\,\mathcal{U}_1), \tag{II.2.41}$$

where primes now denote differentiation with respect to the dimensionless coordinate ξ and, according to relations (II.2.3) and (II.2.4), the Jacobian reads

$$\bar{\mathcal{J}}_1(\xi) = \frac{1}{\sqrt{(\delta_1' - \delta_2 \mathcal{U}_3)^2 + (\delta_2' + \delta_1 \mathcal{U}_3)^2 + (1 - \delta_1 \mathcal{U}_2 + \delta_2 \mathcal{U}_1)^2}}, \tag{II.2.42}$$

with $\mathcal{U}_j = \boldsymbol{\mathcal{U}} \cdot \boldsymbol{D}_j$.

According to equations (II.2.26–II.2.27), the scaled internal force and moment (II.2.35) can entirely be re-expressed in terms of Eulerian functions as

$$\boldsymbol{\mathcal{F}}(\xi) = \widetilde{\mathcal{F}}_1 \boldsymbol{k}_1 + \widetilde{\mathcal{F}}_2 \boldsymbol{k}_2 + \eta^{-2}(\alpha - 1)\boldsymbol{k}_3, \tag{II.2.43}$$

$$\boldsymbol{\mathcal{M}}(\xi) = \widetilde{\omega}_1 \boldsymbol{k}_1 + \widetilde{\omega}_2 \boldsymbol{k}_2 + (1+\nu)^{-1}(\widetilde{\omega}_3 + \mathcal{J}_1 \varphi')\boldsymbol{k}_3, \tag{II.2.44}$$

where the rotation angle is redefined as $\varphi(\xi) \coloneqq \varphi(S(\xi))$; $\eta^2 = F^\star/A$ is a dimensionless parameter that tends to zero in the limit of inextensible rods; and the components (II.2.20–II.2.22) of the fictitious twist vector $\boldsymbol{\omega}(\xi)$ in the intermediate basis are given by

$$\widetilde{\omega}_1(\xi) = \mathcal{J}_1 \left(\widetilde{\mathcal{U}}_1 - g_2' + \frac{g_2\, g_3'}{1+g_3} \right), \tag{II.2.45}$$

$$\widetilde{\omega}_2(\xi) = \mathcal{J}_1 \left(\widetilde{\mathcal{U}}_2 + g_1' - \frac{g_1\, g_3'}{1+g_3} \right), \tag{II.2.46}$$

$$\widetilde{\omega}_3(\xi) = \mathcal{J}_1 \left(\widetilde{\mathcal{U}}_3 - \frac{g_1\, g_2' - g_1'\, g_2}{1+g_3} \right), \tag{II.2.47}$$

with $\mathcal{J}_1(\xi) = \alpha\, \bar{\mathcal{J}}_1$. Accordingly, the projection of the equilibrium equations (II.2.28–II.2.29) in the $\{\boldsymbol{k}_j\}$–basis yields

$$\mathcal{J}_1 \widetilde{\mathcal{F}}_1' + \eta^{-2}(\alpha - 1)\widetilde{\omega}_2 - \widetilde{\omega}_3 \widetilde{\mathcal{F}}_2 + \widetilde{\sigma}_1 = 0, \tag{II.2.48}$$

$$\mathcal{J}_1 \widetilde{\mathcal{F}}_2' + \widetilde{\omega}_3 \widetilde{\mathcal{F}}_1 - \eta^{-2}(\alpha - 1)\widetilde{\omega}_1 + \widetilde{\sigma}_2 = 0, \tag{II.2.49}$$

$$\mathcal{J}_1 \alpha' + \eta^2 \left(\widetilde{\omega}_1 \widetilde{\mathcal{F}}_2 - \widetilde{\omega}_2 \widetilde{\mathcal{F}}_1 + \widetilde{\sigma}_3 \right) = 0, \tag{II.2.50}$$

$$\mathcal{J}_1 \widetilde{\omega}_1' - \frac{\widetilde{\omega}_2}{1+\nu}(\nu\, \widetilde{\omega}_3 - \mathcal{J}_1 \varphi') - \alpha \widetilde{\mathcal{F}}_2 + \widetilde{\mu}_1 = 0, \tag{II.2.51}$$

$$\mathcal{J}_1 \widetilde{\omega}_2' + \frac{\widetilde{\omega}_1}{1+\nu}(\nu\, \widetilde{\omega}_3 - \mathcal{J}_1 \varphi') + \alpha \widetilde{\mathcal{F}}_1 + \widetilde{\mu}_2 = 0, \tag{II.2.52}$$

$$\mathcal{J}_1^2 \varphi'' + \mathcal{J}_2 \varphi' + \mathcal{J}_1 \widetilde{\omega}_3' + (1+\nu)\widetilde{\mu}_3 = 0, \tag{II.2.53}$$

with $\widetilde{\sigma}_j(\xi) = \boldsymbol{\sigma} \cdot \boldsymbol{k}_j$ and $\widetilde{\mu}_j(\xi) = \boldsymbol{\mu} \cdot \boldsymbol{k}_j$. Further substitution of the definitions (II.2.45–II.2.47) for the $\widetilde{\omega}_j$'s and (II.2.39–II.2.41) for the g_j's, leads to a mixed order system of six differential equations involving three first order, (II.2.48–II.2.50), in α and the $\widetilde{\mathcal{F}}_i$'s; one second order, (II.2.53), in φ; and two third order, (II.2.51–II.2.52), in the δ_i's (with $i = 1, 2.$) Although simply

derived, the resulting system is cumbersome and will not be explicitly presented here.

This system consequently requires the specification of eleven constants of integration. The Eulerian counterpart to the boundary conditions (II.1.16) prescribing the clamped extremity of the rod reads

$$\{\varphi(0), \delta_i(0), \delta_i'(0)\}, \tag{II.2.54}$$

with $i = 1, 2$. At the end S_b of the boundary value problem, the rod remains free to move smoothly through a frictionless sliding sleeve, whose position is fixed in space. Both eccentricity and inclination of the rod with respect to the reference curve must therefore be imposed. Additionally, according to the constitutive relations (II.2.43–II.2.44), the known axial force and twisting moment acting at this extremity also require to prescribe the stretch and the first derivative of the angle φ. Hence, the boundary conditions (II.1.17) become

$$\{\alpha(1), \varphi'(1), \delta_i(1), \delta_i'(1)\}, \tag{II.2.55}$$

with $i = 1, 2$. As an essential outcome of the proposed reformulation, the isoperimetric constraints, a source of difficulty in the Lagrangian formulation, disappear and the system of equations (II.2.48–II.2.53) with the boundary conditions (II.2.54–II.2.55) constitute a classical boundary value problem. Note that the proposed Eulerian reformulation of the rod governing equations could be extended to other boundary conditions.

In conclusion, it has been shown that the rod configuration, entirely defined by $\boldsymbol{r}(s)$ and $\boldsymbol{d}_1(s)$ in the Lagrangian formulation (II.1.1), reduces to the knowledge of the three Eulerian functions

$$[0, 1] \ni \xi \mapsto \varphi(\xi), \delta_1(\xi), \delta_2(\xi) \in \mathbb{R}, \tag{II.2.56}$$

with the boundaries $\xi = \{0, 1\}$ of the elementary problem corresponding to the rod extremities s_a and s_b, respectively. While the components δ_1, δ_2 of the eccentricity vector describe the rod relative position with respect to the reference curve, the angle φ characterizes the rotation of the rod cross section about the director $\boldsymbol{d}_3$. This representation of elastic rods leads to a reduced coordinate formulation involving a minimal number of degrees of freedom similar to the *curve-angle* representations proposed in Langer and Singer (1996); Bergou et al. (2008, 2010). In this formulation, the centerline is explicitly represented and the material frame is characterized by a unique angle.

Besides the suppression of the isoperimetric constraints, the proposed Eulerian reformulation of the rod governing equations drastically simplifies the assessment of the unilateral contact condition, which requires the evaluation of the distance between the two curves $\mathscr{C}$ and $\mathscr{E}$ (parameterized by distinct curvilinear coordinates in the classical Lagrangian formulation.) Specifically, the description of the rod deformed configuration through its relative position with respect to the constraint axis provides a straightforward means to detect the appearance of new contacts

or, depending on the elementary problem under consideration, ensure that the rod remains in continuous contact with the constraining surface. More precisely:

Free rod The *a posteriori* assessment of the unilateral contact condition along contact-free problems is drastically simplified as it reduces to ensure that a threshold on the magnitude of the eccentricity vector is not violated. This constraint, indeed, merely consists in checking that either $\|\boldsymbol{\delta}\| < \epsilon$ or $\|\boldsymbol{\delta}\| > \epsilon$, with the scaled constraint radius $\epsilon(\xi) = Q(S(\xi))/L$, for interior and exterior configurations, respectively.

Continuous contact Alternatively, although the magnitude of the eccentricity vector is known along continuous contact problems, the magnitude of the reaction pressure $\boldsymbol{\rho}(\xi)$ included in the body force $\boldsymbol{\sigma}(\xi)$ and acting normally to the constraint surface is *a priori* unknown. The nonlinear boundary value problem (II.2.48–II.2.55) is therefore supplemented by the relation $\|\boldsymbol{\delta}\| = \epsilon$ to close the formulation and ensure the continuous contact along the whole domain.

II.2.4 Small inclination approximation

The previous developments lead to the rigorous reformulation of the special Cosserat rod theory within the Eulerian framework associated with the reference curve. Although this reformulation hinges on the description of the rod deformed configuration by means of its relative deflection about $\mathscr{C}$, no assumptions were made on the magnitude of $\boldsymbol{\delta}(\xi)$. Along interior problems, the rod eccentricity is however expected to be at most equal to the constraint radius, while for many typical exterior problems, the rod remains within close range of the reference curve such that the norm $\|\boldsymbol{\delta}\|$ be of the order of the constraint radius. The following rescaling of the eccentricity vector is therefore naturally proposed

$$\boldsymbol{\delta}(\xi) = \varepsilon\, \overline{\boldsymbol{\delta}} \tag{II.2.57}$$

with $\overline{\boldsymbol{\delta}}(\xi) = \overline{\delta}_1 \boldsymbol{D}_1 + \overline{\delta}_2 \boldsymbol{D}_2$ and ε a representative value of $\epsilon(\xi)$ along the elementary problem under consideration such that $\|\overline{\boldsymbol{\delta}}\| = \mathcal{O}(1)$ as $\varepsilon \to 0$. For small values of $\|\boldsymbol{\delta}\|$, *i.e.*, for $\varepsilon \ll 1$, the space curve $\mathscr{E}$ may be seen as a perturbation of the reference curve and the distinction between Eulerian and stretched coordinates becomes negligible provided the rod relative deflection remains reasonably small compared to the radius of curvature of the reference curve. The conditions under which the nonlinear system (II.2.48–II.2.53) can be simplified accordingly are investigated next.

For eccentricities of order ε such as previously defined, the inclination of the rod on the reference curve is expected to be comparably small, that is $\theta(\xi) = \mathcal{O}(\varepsilon)$ as $\varepsilon \to 0$, and, consequently, the $\{\boldsymbol{k}_j\}$–basis to be expressed as a perturbation of the $\{\boldsymbol{D}_j\}$–basis attached to the reference curve. Expanding the rotation vector $\boldsymbol{\vartheta}(\xi) = \boldsymbol{D}_3 \times \boldsymbol{k}_3$ in powers of ε and inserting the resulting

expression in the definition (II.2.12) of the intermediate basis, leads to

$$\boldsymbol{k}_j(\xi) = \boldsymbol{D}_j + \varepsilon\,\boldsymbol{k}_j^{(1)} + \varepsilon^2\,\boldsymbol{k}_j^{(2)} + \mathcal{O}\left(\varepsilon^3\right), \tag{II.2.58}$$

as $\varepsilon \to 0$, where the first corrections read

$$\boldsymbol{k}_j^{(1)}(\xi) = \boldsymbol{\vartheta}^{(1)} \times \boldsymbol{D}_j, \qquad \boldsymbol{k}_j^{(2)}(\xi) = \frac{1}{2}\left(\boldsymbol{\vartheta}^{(1)} \times \boldsymbol{k}_j^{(1)}\right), \tag{II.2.59}$$

such that the intermediate basis remains orthonormal at each order. The vector $\boldsymbol{\vartheta}(\xi)$ being, by definition, orthogonal to $\boldsymbol{D}_3(\xi)$, it may be expressed as

$$\boldsymbol{\vartheta}(\xi) = \varepsilon\,\boldsymbol{\vartheta}^{(1)} + \varepsilon^3\,\boldsymbol{\vartheta}^{(3)} + \mathcal{O}\left(\varepsilon^5\right), \tag{II.2.60}$$

for $\varepsilon \to 0$, where the corrections read $\boldsymbol{\vartheta}^{(k)}(\xi) = \vartheta_{1,k}\,\boldsymbol{D}_1 + \vartheta_{2,k}\,\boldsymbol{D}_2$ with $\vartheta_{1,k}(\xi)$ and $\vartheta_{2,k}(\xi)$ functions of the $\overline{\boldsymbol{\delta}}(\xi)$ and $\boldsymbol{\mathcal{U}}(\xi)$ components.

Comparison of expression (II.2.58) with the definition of the intermediate basis in terms of the $g_j(\xi)$'s, see equations (II.2.13–II.2.15), allows to identify the perturbation expansions for the components of the director $\boldsymbol{d}_3$ in terms of the $\overline{\delta}_i(\xi)$'s and $\mathcal{U}_j(\xi)$'s. Limiting these developments to twist-free $\{\boldsymbol{D}_j\}$–bases, *i.e.*, Bishop frames, the only nonzero components of the Darboux vector $\boldsymbol{\mathcal{U}}(\xi)$ are of the order of the reference curve curvature $\mathcal{K}(\xi) = \sqrt{\mathcal{U}_1^2 + \mathcal{U}_2^2}$. Therefore, redefining these components as

$$\mathcal{U}_1(\xi) = \mathcal{K}\,\sin\Phi, \qquad \mathcal{U}_2(\xi) = \mathcal{K}\,\cos\Phi, \tag{II.2.61}$$

where $\tan\Phi = \mathcal{U}_1/\mathcal{U}_2$ is the angle between the pair $\{\boldsymbol{D}_1, \boldsymbol{D}_2\}$ and the normal and binormal to $\mathscr{C}$, the components (II.2.39–II.2.41) become

$$g_1(\xi) = \varepsilon\,\overline{\delta}_1' + \varepsilon^2\,\mathcal{K}\,\overline{\delta}_1'\left(\overline{\delta}_1\,\cos\Phi - \overline{\delta}_2\,\sin\Phi\right) + \mathcal{O}\left(\varepsilon^3\right), \tag{II.2.62}$$

$$g_2(\xi) = \varepsilon\,\overline{\delta}_2' + \varepsilon^2\,\mathcal{K}\,\overline{\delta}_2'\left(\overline{\delta}_1\,\cos\Phi - \overline{\delta}_2\,\sin\Phi\right) + \mathcal{O}\left(\varepsilon^3\right), \tag{II.2.63}$$

$$g_3(\xi) = 1 - \frac{\varepsilon^2}{2}\left(\overline{\delta}_1'^2 + \overline{\delta}_2'^2\right) + \mathcal{O}\left(\varepsilon^3\right), \tag{II.2.64}$$

as $\varepsilon \to 0$.

Considering only the leading order terms, the Jacobian of the mapping from stretched to Eulerian coordinates reduces to

$$\bar{\mathcal{J}}_1(\xi) = 1 + \varepsilon\,\mathcal{K}\left(\overline{\delta}_1\,\cos\Phi - \overline{\delta}_2\,\sin\Phi\right) + \mathcal{O}\left(\varepsilon^2\right), \tag{II.2.65}$$

as $\varepsilon \to 0$, which emphasizes that the drift between these two curvilinear coordinates becomes negligible either for reasonably small curvature of the reference curve or when the eccentricity vector $\boldsymbol{\delta}(\xi)$ is orthogonal to the osculating plane to $\mathscr{C}$, *i.e.*, when the eccentricity of the rod

does not *contribute* to its curvature. In many applications, the reference curve is only slightly tortuous and its radius of curvature is large compared to the length L of the problem. Hence, assuming the product $\varepsilon\,\mathcal{K} = \mathcal{O}(\varepsilon^2)$ for $\varepsilon \to 0$, the third terms in equations (II.2.62) and (II.2.63) become negligible and the Jacobians reduce to $\widetilde{\mathcal{J}}_1(\xi) = 1 + \mathcal{O}(\varepsilon^2)$ and $\mathcal{J}_1(\xi) = \alpha + \mathcal{O}(\varepsilon^2)$. Consequently, the components (II.2.45–II.2.47) of the fictitious twist vector read

$$\widetilde{\omega}_1(\xi) = \alpha\,\mathcal{K}\,\sin\Phi - \alpha\,\varepsilon\,\overline{\delta}_2'' + \mathcal{O}\left(\varepsilon^2\right), \tag{II.2.66}$$

$$\widetilde{\omega}_2(\xi) = \alpha\,\mathcal{K}\,\cos\Phi + \alpha\,\varepsilon\,\overline{\delta}_1'' + \mathcal{O}\left(\varepsilon^2\right), \tag{II.2.67}$$

$$\widetilde{\omega}_3(\xi) = \mathcal{O}\left(\varepsilon^2\right), \tag{II.2.68}$$

for $\varepsilon \to 0$, leading to a substantial simplification of the governing system of equations (II.2.48–II.2.53). From equations (II.2.51–II.2.52), the shear components of the internal force in the $\{\boldsymbol{k}_j\}$–basis for instance become

$$\begin{aligned}\widetilde{\mathcal{F}}_1(\xi) = &-(\alpha\,\mathcal{K}' + \alpha'\,\mathcal{K})\cos\Psi + \left(\alpha\,\Psi' + \alpha\frac{\varphi'}{1+\nu}\right)\mathcal{K}\,\sin\Psi \\ &+ \varepsilon\left[\alpha'\,\overline{\delta}_1'' + \alpha\,\overline{\delta}_1''' + \alpha\frac{\varphi'}{1+\nu}\alpha\overline{\delta}_2''\right] + \mathcal{O}\left(\varepsilon^2\right),\end{aligned} \tag{II.2.69}$$

$$\begin{aligned}\widetilde{\mathcal{F}}_2(\xi) = &(\alpha\,\mathcal{K}' + \alpha'\,\mathcal{K})\sin\Psi + \left(\alpha\,\Psi' + \alpha\frac{\varphi'}{1+\nu}\right)\mathcal{K}\,\cos\Psi \\ &- \varepsilon\left[\alpha'\,\overline{\delta}_2'' + \alpha\,\overline{\delta}_2''' - \alpha\frac{\varphi'}{1+\nu}\overline{\delta}_1''\right] + \mathcal{O}\left(\varepsilon^2\right),\end{aligned} \tag{II.2.70}$$

in the absence of body couple, while according to equations (II.2.17–II.2.19) and (II.2.37), the scaled strain variables may be expressed as

$$\mathcal{M}_1(\xi) = \alpha\,\mathcal{K}\,\sin(\Phi+\varphi) + \alpha\,\varepsilon\left(\overline{\delta}_1''\sin\varphi - \overline{\delta}_2''\cos\varphi\right) + \mathcal{O}\left(\varepsilon^2\right), \tag{II.2.71}$$

$$\mathcal{M}_2(\xi) = \alpha\,\mathcal{K}\,\cos(\Phi+\varphi) + \alpha\,\varepsilon\left(\overline{\delta}_1''\cos\varphi + \overline{\delta}_2''\sin\varphi\right) + \mathcal{O}\left(\varepsilon^2\right), \tag{II.2.72}$$

$$\mathcal{M}_3(\xi) = \frac{\alpha}{1+\nu}\varphi' + \mathcal{O}\left(\varepsilon^2\right), \tag{II.2.73}$$

for $\varepsilon \to 0$.

In practice, the domain of applicability of this small scale approximation of the Eulerian formulation may seem relatively restricted as it requires that $\mathcal{K} = \mathcal{O}(\varepsilon)$ for $\varepsilon \to 0$. It is however shown in Section II.3.3, that it provides remarkably good results for the internal force and moment, even for a curvature of the reference curve of order 1. The main interest of this approximation actually resides in its propensity to stress how the tortuosity of the reference curve affects the transmission of the internal force and moment. Finally, within a numerical scheme, this approximation could be used as an initial guess for a solver.

II.3 Validation and applications

As suggested in the introduction, the range of disciplines and applications concerned with the constrained deformation of a slender elastic body is potentially very wide. Exploring all the possible features of the proposed Eulerian reformulation exceeds the scope of this Chapter and, merely, a few of its benefits and limitations are highlighted in the following. Considering a series of fundamental problems, the validity of the method is assessed by comparison with known analytical results and numerical solutions obtained using the Lagrangian formulation.

II.3.1 Planar elastica

Planar deflection can either result from the rod cross section geometry and loading symmetry (these solutions do not need to be stable) or be imposed by external constraints (in which case the transversal force is not necessarily null.) The purely bi-dimensional configuration corresponding to the external constraint $\boldsymbol{d}_2(\xi) = \boldsymbol{e}_2$ is investigated here by assuming $\delta_2(\xi) = 0$ and a planar reference curve. The $\{\boldsymbol{D}_j\}$–basis attached to $\mathscr{C}$ is defined such that $\boldsymbol{D}_2(\xi) = \boldsymbol{e}_2$; hence the only non-null component of the Darboux vector $\boldsymbol{\mathcal{U}}(\xi) = \mathcal{U}_2 \boldsymbol{D}_2$ corresponds to the curvature of the reference curve.

Consequently, the components of the director $\boldsymbol{d}_3$ in the frame attached to the reference curve, *cf.* Equations (II.2.39–II.2.41), reduce to

$$g_1(\xi) = \bar{\mathcal{J}}_1 \delta_1', \qquad g_2(\xi) = 0, \qquad g_3(\xi) = \bar{\mathcal{J}}_1 (1 - \delta_1 \mathcal{U}_2), \tag{II.3.1}$$

where the Jacobian (II.2.42) from Eulerian to stretched coordinates is given by

$$\bar{\mathcal{J}}_1(\xi) = \frac{1}{\sqrt{\delta_1'^2 + (1 - \delta_1 \mathcal{U}_2)}}. \tag{II.3.2}$$

The only non-null component of the fictitious twist vector (II.2.45–II.2.47) therefore reads

$$\widetilde{\omega}_2(\xi) = \bar{\mathcal{J}}_1^3 \left(\mathcal{U}_2 + \delta_1'' - 2\delta_1 \mathcal{U}_2^2 + \delta_1^2 \mathcal{U}_2^3 + 2\delta_1'^2 \mathcal{U}_2 - \delta_1 \delta_1'' \mathcal{U}_2 - \delta_1 \delta_1' \mathcal{U}_2' \right), \tag{II.3.3}$$

which is the curvature of the rod. Hence, according to equations (II.2.17–II.2.19) and (II.2.37), the strain variables reduce to

$$\mathcal{M}_1 = \alpha \widetilde{\omega}_2 \sin\varphi, \qquad \mathcal{M}_2 = \alpha \widetilde{\omega}_2 \cos\varphi, \qquad \mathcal{M}_3 = \mathcal{J}_1 \frac{\varphi'}{1+\nu}. \tag{II.3.4}$$

For inextensible rods, *i.e.*, for $\alpha(\xi) = 1$, and assuming no rotation of the rod cross section about its axis, *i.e.*, $\varphi'(\xi) = 0$, we recover the Eulerian formulation proposed by Denoël and Detournay (2011) for a constrained elastica.

II.3.2 Straight conduit

The helical buckling and post-buckling behavior of a rod within a cylindrical constraint has been extensively studied (Seemann, 1996; Thompson and Champneys, 1996; Goriely and Tabor, 1997c; van der Heijden, 2001; van der Heijden et al., 2002; Thompson et al., 2012) not only due to the major interest it represents to several areas of science and engineering (*e.g.,* mechanics of climbing in twining plants, drilling industry, fittings in overhead transmission lines or buckling of optical fibers in loose-tube packaging) but also as a result of the position this fundamental problem occupies in advanced continuum mechanics. Here, it is shown that well-known results associated with twisted elastic rods can easily be recovered from the proposed Eulerian formulation of the rod governing equations.

Along a straight reference curve framed by a constant $\{\boldsymbol{D}_j\}$–basis, the rod assumes a helical deflection with radius δ and pitch angle θ provided the components of the eccentricity vector satisfy

$$\delta_1(\xi) = \delta\cos(2\pi\,\xi/\lambda), \qquad \delta_2(\xi) = \delta\sin(2\pi\,\xi/\lambda), \tag{II.3.5}$$

where $\lambda = 2\pi\,\delta/\tan\theta$ is the helix axial wavelength or pitch. Note that the pitch angle θ is also the inclination of the rod on the reference curve as defined in equation (II.2.12). The Jacobian (II.2.42) of the mapping from Eulerian to Lagrangian coordinates reduces then to $\mathcal{J}_1(\xi) = \alpha\cos\theta$ and, restricting ourselves to weightless rods and frictionless contact, the reaction pressure $\boldsymbol{\rho}(\xi)$ is equivalent to a body force acting normally to the constraint surface, *i.e.*, $\boldsymbol{\rho}\cdot\boldsymbol{D}_3 = 0$. It may therefore be convenient to decompose the shear forces between their normal $\mathcal{F}_n$ and geodesic $\mathcal{F}_g$ components

$$\mathcal{F}_1(\xi) = \mathcal{F}_n\cos(2\pi\,\xi/\lambda) - \mathcal{F}_g\sin(2\pi\,\xi/\lambda), \tag{II.3.6}$$

$$\mathcal{F}_2(\xi) = \mathcal{F}_n\sin(2\pi\,\xi/\lambda) + \mathcal{F}_g\cos(2\pi\,\xi/\lambda), \tag{II.3.7}$$

with $\mathcal{F}_n = \boldsymbol{\mathcal{F}}\cdot\boldsymbol{N}$ and $\mathcal{F}_g = \boldsymbol{\mathcal{F}}\cdot(\boldsymbol{N}\times\boldsymbol{d}_3)$ where $\boldsymbol{N}(\xi) = \cos(2\pi\,\xi/\lambda)\,\boldsymbol{D}_1 + \sin(2\pi\,\xi/\lambda)\,\boldsymbol{D}_2$. Hence, substituting expressions (II.3.5) for δ_1 and δ_2 in the components (II.2.45–II.2.47) of the fictitious twist vector lead to

$$\begin{aligned}
\widetilde{\omega}_1(\xi) &= \alpha\,\sin^2\theta\,\sin(2\pi\,\xi/\lambda)/\delta,\\
\widetilde{\omega}_2(\xi) &= -\alpha\,\sin^2\theta\,\cos(2\pi\,\xi/\lambda)/\delta,\\
\widetilde{\omega}_3(\xi) &= \alpha\,\sin\theta\,(1-\cos\theta)/\delta,
\end{aligned}$$

such that the equilibrium equations (II.2.51) and (II.2.52) yield

$$\mathcal{F}_n(\xi) = \frac{\alpha'}{\delta}\cos\theta\,\sin^2\theta, \tag{II.3.8}$$

$$\mathcal{F}_g(\xi) = \frac{\alpha}{(1+\nu)\,\delta^2}\cos\theta\,\sin^2\theta\,[\tan\theta\,(1+\nu\,\cos\theta) - \delta\,\varphi']\,. \tag{II.3.9}$$

Considering exclusively solutions homoclinic to the straight unbuckled configuration (*i.e.*, asymptotically straight towards both ends), the torque reads $\mathcal{M}_3 = \mathcal{M}$ such that the rod carries about its own material axis the applied end twisting moment $\mathcal{M} = \boldsymbol{\mathcal{M}}\cdot\boldsymbol{D}_3$ (Love, 1927; van der Heijden and Thompson, 2000; Thompson et al., 2012). According to equations (II.2.50) and (II.2.53), the stretch α and the angle φ read

$$\alpha(\xi) = \frac{\eta^2\mathcal{T} + \cos\theta}{\cos\theta + \frac{\eta^2}{\delta^2}\sin^4\theta}, \tag{II.3.10}$$

$$\varphi(\xi) = \varphi(0) + \xi\frac{\tan\theta\,[2+\nu\,(1+\cos\theta)]}{\delta}, \tag{II.3.11}$$

where $\mathcal{T} = \boldsymbol{\mathcal{F}}\cdot\boldsymbol{D}_3$ denotes the applied end force, such that the twisting moment is given by

$$\mathcal{M} = \frac{\sin\theta\,(1+\cos\theta)\left(\cos\theta + \eta^2\,\mathcal{T}\right)}{\delta\left(\cos\theta + \frac{\eta^2}{\delta^2}\sin^4\theta\right)}. \tag{II.3.12}$$

Finally, equations (II.2.48) and (II.2.49) lead to

$$\rho(\xi) = \alpha\left(\frac{\alpha - 1 + \eta^2\,\mathcal{F}_g\,\cot\theta}{\delta\,\eta^2}\sin^2\theta - \mathcal{F}_n'\cos\theta\right), \tag{II.3.13}$$

for the magnitude of the reaction. The helical buckling and post-buckling of both the free rod and the rod in continuous contact with the cylindrical restraint are investigated in the following.

II.3.2.1 Free rod

In particular, the reaction pressure vanishes along the free helix and equations (II.3.12–II.3.13) with (II.3.8–II.3.11) relate the helix attributes $\{\delta, \theta\}$ to the end loading $\{\mathcal{M}, \mathcal{T}\}$

$$\delta\,\mathcal{M} = \frac{\sin\theta\,(1+\cos\theta)}{1 - \frac{\eta^2}{\delta^2}\sin^2\theta\,\cos\theta}, \qquad \delta^2\mathcal{T} = \frac{\sin^2\theta}{1 - \frac{\eta^2}{\delta^2}\sin^2\theta\,\cos\theta}, \tag{II.3.14}$$

or, defining the *loading parameter* $m = \mathcal{M}/\sqrt{\mathcal{T}}$,

$$m = \frac{1+\cos\theta}{\sqrt{1 - \frac{\eta^2}{\delta^2}\sin^2\theta\cos\theta}}, \tag{II.3.15}$$

which extends the well-known relation $m = 1 + \cos\theta$ to extensible rods, *i.e.*, for $\eta \neq 0$. Substituting this relation in the former equilibrium conditions (II.3.14) to eliminate the pitch angle, the radius $\Gamma = \delta\sqrt{\mathcal{T}}$ can similarly be expressed as a function of both the loading parameter m and the ratio δ/η. These relations are presented in Figure II.3.1. Although the buckling load $m_b = 2$ is unaffected by the *reduced eccentricity* δ/η, it appears that this ratio significantly alters the post-buckling path. Beyond the subcritical buckling bifurcation, *i.e.*, for $m > 2$, and for $\delta/\eta > \sqrt{2}$ the only equilibrium solution is the unstable straight configuration whilst, for $\delta/\eta \in \left[\sqrt{2}/3^{3/4}, \sqrt{2}\right]$, two additional equilibrium solutions emerge as the loading parameter given in expression (II.3.15) admits a maximum

$$m^* = \frac{1+\cos\theta}{\sqrt{\frac{1+3\cos 2\theta}{4\cos\theta+\cos 2\theta-1}}}, \tag{II.3.16}$$

with $\theta \in [0, \arccos(-1/3)/2]$. For inextensible rods, a localized post-buckling path has, however, been observed experimentally Thompson and Champneys (1996); similar energetically favorable paths are most likely to exist for extensible rods and to be influenced by the values of the reduced excentricity δ/η.

For isotropic rods of circular cross section, the ratio δ/η reads $2\,\Delta/a$ and, therefore, relates the helix radius Δ to the rod radius a. The outset of Figure II.3.1 depicts the deformed configurations associated with five distinct values of this ratio for $\theta = \pi/5$ and $\mathcal{T} = 1$. Note that, for $\delta/\eta > 0$, the complete range of radius $\Gamma = \delta\sqrt{\mathcal{T}}$ satisfying the equilibrium condition is not accessible as the rod may be subjected to self-intersection.

II.3.2.2 Continuous contact

For rods contacting the cylindrical constraint, either inside or outside, the helix radius δ is no longer unknown and condition (II.3.15) ceases to be valid. The twisting moment is given by equation (II.3.12) and the helical equilibrium is maintained provided the loading parameter satisfies

$$m = \frac{\sin\theta\,(1+\cos\theta)\left(\cos\theta + \frac{\eta^2}{\delta^2}\Gamma^2\right)}{\Gamma\left(\cos\theta + \frac{\eta^2}{\delta^2}\sin^4\theta\right)}, \tag{II.3.17}$$

which simplifies to $m = \sin\theta\,(1+\cos\theta)/\Gamma$ for inextensible rods with $\Gamma = \delta\sqrt{\mathcal{T}}$. The constant magnitude ρ of the associated radial reaction force reads

$$\frac{\rho\,\delta}{\mathcal{T}} = m^2\frac{\Gamma^2 - \left(1 + \frac{\eta^2}{\delta^2}\Gamma^2\cos\theta\right)\sin^2\theta}{(1+\cos\theta)^2\left(\cos\theta + \frac{\eta^2}{\delta^2}\Gamma^2\right)}, \tag{II.3.18}$$

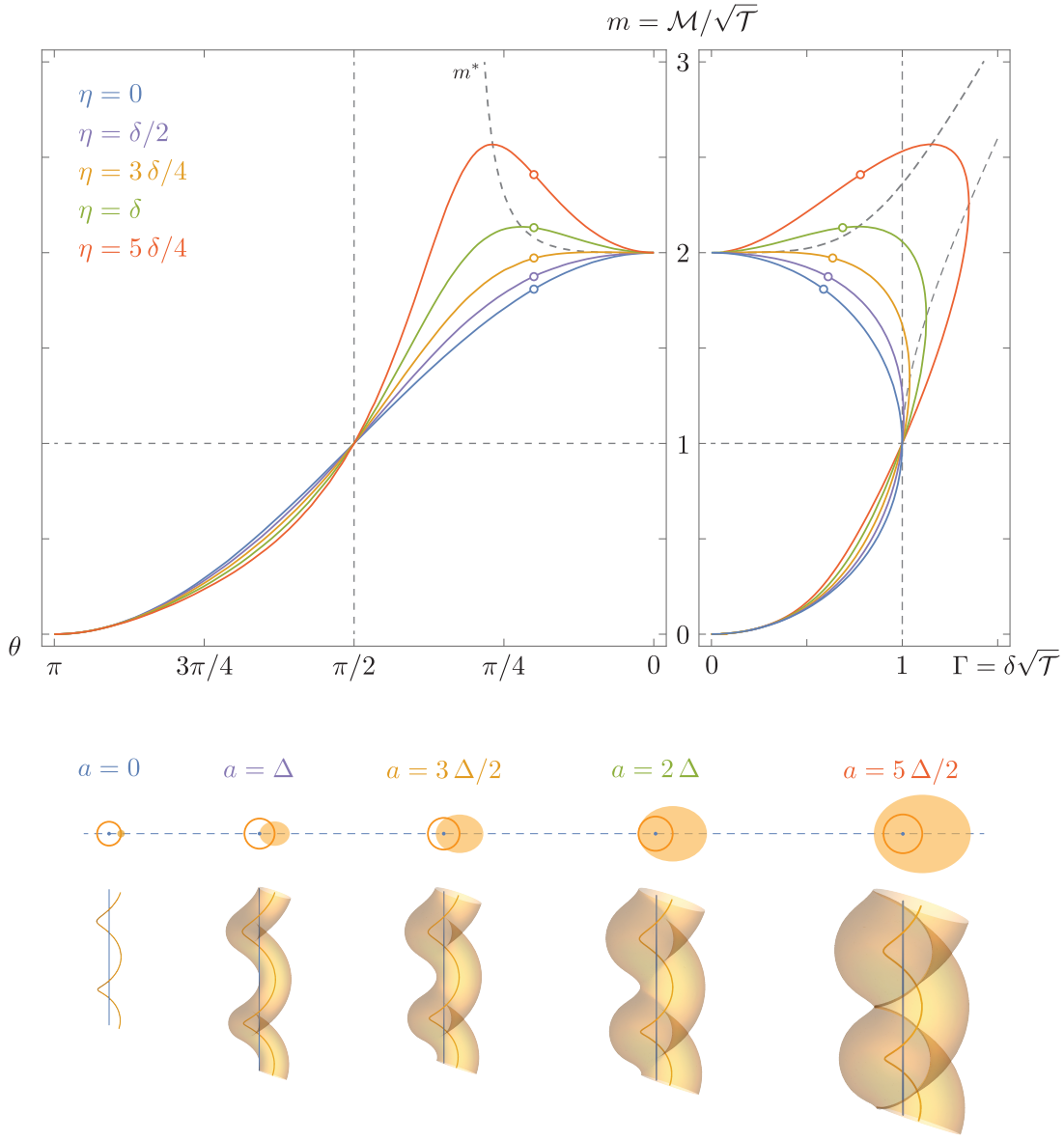

Figure II.3.1: Attributes of the free helix as functions of the loading parameter $m = \mathcal{M}/\sqrt{\mathcal{T}}$. The pitch angle θ and radius $\Gamma = \delta\sqrt{\mathcal{T}}$ are presented for various values of the ratio η/δ. Outset: deformed configurations associated with distinct values of the ratio $\delta/\eta = 2\,\Delta/a$ for $\theta = \pi/5$ and $\mathcal{T} = 1$; the corresponding sets of parameters $\{m, \theta, \Gamma\}$ are identified with circles on the universal curves.

with $\rho > 0$ corresponding to an outward-pointing radial reaction force. Whether this reaction is positive or negative depends on whether the constraint radius is larger or smaller than the

radius of the free helix for the same loading parameter m. The radius Γ and, subsequently, the loading parameter m corresponding to the free helix, *cf.* Equation (II.3.15), are recovered upon imposing $\rho = 0$.

II.3.3 Helical conduit

As a third example, the progressive buckling of an initially straight elastic rod constrained inside a helical conduit is investigated. Although axially unconstrained, *i.e.*, free to flow in/out of the conduit, the rod is assumed to be transversally clamped on the conduit axis at both extremities and subjected to an end torque $\mathcal{M}_3(1) = \mathcal{M}$ and axial force $\mathcal{F}_3(1) = \mathcal{T}$, see Figure II.3.2(a). Assuming the rod to be weightless and maintaining the end torque constant, the magnitude of the axial force is progressively increased until the rod contacts the constraint and a discrete contact subsequently emerges. The constraint considered in the present application is defined by its helical axis, with pitch angle $\Theta = \pi/4$ and radius $\Sigma = R/L = \left(\pi\sqrt{2}\right)^{-1}$, and constant radius $\epsilon = Q/L$ where the length $L = \pi R/\sin\Theta$ of the problem under consideration corresponds to a half helical turn. Two clearances, $\epsilon = 1/40$ and $1/20$, are investigated. Anticipating the discrete contact to appear at midspan $\xi = 1/2$ for symmetry reasons, the attached $\{\boldsymbol{D}_j\}$–basis is chosen to be the Bishop frame aligned with the Frenet-Serret apparatus at this point.

Although the present application shares multiple features with the problem of an elastica constrained inside a tube that has been investigated in Chen and Li (2011); Fang et al. (2013); Li and Chen (2014), it differs by the unprescribed nature of the rod length, *i.e.*, self-feeding. Indeed, while the distance between the extremities of a rod of finite length evolves as a result of the loading, this distance is kept constant in the present analysis and the rod length freely adapts to the loading.

In the following, the initial contact-free and the subsequent discrete contact phases of this constrained buckling is analyzed for $\eta = 1/20$ and $\nu = 1/3$. Details of the numerical implementation are presented in Section IV.1.1.1.

II.3.3.1 Free rod

The initial configuration is chosen to be the helical deformation characterized by a uniformly null eccentricity vector; this state is however not to be confused with the straight stress-free configuration $\mathscr{E}^0$ that is only observable in helical conduits with $\epsilon \geq \Sigma$. Following a procedure similar to the one presented in Section II.3.2 but considering solutions that are not homoclinic to the straight configuration, one may solve the governing equations (II.2.48–II.2.53) with the boundary conditions $\{\mathcal{F}_3(0) = \mathcal{T}, \mathcal{M}_3(0) = \mathcal{M}\}$. Hence, the axial end force $\mathcal{T} = \mathcal{T}_0$ required to maintain the rod on the constraint axis is obtained by imposing $\rho(\xi) = 0$, that is

$$\Sigma^2 \mathcal{T}_0 = \frac{(\Sigma\,\mathcal{M} - \sin\Theta\cos\Theta)\sin\Theta\cos\Theta}{1 + \frac{\eta^2}{\Sigma^2}\sin^2\Theta\cos^2\Theta}. \tag{II.3.19}$$

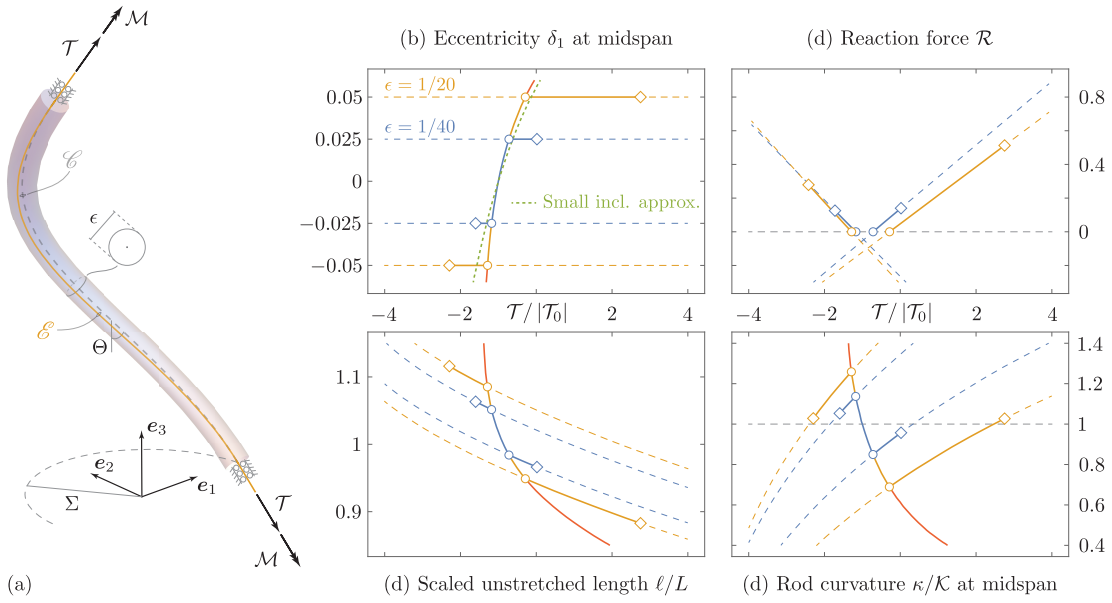

Figure II.3.2: Progressive buckling of an initially straight elastic rod constrained inside a helical conduit. The rod is subjected to an end torque $\mathcal{M} = -1$ and axial force $\mathcal{T}$. (a) Description of the problem under consideration. (b) Eccentricity δ_1 at midspan, (c) reaction force $\mathcal{R}$ at the discrete contact, (d) scaled unstretched length of the rod ℓ/L, and (e) rod curvature $\kappa/\mathcal{K}$ at midspan as functions of the end force $\mathcal{T}/|\mathcal{T}_0|$ with $\mathcal{T}_0 = -7.069$. Results obtained for $\epsilon = 1/40$ and $\epsilon = 1/20$ are plotted in blue and orange, respectively. Circles mark the appearance of the discrete contacts and squares identify the transition from discrete to continuous contact.

For values of the parameters associated with the problem under consideration and $\mathcal{M} = -1$, this relation yields $\mathcal{T}_0 = -7.069$.

Maintaining the torque $\mathcal{M}$ constant, the magnitude of the end force $\mathcal{T}$ is progressively increased causing the rod to gradually leave the constraint axis. Results obtained by means of the *exact* Eulerian formulation are compared to both the small inclination approximation (*cf.* section II.2.4) and the conventional Lagrangian formulation in Figure II.3.3 for $\mathcal{T}/|\mathcal{T}_0| = -1.25$. Although the Eulerian and Lagrangian formulations yield virtually identical results, the small inclination approximation underestimates the magnitude of the rod relative deflection; the overall profile of this solution being however coherent. This inaccuracy, due to the large curvature $\mathcal{K} = \pi \sin\Theta$ of the reference curve in spite of the smallness of ϵ, is expected to cause subsequent issues related to the non-penetration condition such as the detection of emerging contacts or the distinction between continuous and discrete contacts.

It is also seen that the magnitude of the eccentricity vector is maximal at midspan where $\delta_2 = 0$ such that the emergence of a contact between the rod and the constraint can readily be verified by ensuring that $|\delta_1| < \epsilon$ at $\xi = 1/2$. The evolution of the eccentricity δ_1 at midspan is pictured in Figure II.3.2(b) as a function of the end force $\mathcal{T}/|\mathcal{T}_0|$; both the results obtained by

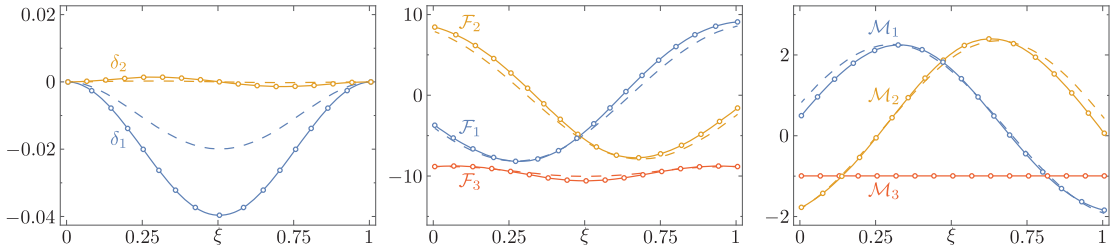

Figure II.3.3: Deflection, internal force and moment of a rod constrained inside a helical conduit as functions of the Eulerian curvilinear coordinate ξ. The projections $\delta_i(\xi)$ $(i = 1, 2)$ of the eccentricity vector and the components $\mathcal{F}_j(\xi)$ and $\mathcal{M}_j(\xi)$ $(j = 1, 2, 3)$ of the internal force and moment, respectively, are pictured as functions of ξ for $\mathcal{T}/|\mathcal{T}_0| = -1.25$ and $\mathcal{M} = -1$. The exact Eulerian formulation (——) is compared to both the small inclination approximation (– – –) and the Lagrangian formulation (∘ ∘ ∘).

means of the exact Eulerian formulation and the small inclination approximation are presented. As expected, the approximate formulation underestimates the end force at which the contact emerges. Additionally, the *self-feeding* ability characterizing the proposed method is emphasized in Figure II.3.2(d) as the unstretched length ℓ/L, which typically corresponds to the domain of the classical Lagrangian formulation, is seen to freely evolve as a result of the loading.

II.3.3.2 Discrete contact

As the eccentricity $\|\boldsymbol{\delta}\|$ reaches the clearance ϵ, a discrete contact emerges between the rod and the constraint giving rise to a reaction force $\boldsymbol{\mathcal{R}} = [\![\boldsymbol{\mathcal{F}} - \mathcal{F}_3\, \boldsymbol{d}_3]\!]$ aligned with the local normal to the constraint surface and balancing the discontinuity in the shear force. Here, double brackets denotes the increment of the quantity across a discontinuity, *e.g.* $[\![\boldsymbol{\mathcal{F}}]\!] = \lim_{\partial\xi} (\boldsymbol{\mathcal{F}}(\xi + \partial\xi) - \boldsymbol{\mathcal{F}}(\xi - \partial\xi))$. The magnitude of this reaction force being *a priori* unknown, the global problem is partitioned into two elementary boundary value problems, each corresponding to a rod segment free of contact. Although both the position and inclination of the rod are prescribed at the extremities of the global problem, only the magnitude of the eccentricity vector is known at the junction of the two elementary problems. Resorting to a shooting method Ascher et al. (1995), the missing boundary conditions are substituted with educated guesses and the rod integrity is restored by ensuring the continuity of the internal moment across the contact, *i.e.*, $[\![\boldsymbol{\mathcal{M}}]\!] = \mathbf{0}$. The magnitude $\mathcal{R} > 0$ of the radial reaction and the unstretched length ℓ/L are presented in Figure II.3.2(c) and II.3.2(d), respectively, as the end force varies. For consistency purposes with the preceding phase of the loading, these quantities are plotted in the scaling associated with the global problem. Points marking the appearance of the discrete contact are identified with circles.

Further increasing the magnitude of the end force may however lead to a violation of the unilateral contact condition and an additional restriction on the curvatures of both the rod and

the constraint surface at the contact point should be considered. This criterion, which also marks the transition form discrete to continuous contact, ensures that the curvature of the constraint surface is smaller than the curvature of the osculating circle to the space curve $\mathscr{C}$ at the contact point.

II.3.3.3 Continuous contact

As emphasized in the following Chapter, along a continuous contact, the rod curvature κ can be decomposed between its normal κ_n and geodesic κ_g components according to Pressley (2010)

$$\kappa\,\boldsymbol{n} = \kappa_n\,\boldsymbol{N} + \kappa_g\,\boldsymbol{N}\times\boldsymbol{d}_3, \tag{II.3.20}$$

where $\boldsymbol{N}$ is the inward pointing unit normal to the constraint surface. While $\boldsymbol{N} = -\boldsymbol{D}_1$ for the inner ($\delta_1 = \epsilon$) and $\boldsymbol{N} = \boldsymbol{D}_1$ for the outer ($\delta_1 = -\epsilon$) discrete contact, it can be shown that, due to the symmetry of the rod deformed configuration, the unit normal vector to $\mathscr{C}$ reads $\boldsymbol{n} = \boldsymbol{D}_1$ at these points irrespectively of the contacting side. Additionally, following Euler's theorem, the normal curvature reads

$$\kappa_n = \mathcal{K}_1\sin^2\theta + \mathcal{K}_2\cos^2\theta, \tag{II.3.21}$$

with the principal curvatures of the constraint surface given by $\mathcal{K}_1 = 1/\epsilon$ and $\mathcal{K}_2 = \mathcal{K}/\left(\epsilon\,\mathcal{K}\pm 1\right)$ for the outer (+) and inner (−) contacts, respectively. The principal vectors associated therewith coinciding with $\boldsymbol{D}_2$ and $\boldsymbol{D}_3$, the angle θ is defined as the inclination of the director $\boldsymbol{d}_3$ on the reference curve according to Equation (II.2.12). Therefore, projecting equation (II.3.20) with expression (II.3.21) for the normal curvature κ_n and the above mentioned definitions of the principle curvatures $\mathcal{K}_1$ and $\mathcal{K}_2$ on the unit normal vector $\boldsymbol{n} = \pm\boldsymbol{N}$, it can readily be shown that the contacts remain discrete provided the rod curvature satisfies the following inequalities

$$\kappa \leq \frac{\epsilon\,\mathcal{K} - \sin^2\theta}{\epsilon\left(\epsilon\,\mathcal{K} - 1\right)}, \qquad\qquad \kappa \geq \frac{\epsilon\,\mathcal{K} + \sin^2\theta}{\epsilon\left(\epsilon\,\mathcal{K} + 1\right)}, \tag{II.3.22}$$

at the inner and outer contacts, respectively. The rod curvature is depicted in Figure II.3.2(e) as the end force varies. Points marking the transition from discrete to continuous contact, *i.e.*, at which the inequalities are strictly satisfied, are identified with rhombuses.

At this stage of the loading, the method used to solve the discrete contact problem ceases to be valid and the global problem should be partitioned into three elementary boundary value problems. As the extent and geometry of the central problem, corresponding to the rod in continuous contact with the constraint surface, are *a priori* unknown a shooting method similar to the one previously introduced can be used. This forthcoming stage of the loading is analyzed in Section IV.2.

II.4 Summary

The Eulerian formulation of elastic rods proposed in this Chapter hinges on *(i)* describing the rod deformed configuration $\mathscr{E}$ by means of its relative deflection with respect to a reference curve $\mathscr{C}$, and *(ii)* expressing the kinematical as well as mechanical quantities pertaining to the rod in terms of the curvilinear coordinate associated with the reference curve. Both elementary configurations corresponding to segments of rod either in continuous contact with the constraint or free of contact have been investigated simultaneously as they essentially differ by the nature of the body force acting along the rod.

The restatement of the rod local equilibrium in terms of the Eulerian curvilinear coordinate, is particularly appropriate to treat free boundary problems associated with rods forced to go through two distinct fixed points in space. The isoperimetric constraints that would otherwise ensue from a conventional Lagrangian formulation indeed vanish and the resolution reduces to that of a classical boundary value problem, of mixed order though. Additionally, the *a posteriori* assessment of the unilateral contact condition ensuring that, depending on the context, the rod remains either in continuous contact or free of contact along an elementary problem has been trivialized. The detection of emerging contacts throughout contact-free problems indeed reduces to the comparison of the eccentricity magnitude with the constraint radius. Alternatively, along continuous contacts, the rod is compelled to lay on the constraining surface by straightforwardly imposing the magnitude of this vector.

The proposed formulation reaches its limits with the single-valuedness of the mapping $S(s)$, from Lagrangian to Eulerian coordinates, and its reciprocal $s(S)$, from Eulerian to Lagrangian coordinates. Geometrically, these knotty situations emerge either as a section along the reference curve is crossed multiple times or if the eccentricity vectors at distinct Eulerian coordinates intersect. The former situation, which usually arises in conjunction with deformed configurations characterized by curling, writhing or other solutions involving self-contact such as folding, can be identified by the orthogonality of the director $\boldsymbol{d}_3$ and the tangent vector to the reference curve $\boldsymbol{D}_3$, *i.e.*, situations where $g_3(\xi)$ vanishes at least once along the domain. Alternatively, the singular configuration associated with the latter situation occurs when the eccentricity vector aligns with the normal vector to the reference curve $\boldsymbol{D}_3'$ and its norm is at least equal to the reference curve curvature $\mathcal{K}$, that is when $\boldsymbol{\delta} \cdot \boldsymbol{D}_3' = \delta_1 \mathcal{U}_2 - \delta_2 \mathcal{U}_1 \geq 1$. Interestingly, these two problematic situations are both avoided by ensuring $g_3(\xi)$ to remain strictly positive throughout the domain. Therefore, situations in which the scalar product $\boldsymbol{d}_3 \cdot \boldsymbol{D}_3$ changes sign cannot be captured by the proposed method.

Remark regarding the nonuniqueness of the solution

As the length of the rod along the boundary value problem under consideration is not prescribed, more than one solution may correspond to one set of boundary conditions. In the context of heavy (as opposed to weightless) rods, distinct rod lengths indeed correspond to

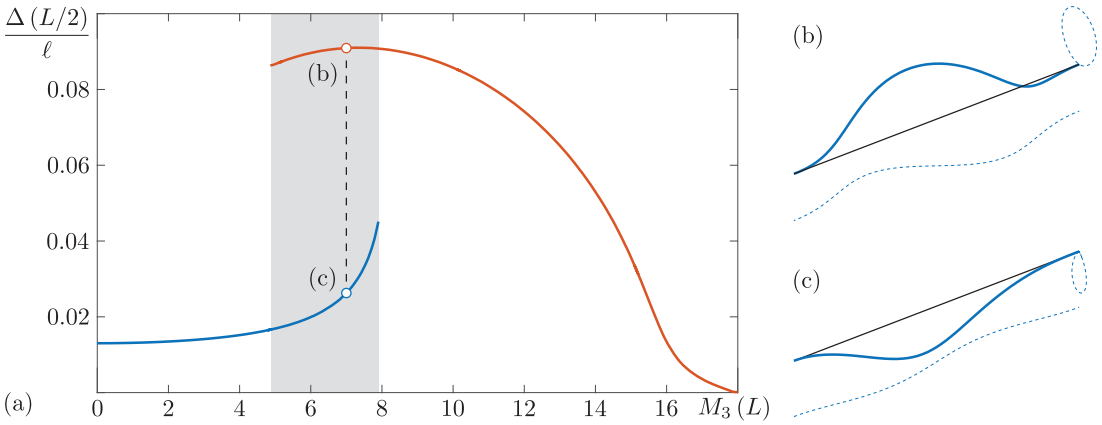

Figure II.4.1: Nonuniqueness of the solution of the elementary problem. (a) Response diagram of the clamped-sliding sleeve rod under varying end twisting $M_3(L)$, zero end trust $F_3(L) = 0$ and constant specific weight ($\boldsymbol{f} = w\,\boldsymbol{e}_3$ with $w = 5\,B/L^3$). The greyed zone identifies the region where noncongruent equilibrium have been observed (numerically.) Although both solutions (b) and (c) are associated with identical boundary conditions ($M_3(L) = 7\,B/L$) and external loading, they corresponds to noncongruent equilibriums of the rod. The dashed lines correspond to the projections of rod centerline on horizontal and vertical planes. Note that the rod deflection in solution (b) is amplified by a factor 5.

different loadings such that noncongruent equilibriums may be obtained for identical boundary conditions. Figure II.4.1(a) depicts the response diagram of an elastic rod subjected to clamped-sliding sleeve boundary conditions and varying end twist $M_3(L)$. The greyed zone in the Figure identifies the region where noncongruent equilibriums have been observed (numerically.) For instance, both solutions (b) and (c) were obtained by imposing identical end conditions ($M_3(L) = 7\,B/L, F_3(L) = 0$). The identification of the complete loading path, expected to join the two branches presented in Figure II.4.1(a), would require the numerical continuation of the solution, which is beyond the scope of this work. This aspect of the problem has been investigated in more details in an conference article (Huynen et al., 2013). Finally, note that this property is not specific to the Eulerian formulation but rather results from the support conditions and the *self-feeding* feature associated with the elementary problem.

"[...] for the description of right lines and circles, upon which geometry is founded, belongs to mechanics. Geometry does not teach us to draw these lines, but requires them to be drawn [...]"

Sir Isaac Newton (1687)

Chapter III

Surface Constrained Elastic Rods

In the previous Chapter, both the continuous contact and the free of contact configurations have been investigated simultaneously under the assumption that they essentially differ by the nature of the body force acting on the rod. However, as the *a priori* unknown reaction pressure compels the rod to lay on the constraint surface along a continuous contact, the rod inherently shares fundamental geometric features with this surface and the determination of the rod spatial configuration may therefore be adapted accordingly. In this Chapter, the general Lagrangian formulation for elastic rods is first particularized to surface bound rods by *(i)* specifying the configuration of the rod centerline in terms of its coordinates in the parameter space associated with the constraint surface parameterization, and *(ii)* characterizing the configuration of its material frame through its rotation with respect to the surface normal. Although the rod centerline is enforced to lay on the constraint, no assumption is made on its shape. In the process, the rod flexural and torsional strains are re-expressed in terms of intrinsic and extrinsic properties of the constraining surface along the rod centerline, emphasizing the influence of the constraint geometry on the rod deformed configuration. Finally, an expression for the reaction pressure is derived. The Lagrangian description of surface bound rods is then adapted to rods in continuous contact with normal ringed surfaces and an Eulerian formulation analogue to the one obtained in Section II.2 is derived. By degenerating this approach to a single point, the criterion governing the transition between discrete and continuous contacts is finally derived.

III.1 Lagrangian formulation of surface bound elastic rods

Consider an elastic rod lying on an oriented surface $\mathscr{S}$ parameterized by $\boldsymbol{\mathcal{S}}(u, v)$ in the Euclidean space $\mathbb{E}^3$ and denote, once again, by $\boldsymbol{r}(s) = x_j\, \boldsymbol{e}_j$ the parameterization of the rod centerline

$\mathscr{E}$ in its deformed configuration. Within the Cosserat theory, the elastic rod is modeled as a space curve endowed with mechanical properties that are suitably averaged over its cross section. The rod is consequently reduced to a one-dimensional elastic body and its transverse dimension is ignored compared to its length. Along a continuous contact with the constraint surface, the rod centerline is therefore confined to the subset $\mathscr{S}$ of $\mathbb{E}^3$ and the space curve $\mathscr{E}$ may be re-parameterized as

$$\boldsymbol{r}(s) = \boldsymbol{\mathcal{S}}(u(s), v(s)), \tag{III.1.1}$$

where the coordinates $(u(s), v(s))$ of the rod cross section s in the parameter space associated with the constraint surface are smooth functions of s in accordance to the assumed C^4–continuity of both the rod and the constraint surface. Therefore, by the chain rule and the definition (II.1.3) of the stretch vector $\boldsymbol{v} = \mathrm{d}\boldsymbol{r}/\mathrm{d}s$, the stretch of the rod reads

$$\alpha(s) = \|\boldsymbol{\mathcal{S}}_u u' + \boldsymbol{\mathcal{S}}_v v'\|, \tag{III.1.2}$$

with the first partial derivatives $\boldsymbol{\mathcal{S}}_u(u,v) = \partial\boldsymbol{\mathcal{S}}/\partial u$ and $\boldsymbol{\mathcal{S}}_v(u,v) = \partial\boldsymbol{\mathcal{S}}/\partial v$, and where primes indicate derivatives with respect to the Lagrangian coordinate s. Denoting by

$$E(u,v) = \boldsymbol{\mathcal{S}}_u \cdot \boldsymbol{\mathcal{S}}_u, \qquad F(u,v) = \boldsymbol{\mathcal{S}}_u \cdot \boldsymbol{\mathcal{S}}_v, \qquad G(u,v) = \boldsymbol{\mathcal{S}}_v \cdot \boldsymbol{\mathcal{S}}_v, \tag{III.1.3}$$

the coefficients of the first fundamental form associated with the parameterization $\boldsymbol{\mathcal{S}}(u,v)$ of the constraint surface (Pressley, 2010, ch. 6), the former expression may be rewritten as

$$\alpha(s) = \sqrt{E\,u'^2 + 2\,F\,u'\,v' + G\,v'^2}, \tag{III.1.4}$$

which emphasizes that the drift existing between the two curvilinear coordinates is the restriction to the surface curve $\mathscr{E}$ of the square root of the first fundamental form $I = E\,\mathrm{d}u^2 + 2\,F\,\mathrm{d}u\,\mathrm{d}v + G\,\mathrm{d}v^2$ of the surface, *i.e.*, the arc-length of a line element of $\mathscr{E}$ on the surface $\mathscr{S}$. The first fundamental form being positively definite, expression (III.1.4) is always well-defined.

III.1.1 Directors and geometry of deformation

In view of the assumed regularity of the constraint surface, the vectors $\boldsymbol{\mathcal{S}}_u(u,v)$ and $\boldsymbol{\mathcal{S}}_v(u,v)$ are linearly independent and the tangent space to $\mathscr{S}$ is two-dimensional. The director $\boldsymbol{d}_3$, which is the unit tangent vector to the rod centerline $\mathscr{E}$ as a result of the unshearablility assumption, can therefore be expressed as a linear combination of these two vectors. Differentiating equation (III.1.1) with respect to s, this unit vector reads

$$\boldsymbol{d}_3(s) = \alpha^{-1}(\boldsymbol{\mathcal{S}}_u u' + \boldsymbol{\mathcal{S}}_v v'). \tag{III.1.5}$$

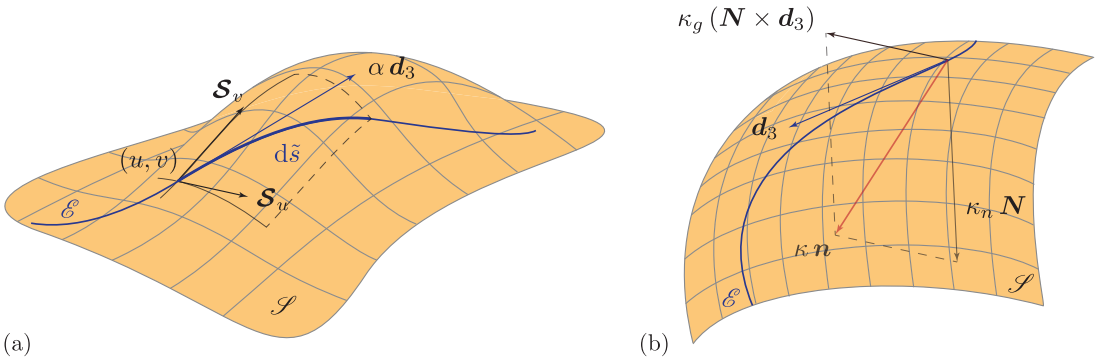

Figure III.1.1: Continuous contact of elastic rods and surface bound curves. (a) Description of the director $\boldsymbol{d}_3$ in the skew coordinates system $\{\boldsymbol{\mathcal{S}}_u, \boldsymbol{\mathcal{S}}_v\}$ associated with the surface parameterization $\boldsymbol{\mathcal{S}}\,(u, v)$. (b) Geometric interpretation of the geodesic curvature κ_g and normal curvature κ_n of surface bound curves, decomposition of the intrinsic curvature κ between its tangential and normal components.

This decomposition in the skew coordinate system $\{\boldsymbol{\mathcal{S}}_u, \boldsymbol{\mathcal{S}}_v\}$ is depicted in Figure III.1.1(a).

Although the configuration of the rod centerline is uniquely defined by the coordinates $(u\,(s)\,, v\,(s))$, the rod spatial configuration is not fully characterized until the angle between either director $\boldsymbol{d}_1$ or $\boldsymbol{d}_2$ and a specified direction is known. Upon definition of the *unit normal* to the constraint surface

$$\boldsymbol{N}\,(u, v) = \frac{\boldsymbol{\mathcal{S}}_u \times \boldsymbol{\mathcal{S}}_v}{\|\boldsymbol{\mathcal{S}}_u \times \boldsymbol{\mathcal{S}}_v\|}, \tag{III.1.6}$$

the triplet $\{\boldsymbol{d}_3, \boldsymbol{N} \times \boldsymbol{d}_3, \boldsymbol{N}\}$ constitutes a right-handed orthonormal basis in which the rotation of the rod cross section about its axis may be specified as

$$\boldsymbol{d}_1\,(s) = \cos\psi\, \boldsymbol{N} \times \boldsymbol{d}_3 + \sin\psi\, \boldsymbol{N}, \tag{III.1.7}$$

$$\boldsymbol{d}_2\,(s) = -\sin\psi\, \boldsymbol{N} \times \boldsymbol{d}_3 + \cos\psi\, \boldsymbol{N}. \tag{III.1.8}$$

The unit vector $\boldsymbol{N} \times \boldsymbol{d}_3$ is sometimes referred to as the *geodesic normal vector* for reasons that will become clear in the following. The triplet of vectors $\{\boldsymbol{d}_3, \boldsymbol{N} \times \boldsymbol{d}_3, \boldsymbol{N}\}$ is the *Darboux frame* (Gray, 1996, ch. 22) of $\mathscr{C}$ with respect to $\mathscr{S}$. Being everywhere well-defined, it presents a major advantage over the Frenet–Serret trihedron (Gray, 1996, ch. 8), which may lead to existence and continuity issues along curves with vanishing curvature.

The rod configuration along a continuous contact with a constraint surface $\mathscr{S}$ parameterized by $\boldsymbol{\mathcal{S}}\,(u, v)$ therefore reduces to the knowledge of three functions

$$[s_a, s_b] \ni s \mapsto u\,(s)\,, v\,(s)\,, \psi\,(s) \in \mathbb{R}. \tag{III.1.9}$$

This description of surface bound rods, involving only three degrees of freedom, leads to a curve-angle representation (Bergou et al., 2008; Langer and Singer, 1996; Bergou et al., 2010) in which, as discussed, the rod's centerline is explicitly defined by the coordinate $(u(s), v(s))$ in the parameter space associated with the constraint surface while the rotation of the material frame is characterized by the angle $\psi(s)$. The differential equations governing the behavior of these functions of s are obtained in the following. This formulation is however not *minimal* as the description of the rod's centerline may be reduced upon orthogonal re–parameterization of the surface, that is such that the coefficient F defined in equation (III.1.3) uniformly vanishes. In this context, the angle $\theta(s) \in [0, 2\pi]$ between the u–parameter line and the unit tangent $\boldsymbol{d}_3$ may indeed be introduced leading to the relations $(u', v') = \alpha \left(\sqrt{E}\cos\theta, \sqrt{G}\sin\theta\right)$; the resulting minimal formulation therefore involving two angles $\theta(s)$ and $\psi(s)$, only. The reason why this formulation is not carried in the following is explained in Section III.1.1.2.

III.1.1.1 Kinematics

The directors being described in the Darboux frame $\{\boldsymbol{d}_3, \boldsymbol{N} \times \boldsymbol{d}_3, \boldsymbol{N}\}$ by means of equations (III.1.7–III.1.8), their kinematics along the surface bound curve $\mathscr{E}$ may be decomposed into the kinematics of the Darboux frame and their rotation $\psi(s)$ with respect to this basis. Analogously to the Frenet–Serret formulas, see equations (II.1.5), are the Darboux formulas (Gray, 1996, ch. 22)

$$\alpha^{-1}\frac{\mathrm{d}\boldsymbol{d}_3}{\mathrm{d}s} = \kappa_g\, \boldsymbol{N} \times \boldsymbol{d}_3 + \kappa_n\, \boldsymbol{N}, \tag{III.1.10}$$

$$\alpha^{-1}\frac{\mathrm{d}}{\mathrm{d}s}(\boldsymbol{N} \times \boldsymbol{d}_3) = -\kappa_g\, \boldsymbol{d}_3 + \tau_g\, \boldsymbol{N}, \tag{III.1.11}$$

$$\alpha^{-1}\frac{\mathrm{d}\boldsymbol{N}}{\mathrm{d}s} = -\kappa_n\, \boldsymbol{d}_3 - \tau_g\, \boldsymbol{N} \times \boldsymbol{d}_3, \tag{III.1.12}$$

where the *geodesic curvature* $\kappa_g(u, v)$, whose definition solely involves the first fundamental form of the parameterization $\boldsymbol{\mathcal{S}}(u, v)$, is an intrinsic property of $\mathscr{S}$, while the *normal curvature* $\kappa_n(u, v)$ and the *geodesic torsion* $\tau_g(u, v)$ are extrinsic properties of the constraint surface. According to the Frenet–Serret formulas (Gray, 1996, ch. 8), the righthand side of equation (III.1.10) reads $\kappa\, \boldsymbol{n}$ where $\boldsymbol{n}$ is the unit normal to the space curve $\mathscr{E}$. This expression therefore emphasizes that $\kappa_n\, \boldsymbol{N}$ and $\kappa_g\, \boldsymbol{N} \times \boldsymbol{d}_3$ are the orthogonal projections of $\kappa\, \boldsymbol{n}$ onto the surface normal and the tangent space to $\boldsymbol{\mathcal{S}}(u, v)$ and, consequently, establishes a relationship between the rod intrinsic curvature $\kappa = \sqrt{\kappa_n^2 + \kappa_g^2}$ and its normal and tangential components κ_n and κ_g, respectively. This decomposition is depicted in Figure III.1.1(b). The significance of these geometric properties, which are attached to the space curve $\mathscr{E}$ confined to $\mathscr{S}$ and are invariant under a re-parameterization of $\mathscr{E}$, is explored below.

III.1.1.2 Geometric invariants

Intrinsic properties of a surface (e.g. length, angle, area) can be measured within the surface itself and, therefore, depend on the metric of the surface, solely. The geodesic curvature, being the rate of change of the angle that the tangent to the curve makes with a parallel direction along the curve (Do Carmo, 1976, p 252), is independent of how the surface sits in the ambient space. It is expressed in terms of the coefficients of the first fundamental form (III.1.3). It generalizes the notion of signed curvature of planar curves (Gray, 1996, p 516) to arbitrary surfaces by measuring how the curve $\mathscr{C}$ bends with respect to geodesics[1] on the surface. It is expressed as

$$\kappa_g(s) = \sqrt{\frac{E\,G - F^2}{\left(E\,u'^2 + 2\,F\,u'\,v' + G\,v'^2\right)^3}}\left[\Gamma^2_{11}u'^3 - \Gamma^1_{22}v'^3 + \left(2\,\Gamma^2_{12} - \Gamma^1_{11}\right)u'^2v' - \left(2\,\Gamma^1_{12} - \Gamma^2_{22}\right)u'v'^2 + u'\,v'' - u''\,v'\right], \tag{III.1.13}$$

where the *Christoffel symbols* (Pressley, 2010, p 172) read

$$\Gamma^1_{11} = \frac{G\,E_u - 2\,F\,F_u + F\,E_v}{2\left(E\,G - F^2\right)}, \qquad \Gamma^2_{11} = \frac{2\,E\,F_u - E\,E_v - F\,E_u}{2\left(E\,G - F^2\right)}, \tag{III.1.14}$$

$$\Gamma^1_{12} = \frac{G\,E_v - F\,G_u}{2\left(E\,G - F^2\right)}, \qquad \Gamma^2_{12} = \frac{E\,G_u - F\,E_v}{2\left(E\,G - F^2\right)}, \tag{III.1.15}$$

$$\Gamma^1_{22} = \frac{2\,G\,F_v - G\,G_u - F\,G_v}{2\left(E\,G - F^2\right)}, \qquad \Gamma^2_{22} = \frac{E\,G_v - 2\,F\,F_v + F\,G_u}{2\left(E\,G - F^2\right)}. \tag{III.1.16}$$

see Appendix A.2 for details of the derivation.

On the other hand, extrinsic properties of $\mathscr{S}$, such as the normal curvature and the geodesic torsion, depend on the embedding of the constraint surface in the ambient space $\mathbb{E}^3$. As the rod may only deform freely in the tangent plane to the constraining surface, these properties are anticipated to play a major role in the way the reaction pressure is transmitted to the rod. Hence, denoting by

$$e(u,v) = \boldsymbol{\mathcal{S}}_{uu}\cdot\boldsymbol{N}, \qquad f(u,v) = \boldsymbol{\mathcal{S}}_{uv}\cdot\boldsymbol{N}, \qquad g(u,v) = \boldsymbol{\mathcal{S}}_{vv}\cdot\boldsymbol{N}, \tag{III.1.17}$$

the coefficients of the second fundamental form $II = e\,\mathrm{d}u^2 + 2\,f\,\mathrm{d}u\,\mathrm{d}v + g\,\mathrm{d}v^2$ (Pressley, 2010, ch. 7), the normal curvature reads

$$\kappa_n(s) = \frac{e\,u'^2 + 2\,f\,u'\,v' + g\,v'^2}{E\,u'^2 + 2\,F\,u'\,v' + G\,v'^2}. \tag{III.1.18}$$

which is the ratio of the fundamental forms along $\mathscr{E}$. It measures how the constraint surface

[1] Geodesics extend the notion of straight lines to curved space and are interpreted as the shortest curve among all piecewise-differentiable curves on $\mathscr{S}$ connecting two points (Gray, 1996, ch. 26). Mathematically, a geodesic is a curve which is everywhere locally a distance minimizer. These surface curves are identified as lines of zero geodesic curvature such that, along geodesics, the rod bending energy solely arises from the normal curvature.

bends in the tangential direction $\boldsymbol{d}_3$ and is positive if $\mathscr{S}$ bends toward its unit normal $\boldsymbol{N}$. The geodesic torsion is a further measure of the local geometry of the surface along the rod centerline complementary to the normal curvature, its expression

$$\tau_g(s) = \frac{(f\,E - e\,F)\,u'^2 + (g\,F - f\,G)\,v'^2 + (g\,E - e\,G)\,u'\,v'}{(E\,u'^2 + 2\,F\,u'\,v' + G\,v'^2)\,\sqrt{E\,G - F^2}}, \tag{III.1.19}$$

similarly involves the coefficients of both first and second fundamental forms; its derivation is presented in Appendix A.2. It equals the torsion of the geodesic passing through the point (u, v) in the direction $\boldsymbol{d}_3$ and, therefore, introduces a geometrical notion of twist. It may also be interpreted as a measure of departure of the rod centerline from alignment with a principal curve, that is a direction along which the normal curvature is maximum or minimum.

As any given curvature and torsion functions determine exactly one space curve (up to rigid body motion), the geodesic and normal curvatures with the geodesic torsion suffice to fully characterize the spatial configuration of the rod centerline. This description of the space curve $\mathscr{E}$ incorporates redundancy, however, and the three geometric invariants $(\kappa_g, \kappa_n, \tau_g)$ are not independent since they are functions of only two parametric coordinates, namely $(u(s), v(s))$. Consequently, only two relations involving the geometric invariants are required to express the equilibrium of the rod centerline.

It has already been mentioned that, upon orthogonal re–parameterization of $\boldsymbol{\mathcal{S}}(u, v)$, the rod's centerline may alternatively be described by means of its local inclination $\theta(s)$ with respect to the u–parameter line, see Figure III.1.2. If this re–parameterization was further chosen such that the parameter lines are aligned with the surface's principal directions of curvature, the geometric invariants could be expressed as (Gray, 1996, p 372, p 520, p 587)

$$\kappa_g(s) = \frac{\theta'}{\alpha} + \kappa_u \cos\theta + \kappa_v \sin\theta, \tag{III.1.20}$$

$$\kappa_n(s) = \kappa_1 \cos^2\theta + \kappa_2 \sin^2\theta, \tag{III.1.21}$$

$$\tau_g(s) = (\kappa_2 - \kappa_1)\sin\theta\,\cos\theta, \tag{III.1.22}$$

where κ_u and κ_v are the geodesic curvatures of the parameter lines, κ_1 and κ_2 are the principal curvatures of the surface. As these intrinsic and extrinsic properties of $\mathscr{S}$ explicitly depend on the position of the rod centerline on the surface, *viz.* the parametric coordinates $(u(s), v(s))$, their evaluation along the rod centerline requires the integration of the relations $(\dot{u}, \dot{v}) = \alpha\left(\sqrt{G}\cos\theta, \sqrt{E}\sin\theta\right)/\sqrt{E\,G}$. This entanglement of the rod local inclination $\theta(s)$ and its coordinates $(u(s), v(s))$ is a further source of complexity that justifies the choice made here to favor a formulation in which the rod centerline is explicitly represented.

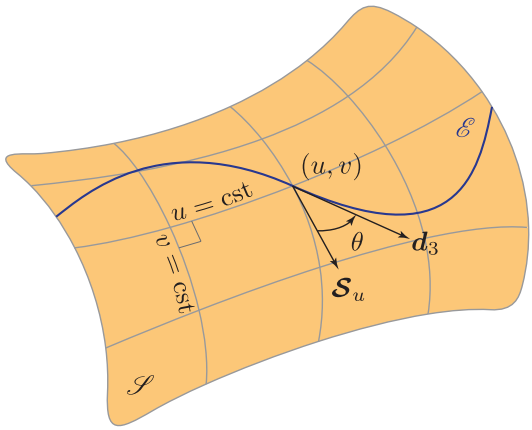

Figure III.1.2: Local inclination θ of a surface curve $\mathscr{E}$ in an orthogonal parameterization of $\mathscr{S}$. The local inclination of $\mathscr{E}$ at any of its point $(u(s), v(s))$ is the acute angle $\theta(s)$ measured from the u–parameter line through $(u(s), v(s))$ along which $u(s)$ increases.

III.1.1.3 Strain variables

The orientation of the directors with respect to the Darboux frame being entirely described by the rotation angle $\psi(s)$ about $\boldsymbol{d}_3$, the twist vector may be expressed as $\boldsymbol{u}(s) = \alpha \boldsymbol{h} + \psi' \boldsymbol{d}_3$ with the Darboux vector $\boldsymbol{h}(s) = \kappa_g \boldsymbol{N} - \kappa_n \boldsymbol{N} \times \boldsymbol{d}_3 + \tau_g \boldsymbol{d}_3$ characterizing the kinematics of the triplet $\{\boldsymbol{d}_3, \boldsymbol{N} \times \boldsymbol{d}_3, \boldsymbol{N}\}$ along the surface curve $\mathscr{E}$. Differentiating both sides of equations (III.1.7–III.1.8) and exploiting the kinematics equations (II.1.9) and (III.1.10–III.1.12), the strain variables indeed read

$$u_1(s) = \alpha \kappa_g \sin\psi - \alpha \kappa_n \cos\psi, \tag{III.1.23}$$

$$u_2(s) = \alpha \kappa_g \cos\psi + \alpha \kappa_n \sin\psi, \tag{III.1.24}$$

$$u_3(s) = \alpha \tau_g + \psi', \tag{III.1.25}$$

where the geometric invariants κ_g, κ_n and τ_g maintain identical values regardless of coordinate transformation, that is whether the surface curve $\mathscr{E}$ is parameterized by the coordinate s associated to the rod unstressed configuration, its arc-length parameter $\bar{s}$ or any other curvilinear coordinate.

Under the isotropy assumption, the rod bending stiffness about the directors $\boldsymbol{d}_1$ and $\boldsymbol{d}_2$ are equal and the constitutive laws (II.1.14–II.1.15) that relate the stretch and strain variables to the components of the internal force $\boldsymbol{F}(s) = F_k \boldsymbol{d}_k$ and moment $\boldsymbol{M}(s) = M_k \boldsymbol{d}_k$ may be expressed

in the Darboux frame $\{\boldsymbol{d}_3, \boldsymbol{N} \times \boldsymbol{d}_3, \boldsymbol{N}\}$ as

$$\boldsymbol{F}(s) = F_g\, \boldsymbol{N} \times \boldsymbol{d}_3 + F_n\, \boldsymbol{N} + A\,(\alpha - 1)\, \boldsymbol{d}_3, \tag{III.1.26}$$

$$\boldsymbol{M}(s) = \alpha\, B\,(\kappa_g\, \boldsymbol{N} - \kappa_n\, \boldsymbol{N} \times \boldsymbol{d}_3) + C\left(\alpha\, \tau_g + \dot{\psi}\right) \boldsymbol{d}_3, \tag{III.1.27}$$

where, again, A, B and C denote the axial, bending and torsional stiffnesses, respectively.

III.1.2 Force and moment balance

Along a continuous contact, the constraint surface $\mathscr{S}$ exerts on the elastic rod an *a priori* unknown normal reaction pressure $p(s)$ that enters the equilibrium equations through the body force $\boldsymbol{f}(s) = f_g\, \boldsymbol{N} \times \boldsymbol{d}_3 + (f_n + p)\, \boldsymbol{N} + f_3\, \boldsymbol{d}_3$ with (f_g, f_n, f_3) the projections of the known body force (e.g. its weight) per unit arc-length in the Darboux frame. Although in effect acting on the surface of the rod and not at its centerline, the assumption that the rod radius is much smaller than its length implicitly leads to ignore the otherwise resulting body couple per unit arc-length. Note that potential distributed couples arising from alternative sources (e.g., magnetic field) may however enter the rod governing equations through the body couple per unit reference length $\boldsymbol{m}(s) = m_g\, \boldsymbol{N} \times \boldsymbol{d}_3 + m_n\, \boldsymbol{N} + m_3\, \boldsymbol{d}_3$. The projection of the conservation of linear and angular momenta (II.1.12–II.1.13) in the Darboux frame, while expressing the dependance of the internal force and moment in the strain variables through the substitution of the constitutive relations (III.1.26–III.1.27), leads to

$$F_g' + A\,\alpha\,\kappa_g\,(\alpha - 1) - \alpha\,\tau_g\,F_n + f_g = 0, \tag{III.1.28}$$

$$F_n' + A\,\alpha\,\kappa_n\,(\alpha - 1) + \alpha\,\tau_g F_g + f_n + p = 0, \tag{III.1.29}$$

$$A\,\alpha' - \alpha\,(\kappa_g\,F_g + \kappa_n\,F_n) + f_3 = 0, \tag{III.1.30}$$

$$B\,(\alpha'\,\kappa_n + \alpha\,\kappa_n') + B\,\alpha^2\,\kappa_g\,\tau_g - C\,\alpha\,\kappa_g\,(\alpha\,\tau_g + \psi') + \alpha\,F_n - m_g = 0, \tag{III.1.31}$$

$$B\left(\alpha'\,\kappa_g + \alpha\,\kappa_g'\right) - B\,\alpha^2\,\kappa_n\,\tau_g + C\,\alpha\,\kappa_n\,(\alpha\,\tau_g + \psi') + \alpha\,F_g + m_n = 0, \tag{III.1.32}$$

$$C\left(\psi'' + \alpha'\,\tau_g + \alpha\,\tau_g'\right) + m_3 = 0. \tag{III.1.33}$$

After elimination of the shear components of the internal force and introduction of the definitions (III.1.4,III.1.13,III.1.18,III.1.19) for the stretch and geometric invariants, this coupled system of equations may be reduced to a set of three nonlinear differential equations: one fourth order, (III.1.28), and one third order, (III.1.30), in the parametric coordinates $(u(s), v(s))$ as well as one second order, (III.1.33), in the rotation angle $\psi(s)$; the remaining equation, (III.1.29), providing an expression for the reaction pressure $p(s)$. Although straightforwardly obtained, the resulting mixed order system of ODEs is cumbersome and will not be presented here.

III.1.3 Dimensionless formulation for weightless elastic rods

Consider a weightless elastic rod laying on a smooth surface and denote by $\ell^\star$ a characteristic length of the problem. The arc-length parameter and the geometric invariants therefore scale as $\chi = (s - s_a)/\ell^\star$ and

$$\varkappa_g(\chi) = \kappa_g(s(\chi))\,\ell^\star, \qquad \varkappa_n(\chi) = \kappa_n(s(\chi))\,\ell^\star, \qquad \varkappa_t(\chi) = \tau_g(s(\chi))\,\ell^\star, \tag{III.1.34}$$

respectively. Additionally introducing the characteristic force $F^\star = B/\ell^{\star 2}$ leads to the definition of the scaled internal force $\boldsymbol{\mathcal{F}}(\xi) = \boldsymbol{F}(s(\chi))/F^\star$ and moment $\boldsymbol{\mathcal{M}}(\chi) = \boldsymbol{M}(s(\chi))/\ell^\star F^\star$. Being naturally dimensionless, the stretch and the rotation angle are redefined as $\alpha(\chi) \coloneqq \alpha(s(\chi))$ and $\psi(\chi) \coloneqq \psi(s(\chi))$.

In the absence of body couple, the bending and twisting behaviors of an isotropic rod with a circular cross section uncouple. The projection of the moment balance (II.1.13) on the unit tangent $\boldsymbol{d}_3$ therefore reveals that the twisting moment $\mathcal{M}_3$ is uniform along its length. Accounting for the constitutive relation (III.1.27), it reads

$$(1+\nu)\,\mathcal{M}_3 = \alpha\,\varkappa_t + \psi', \tag{III.1.35}$$

with Poisson ratio $\nu = B/C - 1$ and where a prime now denotes differentiation with respect to the dimensionless coordinate χ. This relation reveals the partition of the twisting moment, $\mathcal{M}_3$, into the internal twist, ψ', and a measure of the kinematic torsion of the rod's centerline, $\alpha\,\varkappa_t$. It is analogous to the usual partition of the twist of an elastica into its internal twist and the torsion of its centerline (van der Heijden and Thompson, 2000). It also expresses that, along a twist free elastic rod, the pair of directors $(\boldsymbol{d}_1, \boldsymbol{d}_2)$ rotates about the unit tangent $\boldsymbol{d}_3$ with an *angular velocity* equal and opposite to $\alpha\,\varkappa_t$.

Similarly, plugging the constitutive relation (III.1.27) in the moment balance (II.1.13) and projecting the resulting equation on the geodesic $\boldsymbol{N} \times \boldsymbol{d}_3$ and normal $\boldsymbol{N}$ directions leads to equations (III.1.31–III.1.32) or

$$\alpha\,\mathcal{F}_g = -(\alpha\,\varkappa_g)' + \alpha\,\varkappa_n(\alpha\,\varkappa_t - \mathcal{M}_3), \tag{III.1.36}$$

$$\alpha\,\mathcal{F}_n = -(\alpha\,\varkappa_n)' - \alpha\,\varkappa_g(\alpha\,\varkappa_t - \mathcal{M}_3), \tag{III.1.37}$$

for the geodesic and normal components of the internal force, respectively. Substitution of these expressions in the force balance (II.1.12) and projection along the Darboux frame $\{\boldsymbol{d}_3, \boldsymbol{N} \times \boldsymbol{d}_3, \boldsymbol{N}\}$ provides the necessary governing equations relating the geometric invariants $(\varkappa_g, \varkappa_n, \varkappa_t)$ along the rod centerline as well as an expression for the scaled normal reaction pressure $\rho(\chi) = p\,\ell^\star/F^\star$.

Equations (III.1.28–III.1.30) indeed become

$$\eta^{-2}\alpha' + \varkappa_g\,(\alpha\,\varkappa_g)' + \varkappa_n\,(\alpha\,\varkappa_n)' = 0, \tag{III.1.38}$$

$$(\alpha\,\varkappa_g)'' - \frac{\alpha'}{\alpha}\,(\alpha\,\varkappa_g)' - \alpha^2\varkappa_g\,[\mathcal{F}_3 + \varkappa_t\,(\alpha\,\varkappa_t - \mathcal{M}_3)] - \frac{\big[\alpha\,\varkappa_n^2\,(\alpha\,\varkappa_t - \mathcal{M}_3)\big]'}{\varkappa_n} - \mathcal{M}_3\,(\alpha\,\varkappa_n)' = 0, \tag{III.1.39}$$

$$(\alpha\,\varkappa_n)'' - \frac{\alpha'}{\alpha}\,(\alpha\,\varkappa_n)' - \alpha^2\varkappa_n\,[\mathcal{F}_3 + \varkappa_t\,(\alpha\,\varkappa_t - \mathcal{M}_3)] + \frac{\big[\alpha\,\varkappa_g^2\,(\alpha\,\varkappa_t - \mathcal{M}_3)\big]'}{\varkappa_g} + \mathcal{M}_3\,(\alpha\,\varkappa_g)' = \alpha\,\rho, \tag{III.1.40}$$

where the axial component of the internal force reads $\mathcal{F}_3\,(\chi) = \eta^{-2}\,(\alpha - 1)$ and the dimensionless parameter $\eta^2 = F^\star/A = B/A\,\ell^{\star 2}$ is a measure of the rod *slenderness* that reflects the relative magnitude of the rod flexural and extensional stiffnesses. A consequence of the symmetric decomposition of the flexural strains (III.1.23–III.1.24) between the geodesic and normal curvatures is the parity of equations (III.1.39–III.1.40), whose left-hand sides are identical under permutation of $\varkappa_g$ and $\varkappa_n$ with a change of sign for the last two terms. Equations (III.1.35,III.1.38–III.1.40) constitute the set of equations governing the response of a weightless elastic rod constrained on a smooth surface.

Premultiplication of equation (III.1.38) by $\alpha\,(s)$ and integration yields

$$\alpha^2\left(\eta^{-2} + \varkappa_g^2 + \varkappa_n^2\right) = \alpha_0^2, \tag{III.1.41}$$

where $\alpha_0 > 0$ is a constant of integration. This expression relates the stretch, interpreted as the Jacobian of the mapping $s \mapsto \tilde{s}\,(s)$, to the rod intrinsic curvature $\varkappa = \sqrt{\varkappa_g^2 + \varkappa_n^2}$. Additionally, by combining the scaled versions of equations (III.1.28–III.1.30), an alternative expression for the reaction pressure is obtained

$$\rho\,(\chi) = -\frac{\left(\mathcal{F}_g^2 + \mathcal{F}_n^2 - \mathcal{F}_3^2\right)'}{2\,\mathcal{F}_n}, \tag{III.1.42}$$

which expresses its magnitude in terms of dynamical quantities rather than kinematical ones.

III.1.3.1 Weightless elastica and elastic curves

Inextensible rod models are common as the stretching strain $(\alpha - 1)$ is often small and negligible compared to the bending strains $\alpha\,\varkappa_g$ and $\alpha\,\varkappa_n$. A generalization of Euler's planar elastica model to arbitrary surfaces can be obtained easily by degenerating the governing equations (III.1.35, III.1.38–III.1.40) to their inextensible counterpart. Indeed, by letting $\eta^2 \to 0$ and $\alpha \to 1$ such that the product $\mathcal{F}_3 = \eta^{-2}\,(\alpha - 1)$ is finite, the constant twist moment equation (III.1.35)

becomes

$$(1+\nu)\,\mathcal{M}_3 = \varkappa_t + \psi', \tag{III.1.43}$$

while equation (III.1.38) may be re-written as

$$\mathcal{F}_3' + \varkappa_g\,\varkappa_g' + \varkappa_n\,\varkappa_n' = 0, \tag{III.1.44}$$

such that the axial component of the internal force reduces to

$$\mathcal{F}_3(\xi) = \mathcal{F}_0 - \frac{\varkappa_g^2 + \varkappa_n^2}{2}. \tag{III.1.45}$$

The parameter $\mathcal{F}_0$ is a constant of integration, corresponding to the axial force at points characterized by $\varkappa^2 = \varkappa_g^2 + \varkappa_n^2 = 0$. Accordingly, relations (III.1.39–III.1.40) become

$$\varkappa_g'' + \varkappa_g\left[\frac{\varkappa_g^2+\varkappa_n^2}{2} - \left(\varkappa_t - \frac{\mathcal{M}_3}{2}\right)^2 + \frac{\mathcal{M}_3^2}{4} - \mathcal{F}_0\right] - \frac{\left[\varkappa_n^2\left(\varkappa_t - \frac{\mathcal{M}_3}{2}\right)\right]'}{\varkappa_n} = 0, \tag{III.1.46}$$

$$\varkappa_n'' + \varkappa_n\left[\frac{\varkappa_g^2+\varkappa_n^2}{2} - \left(\varkappa_t - \frac{\mathcal{M}_3}{2}\right)^2 + \frac{\mathcal{M}_3^2}{4} - \mathcal{F}_0\right] + \frac{\left[\varkappa_g^2\left(\varkappa_t - \frac{\mathcal{M}_3}{2}\right)\right]'}{\varkappa_g} = \rho, \tag{III.1.47}$$

which are to be compared with the equations derived for *elastic surface curves* (Nickerson and Manning, 1988; Guven and Vázquez-Montejo, 2012; Guven et al., 2014). The intrinsic equations for these twist-less inextensible rods constrained on a smooth surface, which are obtained by minimizing the bending energy of curves along their length, may indeed be recovered by posing $\mathcal{M}_3 = 0$ in equations (III.1.46–III.1.47).

As a result of the similitudes between the Frenet-Serret and the Darboux formulas, the classic governing equations for an unconstrained elastica, see for instance equations (4.1a–4.1b) in (Shi and Hearst, 1994), may easily be retrieved by posing $\varkappa_n = \rho = 0$ while swapping the geodesic curvature and torsion with the elastica intrinsic curvature and torsion, respectively. This result may alternatively be obtained by observing that the triplet $(\varkappa_g, \varkappa_n, \varkappa_t)$ may be identified to the curvature functions of a curve in the Euclidean 4-space. The elastica being therefore confined to the three–dimensional space if $\varkappa_n$ vanishes uniformly.

III.1.3.2 Elastic string and geodesics

Rods with zero or negligible bending stiffness, *i.e.*, strings or cables, are of practical importance in a wide variety of applications. The soft string model, that ignores the bending stiffness of the drillstring, is for instance extensively used by the oil and gas industry. The scaling used to derive equations (III.1.38–III.1.40) is however not optimal to identify the rod behavior in this context as the characteristic force $F^\star = B/\ell^{\star 2}$ involves the rod bending stiffness.

These structures essentially resist transverse loads by means of large displacements and axial tension (Denoël and Detournay, 2009a). One may therefore denote by $F_0 > 0$ a representative value of the axial force, *e.g.* its magnitude at one extremity of the cable, and rescale the internal force and moment as $\overline{\boldsymbol{\mathcal{F}}}(\chi) = \boldsymbol{F}(s(\xi))/F_0$ and $\overline{\boldsymbol{\mathcal{M}}}(\chi) = \boldsymbol{M}(s(\xi))/\ell^* F_0$, respectively. Hence, equations (III.1.36–III.1.37) read

$$\alpha\,\overline{\mathcal{F}}_g = -\frac{B}{F_0\,\ell^{\star 2}}\left[(\alpha\,\varkappa_g)' - \alpha\,\varkappa_n\left(\alpha\,\varkappa_t - \overline{\mathcal{M}}_3\right)\right], \tag{III.1.48}$$

$$\alpha\,\overline{\mathcal{F}}_n = -\frac{B}{F_0\,\ell^{\star 2}}\left[(\alpha\,\varkappa_n)' + \alpha\,\varkappa_g\left(\alpha\,\varkappa_t - \overline{\mathcal{M}}_3\right)\right], \tag{III.1.49}$$

such that, assuming that the ratio $B/C = (1+\nu)$ remains constant, the geodesic and normal components of the shear force vanish for $B \to 0$, that is $\overline{\mathcal{F}}_g = \overline{\mathcal{F}}_n = 0$. Accordingly, equations (III.1.28–III.1.30) reduce to

$$\overline{\eta}^{-2}\alpha\,(\alpha-1)\,\varkappa_g + \overline{\sigma}_g = 0, \tag{III.1.50}$$

$$\overline{\eta}^{-2}\alpha\,(\alpha-1)\,\varkappa_n + \overline{\sigma}_n + \overline{\rho} = 0, \tag{III.1.51}$$

$$\overline{\eta}^{-2}\alpha' + \overline{\sigma}_3 = 0, \tag{III.1.52}$$

with $\overline{\eta}^2 = F_0/A$, the scaled body force $\overline{\boldsymbol{\sigma}}(\chi) = \ell^\star\, f(s(\chi))/F_0$ and reaction pressure $\overline{\rho}(\chi) = \ell^\star\, p(s(\chi))/F_0$. For cables of constant body weight, these equations may be interpreted as the extension to non planar surfaces of the notion of *catenary*.

In the absence of body force, *i.e.*, weightless catenary, these equations yield

$$\varkappa_g(\chi) = 0, \tag{III.1.53}$$

$$\overline{\rho}(\chi) = -\left(1+\overline{\eta}^2\right)\varkappa_n, \tag{III.1.54}$$

$$\alpha(\chi) = 1 + \overline{\eta}^2, \tag{III.1.55}$$

which emphasize the proportionality between the reaction pressure and the normal curvature. Equation (III.1.53) expresses that cables constrained to lie on a surface follow geodesics. Mathematically, a geodesic is a curve which is everywhere locally a distance minimizer and, therefore, presents an obvious mechanical lure as it minimizes the strain energy associated with the elongation of a cable constrained on a surface. According to the definition (III.1.13) of the geodesic curvature, imposing $\varkappa_g = 0$ leads to the establishment of geodesic equations. In dimensional form, these equations read (Gray, 1996, p 597)

$$u'' + \Gamma^1_{11}u'^2 + 2\,\Gamma^1_{12}u'\,v' + \Gamma^1_{22}v'^2 = 0, \tag{III.1.56}$$

$$v'' + \Gamma^2_{11}u'^2 + 2\,\Gamma^2_{12}u'\,v' + \Gamma^2_{22}v'^2 = 0, \tag{III.1.57}$$

with the Christoffel symbols $\Gamma^i_{jk}(u(S), v(S))$ defined in equations (III.1.14–III.1.16).

III.1.4 Benefits and shortcomings of the formulation

The particularization of the rod governing equations to surface bound configurations lead to an explicit representation of the rod centerline in which the strain variables, measuring the rod deformation, are expressed in terms of the geometric invariants $(\varkappa_g, \varkappa_n, \varkappa_t)$. As a result, the influence of the constraint local geometry on the configuration of the rod centerline and the reaction pressure has been emphasized. For regular boundary value problems associated with a fixed rod length $\ell = s_b - s_a$, the formulation (III.1.9) indeed may lead to a substantial improvement in the understanding of the rod behavior or simplify its governing equations.

The elementary problem defined in Section I.3.3 is however characterized by clamped-sliding sleeve boundary conditions that are responsible for the rod self-feeding, see Figure II.1.4. Alongside with the general Lagrangian formulation (II.1.1), this formulation therefore results in a free boundary problem and the boundary conditions specifying the locations $\boldsymbol{\mathcal{S}}(u(s_a), v(s_a))$ and $\boldsymbol{\mathcal{S}}(u(s_b), v(s_b))$ of the rod centerline at both extremities lead to the establishment of isoperimetric constraints, which again contribute to the numerical burden of the method.

It should additionally be stressed that solutions of physical interest are those associated with a normal reaction pressure of constant sign. For interior applications, such as the drilling problem, this reaction is indeed expected to be inward-pointing with the rod leaving the constraint where this pressure drops to zero. Conversely, exterior applications, such as the twinning plants problem, are meant to be associated with an outward-pointing reaction.

III.1.5 Application to spherical constraint

As a first insight into the behavior of rods in continuous contact with differentiable surfaces, consider a weightless elastic rod embedded on a sphere of radius R

$$\boldsymbol{\mathcal{S}}(u, v) = R(\cos u \cos v\, \boldsymbol{e}_1 + \cos u \sin v\, \boldsymbol{e}_2 + \sin u\, \boldsymbol{e}_3), \tag{III.1.58}$$

where $-\pi/2 \leq u \leq \pi/2$ and $0 \leq v \leq 2\pi$. Although leading to surprisingly complex equilibrium configurations, the sphere is a remarkably simple constraining surface. Due to its symmetry, all directions are indeed equivalent and both the normal curvature and geodesic torsion are constant, $\kappa_n = 1/R$ and $\tau_g = 0$. Hence, the arc-length parameter and the geometric invariants are naturally scaled by the radius of the sphere according to equations (III.1.34) with $\ell^\star = R$.

The elastica model being often favored for its simplicity, the continuous contact between the rod and the sphere is first investigated under the assumption of inextensibility. The broader problem of an extensible rod is then explored by relaxing this assumption.

III.1.5.1 Inextensible rod

According to equations (III.1.36–III.1.37,III.1.45) with $\alpha \to 1$, the scaled components of the internal force read

$$\mathcal{F}_g(\chi) = -\varkappa_g' - \mathcal{M}_3, \qquad \mathcal{F}_n(\chi) = \varkappa_g \mathcal{M}_3, \qquad \mathcal{F}_3(\chi) = \frac{\sigma - \varkappa_g^2}{2}, \tag{III.1.59}$$

where $\mathcal{M}_3$ and $\sigma = 2\mathcal{F}_0 - 1$ are two constants of integration. Similarly, equation (III.1.46) reduces to

$$2\varkappa_g'' + \varkappa_g\left(\varkappa_g^2 - \sigma\right) = 0, \tag{III.1.60}$$

which is known to be the intrinsic equation of a planar elastica with end tension 2σ (Lee and Forsythe, 1973; Brunnett, 1993). Using a variational approach, a similar equation has been obtained by Langer and Singer (1984a,b) for the curvature of regular curves in a 2–manifold of constant sectional curvature. Consequently, the geodesic curvature of an elastica constrained on a sphere and the intrinsic curvature of a planar elastica satisfy identical differential equations, an observation already made by Nickerson and Manning (1988) as well as Brunnett and Crouch (1994) and Guven and Vázquez-Montejo (2012). Note that stationary solutions of this equation are either geodesics, *i.e.*, $\varkappa_g(\chi) = 0$, or circles of constant geodesic curvature $\varkappa_g(\chi) = \pm\sqrt{\sigma}$. Finally, the reaction pressure $\rho(\chi) = p\,R/F^\star$ is obtained from equation (III.1.47) as

$$\rho(\chi) = \frac{\varkappa_g^2 - \sigma}{2} - \varkappa_g' \mathcal{M}_3, \tag{III.1.61}$$

which emphasizes that, although the geodesic curvature is unaffected by the magnitude of the twist, the reaction pressure depends on both the tension parameter σ and the twisting moment $\mathcal{M}_3$. For a planar constraining surface, *i.e.*, $\varkappa_n = \varkappa_t = 0$, equation (III.1.47) reduces to $\rho(\chi) = -\varkappa_g' \mathcal{M}_3$.

General solutions

While the formulation and the study of the planar elastica dates back to J. Bernoulli, the complete solution and characterization of this family of curves is generally attributed to L. Euler (Levien, 2008). Through the years, the planar elastica has been thoroughly investigated and solutions are now commonly classified in two families based on the presence or absence of inflection points (Love, 1927, pp. 402 – 405). Although, on the 2–sphere, the intrinsic curvature of an elastica is bounded from below by the constant normal curvature $\varkappa_n$, this classification is maintained in the following by reference to the geodesic curvature. If $\varkappa_g(\chi)$ is a non-trivial solution of equation (III.1.60), the squared geodesic curvature function $\varkappa_g^2(\chi)$ is known to have a global maximum $\varkappa_m^2 \neq 0$ that satisfies $\varkappa_m^2 \geq \sigma$ and conditions the nature of the solution (Brunnett, 1993). For *inflectional* or *wavelike* elastica, the global maximum squared curvature

satisfies $\varkappa_m^2 > 2\,\sigma$ and the solution reads

$$\varkappa_g(\chi) = \varkappa_m \operatorname{cn}\left(\frac{\chi - \chi_m}{2\,k}\varkappa_m, k^2\right), \tag{III.1.62}$$

with the abscissa χ_m such that $\varkappa_g^2(\chi_m) = \varkappa_m^2$ and

$$k^2 = \frac{\varkappa_m^2}{2\,(\varkappa_m^2 - \sigma)}. \tag{III.1.63}$$

Conversely, for $\varkappa_m^2 \leq 2\,\sigma$, the squared geodesic curvature satisfies $2\,\sigma - \varkappa_m^2 \leq \varkappa_g^2 \leq \varkappa_m^2$ and the elastica is said to be *non-inflectional* or *orbitlike*. The corresponding solution reads

$$\varkappa_g(\chi) = \varkappa_m \operatorname{dn}\left(\frac{\chi - \chi_m}{2}\varkappa_m, \frac{1}{k^2}\right). \tag{III.1.64}$$

In these expressions, $\operatorname{cn}(z, m)$ and $\operatorname{dn}(z, m)$ are the Jacobi elliptic cosine and delta amplitude functions of modulus m (Olver et al., 2010, ch. 22), respectively. Both inflectional and non-inflectional solutions are periodic with period $8\,k\,\mathrm{K}\left(k^2\right)/\varkappa_m$ for the former and $4\,\mathrm{K}\left(1/k^2\right)/\varkappa_m$ for the latter, where $\mathrm{K}(m)$ denotes the complete elliptic integral of the first kind of modulus m (Olver et al., 2010, p 553).

With the solutions (III.1.62) and (III.1.64) for the geodesic curvature $\varkappa_g(\chi)$, it is now straightforward to (numerically) integrate expression (III.1.13) under the unit speed condition $\alpha(\chi) = 1$ and obtain the coordinates $(u(\chi), v(\chi))$ of the elastica on the sphere. In the present context, the conservation of angular momentum (II.1.12) may however be integrated and an alternative coordinate system advantageously introduced. Due to the symmetry of the constraining surface, the reaction pressure is indeed everywhere aligned with the position vector of the elastica centerline and the total moment about the center of the sphere

$$\boldsymbol{\mathcal{I}} = \boldsymbol{\mathcal{M}} - \boldsymbol{N} \times \boldsymbol{\mathcal{F}}, \tag{III.1.65}$$

is constant along $\mathscr{E}$. Consistently introducing a cylindrical coordinate system $(\varrho, \vartheta, \zeta)$ with the ζ–axis along this natural direction, that is posing $\boldsymbol{\mathcal{I}} = \mathcal{I}\,\boldsymbol{e}_\zeta$ with $\mathcal{I} = \|\boldsymbol{\mathcal{I}}\|$, the scaled position vector reads $\boldsymbol{\varsigma}(\chi) = \varrho\,\boldsymbol{e}_\varrho + \zeta\,\boldsymbol{e}_\zeta$ with $\varrho^2 + \zeta^2 = 1$. Taking the inner product of both $\boldsymbol{\mathcal{I}}$ and $\boldsymbol{\varsigma}' \times \boldsymbol{\mathcal{I}}$ with $\boldsymbol{\varsigma}$ lead (see Appendix A.3.1)

$$\zeta(\chi) = -\frac{\varkappa_g}{\mathcal{I}}, \qquad\qquad \vartheta'(\chi) = \frac{2 + \sigma - \varkappa_g^2}{2\,\mathcal{I}\,(1 - \zeta^2)}, \tag{III.1.66}$$

for the axial component and the derivative of the polar angle, respectively. The former relation expresses the ζ–coordinate as a rescaling of the geodesic curvature such that $\zeta(\chi)$ and $\varkappa_g(\chi)$ share the same periodicity, extrema of both quantities being therefore concurrent. Additionally, while inflection points (in the geodesic sense) associated with wavelike solutions (III.1.62) arise

on the equator $\zeta = 0$, non-inflectional solutions (III.1.64) are confined to one hemisphere of the constraining sphere and never cross this geodesic. The latter relation in (III.1.66) expresses the derivative of the polar angle in terms of the squared geodesic curvature, solely. Finally, the radial component reads $\varrho(\chi) = \sqrt{1-\zeta^2}$ and is everywhere well-defined since

$$\mathcal{I}^2 = 1 + \frac{\varkappa_m^4 + \sigma^2}{4} + \frac{\sigma}{2}\left(2 - \varkappa_m^2\right), \tag{III.1.67}$$

is always larger than $\varkappa_m^2$ provided both $\varkappa_m$ and $\sigma \leq \varkappa_m^2$ are real, see Appendix A.3.2.

Closed solutions

Inflectional and non-inflectional solutions for the geodesic curvature $\varkappa_g(\chi)$ being periodic functions, the conditions under which the elastica closes around the sphere are now investigated. Both $\zeta(\chi)$ and $\varrho(\chi)$ having a periodicity compatible with that of the geodesic curvature in order for the elastica to close in an integer multiple of the period of $\varkappa_g$, one must ensure that the integral of $\vartheta'(\chi)$, as given in expression (III.1.66), over one period of $\varkappa_g$ is rationally related to 2π. Depending on the nature of the solution, this quantity may either be interpreted as the wavelength Λ of the inflectional elastica or the angular progression $\Delta\vartheta$ of its non-inflectional counterpart. This distinction, which legitimatizes the wavelike and orbit-like denominations, respectively, is emphasized in Figures III.1.3(a–b). Both families of solutions are investigated in the following.

Inflectional elastica $\left(\varkappa_m^2 > 2\sigma\right)$ Integrating expression (III.1.66) for the derivative of the polar angle over one period of the geodesic curvature and accounting for the symmetry of $\varkappa_g(\xi)$, the wavelength of closed inflectional solutions (III.1.62) reads

$$\begin{aligned}\Lambda(\sigma, \varkappa_m) &= \int_0^{8\,k\,\mathrm{K}\left(k^2\right)/\varkappa_m} \vartheta'(\chi)\,\mathrm{d}\chi, \\ &= \frac{k\,\mathcal{I}}{\varkappa_m}\left[\mathrm{K}\left(k^2\right) - \frac{2+\sigma-\mathcal{I}^2}{\varkappa_m^2-\mathcal{I}^2}\Pi\left(\frac{\varkappa_m^2}{\varkappa_m^2-\mathcal{I}^2}, k^2\right)\right],\end{aligned} \tag{III.1.68}$$

where $\Pi(n, m)$ is the complete elliptic integral of the third kind (Olver et al., 2010, ch. 19). This real valued function (over its domain) is even with respect to $\varkappa_m$, that is $\Lambda(\varkappa_0, \varkappa_m) = \Lambda(\varkappa_0, -\varkappa_m)$.

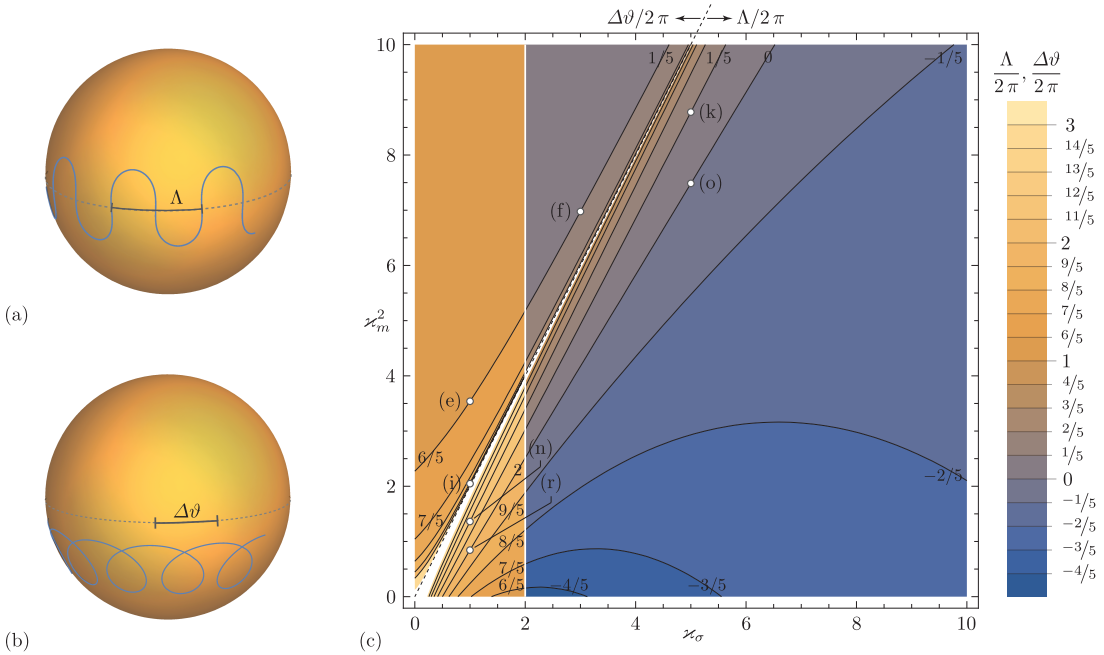

Figure III.1.3: Elastica on the sphere. Definition of (a) the wavelength Λ of an inflectional elastica ($\varkappa_m^2 > 2\,\sigma$ or $2\,\varkappa_\sigma > \varkappa_m^2$) and (b) the angular progression $\Delta\vartheta$ of an non-inflexional elastica ($\varkappa_m^2 \leq 2\,\sigma$ or $2\,\varkappa_\sigma \leq \varkappa_m^2$). (c) Contour representation of the scalar quantities $\Lambda/2\,\pi$ and $\Delta\vartheta/2\,\pi$ in the parameter space $\left(\varkappa_\sigma, \varkappa_m^2\right)$ with $\varkappa_\sigma = \varkappa_m^2 - \sigma$; closed solutions arise for rational values of these quantities. The white dots labeled (e,f,i,k,n,o,r) identify the corresponding closed solutions depicted in Figure III.1.4.

Non-inflectional elastica $\left(\varkappa_m^2 \leq 2\,\sigma\right)$ Similarly integrating expression (III.1.66) for $\vartheta'(\chi)$ over one period of the geodesic curvature, the angular progression of non-inflectional solutions (III.1.64) reads

$$\begin{aligned}\Delta\vartheta(\sigma,\varkappa_m) &= \int_0^{4\,\mathrm{K}\left(1/k^2\right)/\varkappa_m} \vartheta'(\chi)\,\mathrm{d}\chi,\\ &= \frac{\mathcal{I}}{\varkappa_m}\left[\mathrm{K}\left(\frac{1}{k^2}\right) - \frac{2+\sigma-\mathcal{I}^2}{\varkappa_m^2-\mathcal{I}^2}\Pi\left(\frac{\varkappa_m^2}{k^2\left(\varkappa_m^2-\mathcal{I}^2\right)},\frac{1}{k^2}\right)\right],\end{aligned} \tag{III.1.69}$$

which is odd with respect to $\varkappa_m$, *i.e*, $\Delta\vartheta(\sigma,\varkappa_m) = -\Delta\vartheta(\sigma,-\varkappa_m)$.

Irrespectively of the nature of the solution, the closure condition is seen to depend on the two constants σ and $\varkappa_m$ solely and is, therefore, uninfluenced by the twisting moment $\mathcal{M}_3$. Figure III.1.3(c) depicts the values taken by both quantities $\Lambda/2\,\pi$ and $\Delta\vartheta/2\,\pi$ in the parameter space $\left(\varkappa_\sigma,\varkappa_m^2\right)$ where $\varkappa_\sigma = \varkappa_m^2 - \sigma$ is a reduced tension parameter that is always non-negative since $\sigma \leq \varkappa_m^2$. Closed solutions arise along contours corresponding to rational values of the represented quantities. For a contour $\Lambda/2\,\pi = q$ or $\Delta\vartheta/2\,\pi = q$ with $q = n/m \in \mathbb{Q}$, the elastica closes after m periods of its geodesic curvature and going n times around the poles. Besides the boundary $\varkappa_m^2 = 2\,\varkappa_\sigma$ between wavelike and orbit-like solutions, the parameter space is traversed by characteristic curves marking the transitions between different varieties of solutions or corresponding to pathological behaviors. The straight lines $\varkappa_m = 0$ and $\varkappa_\sigma = 0$ are, for instance, associated with circular solutions along the equator and around the poles, respectively; the elastica reducing to one point for $\varkappa_m \to \pm\infty$. These straight lines contain the complete set of planar solutions attainable on the sphere. Additionally, the line $\varkappa_\sigma = 2$ corresponds to the passage of the elastica across the poles and, therefore, is associated with a discontinuity jump of $4\,\pi$ and $2\,\pi$ in the value of Λ and $\Delta\vartheta$, respectively.

A gallery of twenty closed elasticae is presented in Figure III.1.4. The position of each sphere in the Figure has been chosen to roughly match the coordinates of the represented solution in the parameter space $\left(\varkappa_\sigma,\varkappa_m^2\right)$. The dashed curve, which symbolizes the characteristic line $\varkappa_m^2 = 2\,\varkappa_\sigma$, marks the frontier between wavelike (below) and orbit-like (above) solutions. Although most solutions are represented from a lateral point of view, the south to north pole axis $\boldsymbol{e}_\zeta$ laying in the plane of the Figure, elasticae (a,b,c) and (e,f) are pictured as seen from a point situated below the south pole. Subfigures (m) and (q) depict two pathological solutions corresponding to circular elasticae around the south pole and the equator, respectively. As these solutions correspond to singular regions of the parameter space $\left(\varkappa_\sigma,\varkappa_m^2\right)$, they are not associated with a q value. The contour on which the inflectional solutions depicted in Subfigure (r,o,p) lay is crossed by the characteristic curve $\varkappa_\sigma = 2$ and, therefore, is associated with a jump in its value. This jump from $q = 2$ in (r) to $q = 0$ in (o) and (p) is seen to correspond to the passage of the elastica through the poles. Similar comments may be made regarding the solutions (n,k,l). Although also laying on rational contours that are crossed by the characteristic curve $\varkappa_\sigma = 2$,

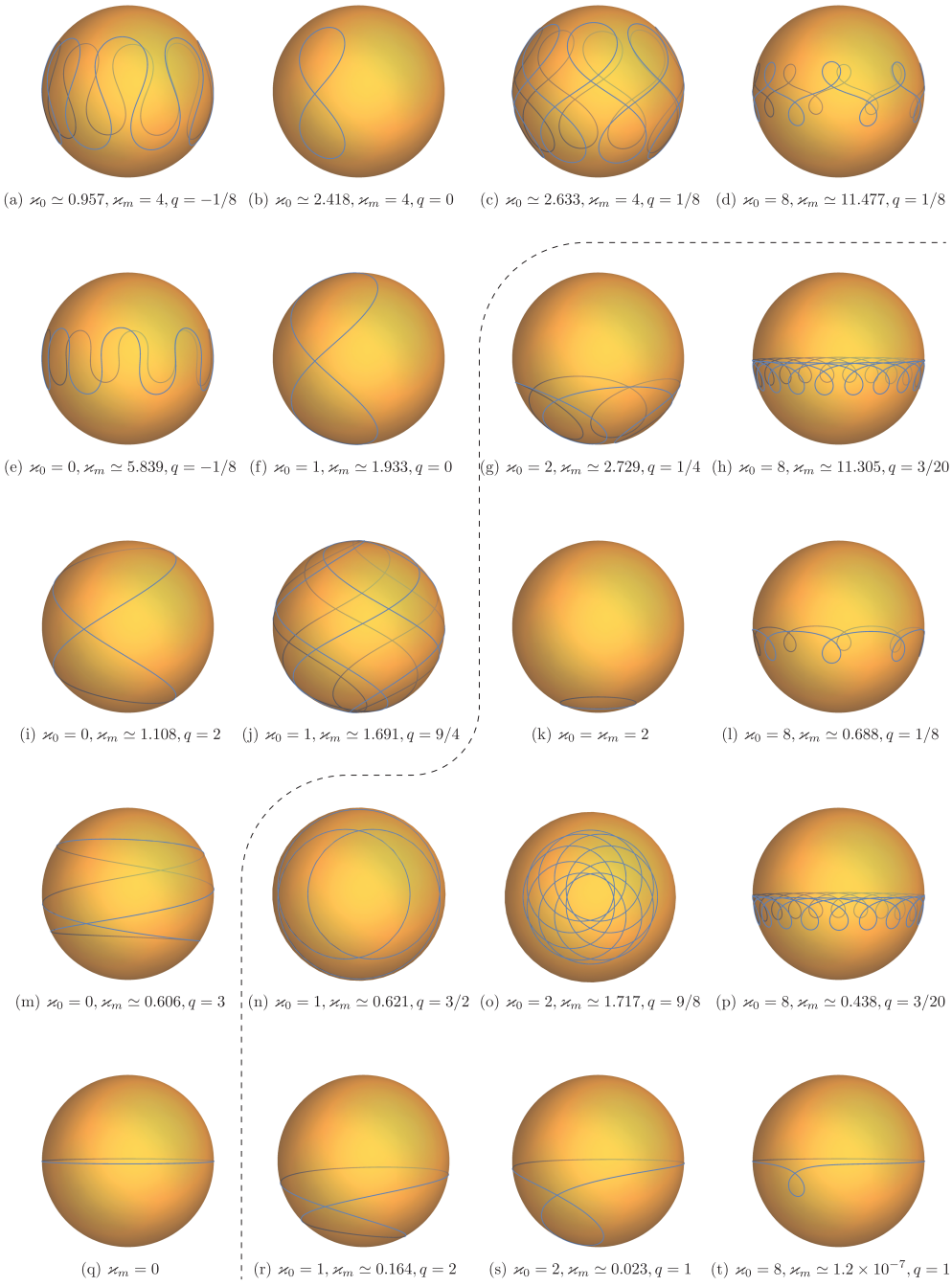

Figure III.1.4: Gallery of closed elasticae on the sphere. The positions of the sphere in the Figure schematically correspond to the coordinates $(\varkappa_0, \varkappa_m)$ of the represented solutions in the associated parameter space. The dashed curve, symbolizing the characteristic line $\varkappa_m^2 = 2\,\varkappa_0^2$, marks the frontier between wavelike (above) and orbit-like (below) solutions. Depending on the nature of the depicted elastica, the value $q \in \mathbb{Q}$ corresponds to $\Lambda/2\,\pi$ or $\Delta\vartheta/2\,\pi$. Although most solutions are represented from a lateral point of view, elasticae (a,b,c) and (e,f) are pictured as seen from a point situated below the south pole.

the sets of non-inflectional elasticae (a,b,c,d), (e,f) and (i,g,h) are associated with a unitary jump in their respective contour value as these solutions are confined to one hemisphere of the constraint.

III.1.5.2 Extensible rod

Relaxation of the inextensibility assumption slightly complicates the rod governing equations. The parallelism with planar configurations that was emphasized in the previous Section is however carried over to extensible rods. With $\varkappa_n(\chi) = 1$ and $\varkappa_t(\chi) = 0$, equation (III.1.39) for the rod geodesic curvature indeed becomes

$$\left(\frac{(\alpha\,\varkappa_g)'}{\alpha}\right)' - \eta^{-2}(\alpha - 1)\,\alpha\,\varkappa_g = 0, \tag{III.1.70}$$

where, according to equation (III.1.41), the stretch reads $\alpha^2\left(1 + \eta^{-2} + \varkappa_g^2\right) = \alpha_0^2$. Although the stretch of the rod reduces to $\alpha^2\left(\eta^{-2} + \varkappa_g^2\right) = \alpha_0^2$ for planar configurations, equation (III.1.70) is identical to the intrinsic equation of its planar counterpart. Stationary solutions of this equation are again either geodesics, *viz.* $\varkappa_g(\chi) = 0$ with $\alpha(\chi) = \alpha_0/\sqrt{1+\eta^{-2}}$, or circles characterized by $\varkappa_g(\chi) = \pm\sqrt{\alpha_0^2 - \eta^{-2} - 1}$ and $\alpha(\chi) = 1$. Similarly, equation (III.1.40) yields

$$\rho(\chi) = -\eta^{-2}\alpha(\alpha - 1) - \varkappa_g'\mathcal{M}_3 + \left(\frac{\alpha'}{\alpha}\right)', \tag{III.1.71}$$

for the reaction pressure.

Due to the nonlinearities of equation (III.1.70) and the entanglement between the stretch $\alpha(\chi)$ and the geodesic curvature $\varkappa_g(\chi)$, closed-form solutions for elastic rods constrained on a sphere are, to the author's knowledge, unfortunately not available. The symmetry of the problem is however not affected by the extensibility of the rod and the total moment about the center of the sphere (III.1.65) is again conserved along $\mathscr{E}$. Its constant magnitude reads

$$\mathcal{I}^2\left(\varkappa_g, \varkappa_g'\right) = \left[\frac{(\alpha\,\varkappa_g)'}{\alpha}\right]^2 + \left(\alpha + \eta^{-2}(\alpha - 1)\right)^2 + (\alpha\,\varkappa_g)^2, \tag{III.1.72}$$

which reduces to its inextensible counterpart (A.3.9) for $\eta \to 0$ provided the constant of integration $\alpha_0 > 0$ is determined such that the axial force $\mathcal{F}_3$ of the rod and that of the elastica are equal at points of zero geodesic curvature, that is

$$\alpha_0 = \sqrt{1+\eta^{-2}}\left(\frac{\sigma\,\eta^2}{2} + 1\right). \tag{III.1.73}$$

From this definition, it appears that one must further require $\sigma\,\eta^2 > -2$ to ensure the injectivity of the mapping $s \mapsto \bar{s}(s)$ and preserve the rod orientation along its centerline.

The phase portrait of the total moment $\mathcal{I}\left(\varkappa_g, \varkappa_g'\right)$ is presented in Figure III.1.5(a) for two

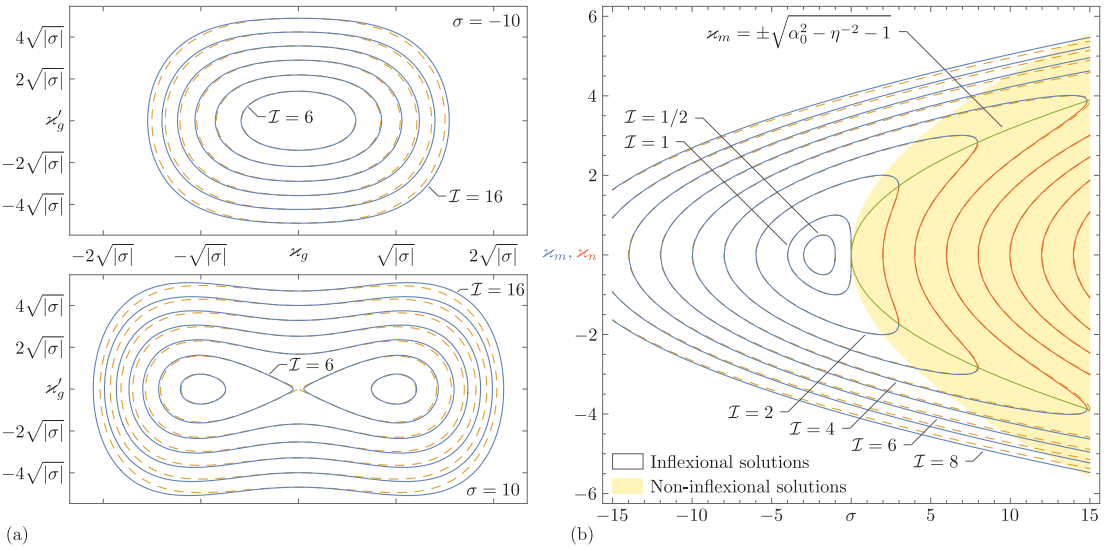

Figure III.1.5: Extensible rod ($\eta = 1/20$) on the sphere. (a) Phase portraits of the total moment about the center of the sphere $\mathcal{I}\left(\varkappa_g, \varkappa_g'\right)$ for $\sigma = -10$ and $\sigma = 10$. Orbits associated with the extensible rod (solid lines) are compared to their elastica counterpart (dashed lines). (b) Extrema $\varkappa_m, \varkappa_n$ of the geodesic curvature as a function of both the total moment $\mathcal{I}$ and the tension parameter σ. The pale yellow region comprehends the set of non-inflexional solutions and the green curve identifies the stationary solutions characterized by $\varkappa_m = \pm\sqrt{\alpha_0 - \eta^{-2} - 1}$.

values of the tension parameter σ and $\eta = 1/20$. The extensible rod model, described by equation (III.1.72) and depicted in solid lines, is compared to the elastica model, specified by equation (A.3.9) and pictured in dashed lines. Each curve represents a different orbit associated with a given value of $\mathcal{I}$. Two distinct families of orbits may be identified and the distinction between inflectional and non-inflectional solutions appears to be carried to extensible rods. Orbits centered on the origin $(0, 0)$ and crossing the line $\varkappa_g = 0$ are indeed associated with inflectional or wavelike solutions, while orbits around the stationary solutions $\left(\pm\sqrt{\alpha_0^2 - \eta^{-2} - 1}, 0\right)$ correspond to non-inflectional or orbit-like solutions. Both families of orbits being closed, they are associated with periodic solutions.

While inflectional solutions are associated with a symmetric range of the geodesic curvature $\varkappa_g \in [-\varkappa_m, \varkappa_m]$, non-inflectional solutions are bounded to an asymmetric range $\varkappa_g \in [\varkappa_n, \varkappa_m]$, with $|\varkappa_n| < |\varkappa_m|$, that is confined to either negative or positive values. Posing $\varkappa_g' = 0$ in expression (III.1.72) for the total moment $\mathcal{I}$, the extrema $\varkappa_m, \varkappa_n$ of the geodesic curvature may be obtained as functions of both the total moment $\mathcal{I}$ and the tension parameter σ. Figure III.1.5(b) compares these ranges of amplitudes (solid lines) to their inextensible counterparts (dashed lines) for discrete values of $\mathcal{I}$. The frontier between inflectional and non-inflectional solutions may be obtained by elimination of the total moment about the centre of the sphere from

$\mathcal{I}(0,0) = \mathcal{I}(\varkappa_m, 0)$. Disregarding the trivial solution $\varkappa_m = 0$, yields

$$\varkappa_m^2 = \frac{8\,\sigma\left(1+\eta^{-2}\right)}{\eta\left(\sigma - 2\,\eta^{-2}\right)^2}, \tag{III.1.74}$$

which reduces to $\varkappa_m^2 = 2\,\sigma$ for $\eta \to 0$. The pale yellow region in Figure III.1.5(b) represents the set of non-inflexional solutions, *viz.* solutions associated with values of $\varkappa_m^2$ lower than the right-hand side of expression (III.1.74). Finally, the green curve identifies the stationary solutions characterized by $\varkappa_m = \pm\sqrt{\alpha_0 - \eta^{-2} - 1}$ and $\alpha = 1$.

III.2 Eulerian formulation adapted to normal ringed surface

The formulation (III.1.9) presented in Section (III.1) adapts the general Lagrangian formulation of elastic rods to surface bound rods, without restriction regarding the nature of the surface provided its orientability. In this curve-angle representation, the coordinates $(u(s), v(s))$ of the rod centerline in the parameter space associated with the parameterization $\boldsymbol{\mathcal{S}}(u,v)$ of the constraint surface are defined as smooth functions of the Lagrangian coordinate s. In some circumstances, it may however be beneficial to substitute this parametric representation of the rod centerline with an explicit one of the form $(u, v(u))$ along with the mapping $u \mapsto s(u)$, from the independent variable to the Lagrangian curvilinear coordinate.

Normal ringed surfaces are generated by sweeping a circle of variable radius along a directrix curve and, therefore, distinguish by possessing circles as one family of parameter lines. In this context, the formulation (III.1.9) may indeed be particularized to account for this specific feature. Aiming at a formulation comparable to the Eulerian description of the rod governing equations introduced in Section (II.2), the Lagrangian parameterization (III.1.1) for surface bound rods is re-written as

$$\boldsymbol{r}(s(S)) = \boldsymbol{\mathcal{S}}(S, \beta(S)), \tag{III.2.1}$$

where, as shown next, $\beta(S) = v(s(S))$ is the angular position of the rod centerline in the cross section of the constraint. The parameter S is again referred to as the Eulerian curvilinear coordinate, the reason for conserving this nomenclature will become clear in the following. Note however that this curvilinear coordinate differs from the (natural) Lagrangian coordinate s, parameterizing the rod in its unstressed configuration, and the stretched coordinate $\bar{s}$, associated with the arc-length parameterization of the rod in its deformed configuration.

The interest of this Eulerian description of surface bound rods relies on the role played by the directrix curve in the definition of normal ringed surfaces and their particularity of possessing circles as one family of parameter lines. Also this family of surfaces presents an

obvious appeal for torque-and-drag applications and the simulation of minimally invasive medical interventions. In the following, the general geometric features of this class of surfaces are first briefly investigated. Starting from the parameterization (III.2.1), the details and the scope of the proposed formulation are then explored. Henceforth, derivatives of scalar and vector valued functions with respect to the Eulerian coordinate S will be denoted by the apposition of a prime while derivatives with respect to the Lagrangian coordinate s and the stretched coordinates $\bar{s}$ are explicitly specified.

III.2.1 Geometry of the constraint

In Chapter I, the constraint surface $\mathscr{S}$ has been defined generically as a perfectly stiff *normal ringed surface*, that is a surface generated by sweeping a circle with variable radius along a directrix curve $\mathscr{C}$ while maintaining the circle in the normal plane to the directrix (Johnstone, 1993; Aumann, 1995), see Figure III.2.1. This broad class of surfaces has been investigated mainly for blending purposes or shape reconstruction in computer-aided design. Well-known subclasses include *canal surfaces*, which are defined as the envelopes of a one-parameter family of spheres (Bastl et al., 2014; Bizzarri and Lávička, 2015), as well as *pipe surfaces* (generated by spheres of constant radius) and *surfaces of revolution* (generated by spheres whose centers are located on a straight line.) These surfaces belong to the general class of *swept surfaces*, which are defined as the envelopes of a one-parameter family of cross-sectional curves.

The constraint surface $\mathscr{S}$ is the normal ringed surface parameterized by

$$[S_a, S_b] \times [0, 2\,\pi[\ni (S, \beta) \mapsto \boldsymbol{\mathcal{S}}(S, \beta) \in \mathbb{E}^3, \tag{III.2.2}$$

with $\boldsymbol{\mathcal{S}}(S, \beta)$ defined as the envelope of a one–parameter family of circles with radii $Q(S)$ and centers $\boldsymbol{R}(S)$, hence

$$\boldsymbol{\mathcal{S}}(S, \beta) = \boldsymbol{R}(S) + Q(S)\,(\cos\beta\,\boldsymbol{D}_1 + \sin\beta\,\boldsymbol{D}_2)\,, \tag{III.2.3}$$

where the pair of unit orthogonal vectors $\boldsymbol{D}_1(S)\,, \boldsymbol{D}_2(S)$ spans the normal plane to the directrix $\mathscr{C}$, indistinctly referred to as the *reference curve* in the present context. As in Chapter II, the parameterization $\boldsymbol{R}(S)$ of this space curve is assumed to be arc-length with the triplet of orthonormal vectors $\{\boldsymbol{D}_j\}$ defined such that $\boldsymbol{R}'(S) = \boldsymbol{D}_3$ is the unit vector tangent to $\mathscr{C}$ for all S. The kinematics of this adapted frame along the directrix may univocally be described by means of a Darboux vector $\boldsymbol{U}(S) = U_j\,\boldsymbol{D}_j$ satisfying the skew-symmetric relation (II.2.1). As previously emphasized, there is more than one way to frame a curve (Bishop, 1975) and, although the choice of orthonormal frame does not affect the properties of the constraint surface or the rod's deformed configuration, some definitions may result in a substantially simpler formulation. Defining the $\{\boldsymbol{D}_j\}$–basis such that it constitutes a Bishop natural frame is again advocated as this adapted frame, also referred to as parallel transport frame, has zero twist uniformly, *i.e.*,

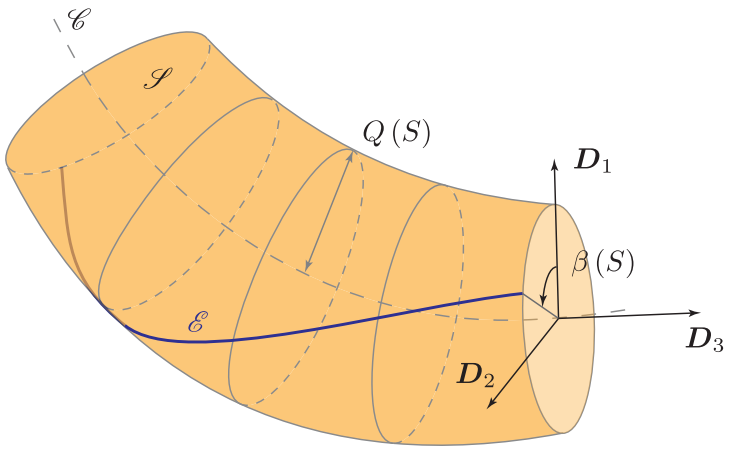

Figure III.2.1: Elastic rod constrained to lie on a normal ringed surface $\mathscr{S}$. The constraint is defined as the surface generated by sweeping a circle with variable radius $Q\,(S)$ along a directrix curve $\mathscr{C}$ while maintaining the circle in the normal plane to the directrix. The position of the rod centerline on the surface reduces to the knowledge of the polar angle $\beta\,(S)$ along the directrix.

$U_3\,(S) = 0$ and is everywhere well-defined. Conversely, and in spite of its natural appeal, the Frenet-Serret apparatus may lead to existence and continuity issues as it ceases to be defined at points where $\boldsymbol{R}'$ and $\boldsymbol{R}''$ are not linearly independent, *viz.* where the curvature of the directrix $K = \sqrt{U_1^2 + U_2^2}$ vanishes. Note finally that, comparing the parameterization (III.2.3) of normal ringed surfaces with the definition (II.2.2) of the eccentricity vector, the angle $\beta\,(S)$ may be related to the components of the eccentricity vector as $\tan\beta = \Delta_2/\Delta_1$.

Although canal surfaces have been investigated more thoroughly than ringed surfaces, it has been shown that all normal ringed surfaces with rational directrix and radius function are rational (Lü and Pottmann, 1996; Bizzarri and Lávička, 2015). Additionally, the normal ringed surface $\boldsymbol{\mathcal{S}}\,(S, \beta)$ is locally n–times continuously differentiable, *i.e.*, C^n, if the directrix curve is of class C^{n+1} and the radius function $Q\,(S)$ of class C^n (Hartmann, 2001). Denoting partial derivatives by subscripts, the surface is said to be regular if it is smooth and the vectors $\boldsymbol{\mathcal{S}}_S$ and $\boldsymbol{\mathcal{S}}_\beta$ are linearly independent at all points (S, β). Using the first fundamental form, the necessary condition for normal ringed surfaces without local self-intersections, that is singular points where $\boldsymbol{\mathcal{S}}_S \times \boldsymbol{\mathcal{S}}_\beta = \boldsymbol{0}$, may be expressed as $Q\,K < 1$ and $Q' \neq 0$. Details of this result are presented in Appendix A.4.

III.2.2 Mappings and Jacobians

As in Section II.2, the restatement of the rod local equilibrium (II.1.12–II.1.13) within the Eulerian framework requires to substitute the Lagrangian curvilinear coordinate s by the mapping

$s \mapsto s(S)$ and express the natural derivatives $\mathrm{d}\cdot/\mathrm{d}s$ in terms of Eulerian derivatives $\mathrm{d}\cdot/\mathrm{d}S$. Following the methodology applied in the previous Chapter, the Jacobian of the mapping $S \mapsto s(S)$ from Eulerian to Lagrangian coordinates is obtained by differentiating expression (III.2.1) with respect to the Eulerian coordinate

$$s'(S) = \pm \left\| \boldsymbol{\mathcal{S}}_S + \beta' \boldsymbol{\mathcal{S}}_\beta \right\| / \left\| \boldsymbol{v} \right\|. \tag{III.2.4}$$

Besides the similitude between this expression and the Jacobian (II.1.12) derived in the previous Chapter, note that the drift existing between the two curvilinear coordinates is again two-fold. Rewriting this Jacobian in terms of the coefficients of the first fundamental form, *viz.*

$$s'(S) = \alpha^{-1} \sqrt{E + 2F\beta' + G\beta'^2}, \tag{III.2.5}$$

the two components of this drift are readily identifiable as *(i)* the arc-length of a line element on the surface $\mathscr{S}$ along $\mathscr{E}$, and *(ii)* the stretch $\|\boldsymbol{v}\| = \alpha$ of the rod itself. As in Section II.2, imposing the mapping $s(S)$ to be increasing by selecting the positive sign in expression (III.2.4) restricts the range of potential configurations adopted by the rod and prevents the appearance of parasitic solutions associated with curling, writhing or other configurations involving self-contact. The first fundamental form being positively definite, expression (III.2.5) is always well-defined provided $\beta(S)$ is a smooth function of the Eulerian coordinate.

Redefining the stretch as $\alpha(S) = \mathrm{d}\bar{s}/\mathrm{d}s\big|_{s=s(S)}$ and resorting to a notation comparable to the one introduced previously, the Eulerian functions $J_k(S)$ and $\bar{J}_k(S)$ are redefined as

$$J_k(S) = \left.\frac{\mathrm{d}^k S}{\mathrm{d}s^k}\right|_{s=s(S)}, \qquad \bar{J}_k(S) = \left.\frac{\mathrm{d}^k S}{\mathrm{d}\bar{s}^k}\right|_{\bar{s}=\bar{s}(S)}, \tag{III.2.6}$$

with $J_1(S) = 1/s'(S)$ and $\bar{J}_1 = 1/\bar{s}'(S)$ the Jacobians of the mappings $s \mapsto S(s)$, from Lagrangian to Eulerian coordinates, and $\bar{s} \mapsto S(\bar{s})$, from stretched to Eulerian coordinates, respectively. Similarly, the recursive relations

$$J_k(S) = J'_{k-1} J_1, \qquad \bar{J}_k(S) = \bar{J}'_{k-1} \bar{J}_1, \tag{III.2.7}$$

for $k > 1$ and the circular relation $J_1 = \alpha \bar{J}_1$ previously introduced remain valid.

III.2.3 Directors and strain variables

In the Lagrangian description of surface bound rods introduced in the previous Section, the director $\boldsymbol{d}_3$ is expressed as a linear combination of $\boldsymbol{\mathcal{S}}_u$ and $\boldsymbol{\mathcal{S}}_v$, both laying in the tangent plane to the constraint surface and aligned with the parametric curves embedded in $\boldsymbol{\mathcal{S}}(u, v)$. Similarly, differentiating the parameterization (III.2.1) of the surface curve $\mathscr{E}$ with respect to the Eulerian

coordinate, the rod local inclination reads

$$\boldsymbol{d}_3\,(S) = \bar{J}_1\,(\boldsymbol{\mathcal{S}}_S + \beta'\boldsymbol{\mathcal{S}}_\beta)\,, \tag{III.2.8}$$

which is to compare with equation II.2.6 obtained for the general Eulerian formulation, *i.e.*, not specific to continuous contact configurations.

The objective of this section being to highlight the relations between the geometrical features of the rod centerline and the constraint surface, the rotation of the rod cross section about its axis is described with respect to the Darboux frame attached to $\mathscr{E}$ rather than the intermediate $\{\boldsymbol{k}_j\}$–basis as in Section II.2. This distinction is essential to the adaptation of the Eulerian formulation to normal ringed surfaces. Therefore, with the unit normal to the constraint surface (III.1.6), the rotation of the pair $\{\boldsymbol{d}_1, \boldsymbol{d}_2\}$ about $\boldsymbol{d}_3$ is specified through the angle $\psi\,(S)$ they subtend with the normal and geodesic directions, that is

$$\boldsymbol{d}_1\,(S) = \cos\psi\,\boldsymbol{N}\times\boldsymbol{d}_3 + \sin\psi\,\boldsymbol{N}, \tag{III.2.9}$$

$$\boldsymbol{d}_2\,(S) = -\sin\psi\,\boldsymbol{N}\times\boldsymbol{d}_3 + \cos\psi\,\boldsymbol{N}. \tag{III.2.10}$$

The tangent and normal vectors, $\boldsymbol{N}\times\boldsymbol{d}_3$ and $\boldsymbol{N}$, are indeed preferred to $\boldsymbol{k}_1$ and $\boldsymbol{k}_2$, which are in general neither tangent nor perpendicular to $\mathscr{S}$.

To account for the change of parameterization of the surface curve $\mathscr{E}$, the kinematics (III.1.10–III.1.12) of the Darboux frame is adapted as

$$\bar{J}_1\,\boldsymbol{d}_3' = \kappa_g\,\boldsymbol{N}\times\boldsymbol{d}_3 + \kappa_n\,\boldsymbol{N}, \tag{III.2.11}$$

$$\bar{J}_1\,(\boldsymbol{N}\times\boldsymbol{d}_3)' = -\kappa_g\,\boldsymbol{d}_3 + \tau_g\,\boldsymbol{N}, \tag{III.2.12}$$

$$\bar{J}_1\,\boldsymbol{N}' = -\kappa_n\,\boldsymbol{d}_3 - \tau_g\,\boldsymbol{N}\times\boldsymbol{d}_3, \tag{III.2.13}$$

where the geodesic curvature $\kappa_g\,(S,\beta)$, the normal curvature $\kappa_n\,(S,\beta)$ and the geodesic torsion $\tau_g\,(S,\beta)$, being geometrical invariants, maintain identical values as they are not affected by the re-parameterization. Their expressions in the Eulerian parameterization of the rod centerline are obtained by substituting $u\,(s) \rightharpoonup S$ and $v\,(s) \rightharpoonup \beta\,(S)$ in their definitions (III.1.13,III.1.18–III.1.19), which yield

$$\begin{aligned}\kappa_g\,(S) = \sqrt{\frac{E\,G - F^2}{(E + 2\,F\,\beta' + G\,\beta'^2)^3}}\,\big[&\Gamma^2_{11} + \beta'' \\ &+ \left(2\,\Gamma^2_{12} - \Gamma^1_{11}\right)\beta' - \left(2\,\Gamma^1_{12} - \Gamma^2_{22}\right)\beta'^2 - \Gamma^1_{22}\beta'^3\big]\,,\end{aligned} \tag{III.2.14}$$

$$\kappa_n\,(S) = \frac{e + 2\,f\,\beta' + g\,\beta'^2}{E + 2\,F\,\beta' + G\,\beta'^2}, \tag{III.2.15}$$

$$\tau_g\,(S) = \frac{(f\,E - e\,F) + (g\,F - f\,G)\,\beta'^2 + (g\,E - e\,G)\,\beta'}{(E + 2\,F\,\beta' + G\,\beta'^2)\,\sqrt{E\,G - F^2}}, \tag{III.2.16}$$

where the Christoffel symbols are similarly obtained from equations (III.1.14–III.1.16). As to the strain variables $u_j(S)$, their expressions (III.1.23–III.1.25) in terms of the geometric invariants remain valid provided the Eulerian curvilinear coordinate is substituted for the Lagrangian one and differentiations account for this change of variable. In the Darboux frame, they read

$$u_g(S) = -\alpha\,\kappa_n, \qquad u_n(S) = \alpha\,\kappa_g, \qquad u_3(S) = \alpha\,\tau_g + J_1\psi', \tag{III.2.17}$$

with $u_g(S) = \boldsymbol{u}\cdot(\boldsymbol{N}\times\boldsymbol{d}_3)$ and $u_n(S) = \boldsymbol{u}\cdot\boldsymbol{N}$.

III.2.4 Dimensionless governing equations and boundary conditions

Due to inherent similarities between the general Eulerian formulation and its adaptation to normal ringed surfaces, the scaling introduced in this Section closely follows the one introduced in Section II.2.3 on page 27. The Eulerian coordinate S is therefore naturally scaled by the known length of the boundary value problem, $L = S_b - S_a$, leading to the introduction of the dimensionless curvilinear coordinate $\xi = (S - S_a)/L$. Analogously scaling the Lagrangian and stretched curvilinear coordinates by L, the stretch is redefined as $\alpha(\xi) \coloneqq \alpha(S(\xi))$ while the Jacobians (III.2.6) read

$$\mathcal{J}_k(\xi) = L^{k-1} J_k(S(\xi)), \qquad \bar{\mathcal{J}}_k(\xi) = L^{k-1}\bar{J}_k(S(\xi)), \tag{III.2.18}$$

for $k \geq 1$. Denoting again by $F^\star = B/L^2$ the characteristic force, the following vector fields are defined

$$\boldsymbol{\mathcal{F}}(\xi) = \boldsymbol{F}(S(\xi))/F^\star, \qquad \boldsymbol{\mathcal{M}}(\xi) = \boldsymbol{M}(S(\xi))/LF^\star, \tag{III.2.19}$$

$$\boldsymbol{\sigma}(\xi) = L\,\boldsymbol{f}(S(\xi))/F^\star, \qquad \boldsymbol{\mu}(\xi) = \boldsymbol{m}(S(\xi))/F^\star, \tag{III.2.20}$$

for the scaled internal force and moment, body force and body couple scale, respectively. Hence, according to the constitutive relation (III.1.27), the dimensionless counterpart to the strain variables (III.2.17) are analogous to the projection of the scaled internal moment in the Darboux frame

$$\mathcal{M}_g(\xi) = L\,u_g, \qquad \mathcal{M}_n(\xi) = L\,u_n, \qquad \mathcal{M}_3(\xi) = L\,u_3(1+\nu)^{-1}, \tag{III.2.21}$$

with $(1+\nu) = B/C$ where, for rods with a circular cross section, ν is Poisson's ratio. Similarly, the geometric invariants scale as

$$\varkappa_g(\xi) = L\,\kappa_g(S(\xi)), \qquad \varkappa_n(\xi) = L\,\kappa_n(S(\xi)), \qquad \varkappa_t(\xi) = L\,\tau_g(S(\xi)), \tag{III.2.22}$$

while both the angular position and the rotation angle are redefined as

$$\beta(\xi) \coloneqq \beta(S(\xi)), \qquad \psi(\xi) \coloneqq \psi(S(\xi)). \tag{III.2.23}$$

Scaling the surface parameterization (III.2.3) by the characteristic length L, the previous definitions for the dimensionless radius function $\epsilon(\xi) = Q(S(\xi))/L$ and the Darboux vector $\boldsymbol{\mathcal{U}}(\xi) = L\,\boldsymbol{U}(S(\xi))$ remain valid leading to

$$\mathsf{E}(\xi) = E(S(\xi), \beta(\xi)), \qquad \mathsf{e}(\xi) = L\,e(S(\xi), \beta(\xi)), \tag{III.2.24}$$

$$\mathsf{F}(\xi) = F(S(\xi), \beta(\xi))/L, \qquad \mathsf{f}(\xi) = f(S(\xi), \beta(\xi)), \tag{III.2.25}$$

$$\mathsf{G}(\xi) = G(S(\xi), \beta(\xi))/L^2, \qquad \mathsf{g}(\xi) = g(S(\xi), \beta(\xi))/L, \tag{III.2.26}$$

for the scaled coefficients of the first and second fundamental forms, respectively. According to relations (III.2.5) and (III.2.6), the first Jacobians therefore read

$$\bar{\mathcal{J}}_1(\xi) = \frac{1}{\sqrt{\mathsf{E} + 2\,\mathsf{F}\,\beta' + \mathsf{G}\,\beta'^2}}, \tag{III.2.27}$$

and $\mathcal{J}_1(\xi) = \alpha\,\bar{\mathcal{J}}_1$, where primes now denote differentiation with respect to the dimensionless coordinate ξ.

Substituting the definitions (III.2.19) and (III.2.22) in the constitutive relations (III.1.26–III.1.27) leads to

$$\boldsymbol{\mathcal{F}}(\xi) = \mathcal{F}_g\,\boldsymbol{N} \times \boldsymbol{d}_3 + \mathcal{F}_n\,\boldsymbol{N} + \eta^{-2}(\alpha - 1)\,\boldsymbol{d}_3, \tag{III.2.28}$$

$$\boldsymbol{\mathcal{M}}(\xi) = \alpha\,\varkappa_g\,\boldsymbol{N} - \alpha\,\varkappa_n\,\boldsymbol{N} \times \boldsymbol{d}_3 + (1+\nu)^{-1}(\alpha\,\varkappa_t + \mathcal{J}_1\,\psi')\,\boldsymbol{d}_3, \tag{III.2.29}$$

with the dimensionless parameter $\eta^2 = F^\star/A$ already introduced in Section II.2.3. Accordingly, the projection of the equilibrium equations (II.1.12–II.1.13) in the Darboux frame yields

$$\mathcal{J}_1\,\mathcal{F}_g' + \alpha\left(\varkappa_g(\alpha - 1)\,\eta^{-2} - \varkappa_t\,\mathcal{F}_n\right) + \sigma_g = 0, \tag{III.2.30}$$

$$\mathcal{J}_1\,\mathcal{F}_n' + \alpha\left(\varkappa_t\,\mathcal{F}_g + \varkappa_n(\alpha - 1)\,\eta^{-2}\right) + \sigma_n + \rho = 0, \tag{III.2.31}$$

$$\mathcal{J}_1\,\alpha' - \alpha\,(\varkappa_g\,\mathcal{F}_g + \varkappa_n\,\mathcal{F}_n)\,\eta^2 + \sigma_3\,\eta^2 = 0, \tag{III.2.32}$$

$$\mathcal{J}_1(\alpha'\,\varkappa_n + \alpha\,\varkappa_n') + \frac{\alpha\,\varkappa_g}{1+\nu}(\alpha\,\varkappa_t\,\nu - \mathcal{J}_1\,\psi') + \alpha\,\mathcal{F}_n - \mu_g = 0, \tag{III.2.33}$$

$$\mathcal{J}_1\left(\alpha'\,\varkappa_g + \alpha\,\varkappa_g'\right) - \frac{\alpha\,\varkappa_n}{1+\nu}(\alpha\,\varkappa_t\,\nu - \mathcal{J}_1\,\psi') + \alpha\,\mathcal{F}_g + \mu_n = 0, \tag{III.2.34}$$

$$\mathcal{J}_1^2\,\psi'' + \mathcal{J}_2\,\psi' + \mathcal{J}_1\,(\alpha'\,\varkappa_t + \alpha\,\varkappa_t') + (1+\nu)\,\mu_3 = 0, \tag{III.2.35}$$

with $\rho(\xi)$ the scaled reaction pressure, $(\sigma_g(\xi), \sigma_n(\xi), \sigma_3(\xi))$ and $(\mu_g(\xi), \mu_n(\xi), \mu_3(\xi))$ the projections of the dimensionless body force and body couple in the Darboux frame. Further substitution of the definitions (III.2.14–III.2.16) for the geometric invariants and (A.4.7–A.4.9,A.4.11–A.4.13) for the coefficients of the first and second fundamental forms, leads to a system of differential algebraic equations. Solving equation III.2.33 for the normal component $\mathcal{F}_n$ of the internal force, the remaining equations of the system involves two first order ODE's, (III.2.30–III.2.32), in $\alpha(\xi)$ and $\mathcal{F}_g(\xi)$; one second order, (III.2.35), in $\psi(\xi)$; and one third order, (III.2.34), for the polar angle $\beta(\xi)$; and one algebraic equation, (III.2.31), for the reaction pressure $\rho(\xi)$. Again, although easily derived, the resulting system is cumbersome and will not be explicitly presented here.

Due to the decrease in the number of degrees of freedom along continuous contacts, the resulting system requires the specification of only seven constants of integration (compared to the eleven ones prescribed in Section II.2.3). The Eulerian counterpart to the boundary conditions (II.1.16) prescribing the clamped extremity of the rod reads

$$\{\psi(0), \beta(0), \beta'(0)\}, \tag{III.2.36}$$

which can be recovered from the boundary conditions (II.2.54), associated with the general Eulerian formulation, by imposing the magnitude of the eccentricity vector, that is $\|\boldsymbol{\delta}\| = \epsilon$. At the opposite extremity of the boundary value problem, the position of the rod centerline and the orientation of its unit tangent are imposed together with the axial force and twisting moment. According to the constitutive relations (III.2.28–III.2.29), the boundary conditions (II.1.17) corresponding to a frictionless sliding sleeve become

$$\{\alpha(1), \psi'(1), \beta(1), \beta'(1)\}, \tag{III.2.37}$$

which are to compare with the boundary conditions (II.2.55). Besides the benefits resulting from the particularization of the rod governing equations to surface bound configurations, the suppression of the isoperimetric constraints, an acknowledged source of difficulty associated with the specification of the rod location at its extremities in the Lagrangian formulation, contributes to the global interest of the proposed formulation.

In Section II.2, the Eulerian description of the rod configuration led to a curve-angle representation involving the components $\delta_1(\xi), \delta_2(\xi)$ of the eccentricity vector and the angle $\varphi(\xi)$ characterizing the rotation of the rod cross section about the director $\boldsymbol{d}_3$. Similarly, the rod configuration along a continuous contact with a normal ringed surface $\mathscr{S}$ parameterized by $\boldsymbol{\mathcal{S}}(\xi, \beta)$ reduces to the knowledge of the two Eulerian functions

$$[0,1] \ni \xi \mapsto \beta(\xi), \psi(\xi) \in \mathbb{R}, \tag{III.2.38}$$

with the boundaries $\xi = \{0, 1\}$ of the canonical problem corresponding to the rod extremities s_a

and s_b, respectively. In this alternative curve-angle representation, the rod centerline is explicitly described by the polar angle $\beta(\xi)$ corresponding to its angular position on the constraint surface while the rotation of the material frame is characterized by the angle $\psi(\xi)$, which generally differs from $\varphi(\xi)$. Although this Eulerian description of surface bound rods is, in all respects, comparable to the Eulerian formulation derived in Section II.2 for contact-free configurations, the number of degrees of freedom is decreased by one as the rod is compelled to lie on the constraint surface. The formulation (III.2.38) may indeed be recovered from the general Eulerian formulation (II.2.56) by imposing the magnitude of the eccentricity vector, that is $\|\boldsymbol{\delta}(\xi)\| = \epsilon(\xi)$. The normal reaction pressure $\rho(\xi)$, ensuring the continuous contact with the constraint surface, remains however *a priori* unknown. The relation giving its magnitude in terms of the Eulerian functions $\beta(\xi), \psi(\xi)$ is readily obtained by projecting the conservation of linear momentum on the unit normal to $\mathscr{S}$.

Specific constraint: Bishop pipe surface

In many applications of practical interest, the radius function of the constraint surface is constant or varies only slightly at the lengthscale of the continuous contact. Hence, the constraint surface may often be regarded as a canal surface with $\epsilon'(\xi) = 0$. Additionally, the adapted frame $\{\boldsymbol{D}_j\}$ attached to the constraint directrix may always be defined such that it constitutes a Bishop natural frame, *viz.* $\mathcal{U}_3(\xi) = 0$. In the following paragraphs, the geometric features characterizing such a *Bishop pipe surface* are investigated. The geometric features characterizing the general normal ringed surface, *i.e.*, not Bishop-like and with $Q' \neq 0$, are presented in Appendix A.4. In this context, the (dimensionless) partial derivatives $\boldsymbol{\mathcal{S}}_\xi(\xi,\beta) = \partial\boldsymbol{\mathcal{S}}/\partial\xi$ and $\boldsymbol{\mathcal{S}}_\beta(\xi,\beta) = \partial\boldsymbol{\mathcal{S}}/\partial\beta$ of the constraint surface parameterization (III.2.3) read

$$\boldsymbol{\mathcal{S}}_\xi(\xi,\beta) = (1 + \epsilon(\mathcal{U}_1 \sin\beta - \mathcal{U}_2 \cos\beta))\,\boldsymbol{D}_3, \tag{III.2.39}$$

$$\boldsymbol{\mathcal{S}}_\beta(\xi,\beta) = \epsilon(-\sin\beta\,\boldsymbol{D}_1 + \cos\beta\,\boldsymbol{D}_2), \tag{III.2.40}$$

such that

$$\|\boldsymbol{\mathcal{S}}_\xi \times \boldsymbol{\mathcal{S}}_\beta\|^2 = \epsilon^2(1 + \epsilon(\mathcal{U}_1 \sin\beta - \mathcal{U}_2 \cos\beta))^2, \tag{III.2.41}$$

and the Bishop pipe surface with constant radius function ϵ has no self-intersection if and only if $1 + \epsilon(\mathcal{U}_1 \sin\beta - \mathcal{U}_2 \cos\beta) \neq 0$. Expressing the components of the Darboux vector as $\mathcal{U}_1(\xi) = \mathcal{K}\sin\Phi$ and $\mathcal{U}_2(\xi) = \mathcal{K}\cos\Phi$ with the directrix curvature $\mathcal{K}(\xi)$, the latter condition may be rewritten as $1 - \epsilon\mathcal{K}\cos(\beta + \Phi) \neq 0$ such that, since $\cos(\beta + \Phi)$ varies between -1 and 1, there will be no self-intersection if $\epsilon\mathcal{K} < 1$.

First fundamental form Equations (III.1.3) for the coefficients of the first fundamental form lead to

$$\mathsf{E}(\xi,\beta) = (1+\epsilon(\mathcal{U}_1\sin\beta - \mathcal{U}_2\cos\beta))^2, \qquad \mathsf{F}(\xi,\beta) = 0, \qquad \mathsf{G}(\xi,\beta) = \epsilon^2, \tag{III.2.42}$$

and the Christoffel symbols defined in equations (III.1.14–III.1.16) reduce to

$$\Gamma^1_{11}(\xi,\beta) = \frac{\epsilon(\mathcal{U}_1'\sin\beta - \mathcal{U}_2'\cos\beta)}{1+\epsilon(\mathcal{U}_1\sin\beta - \mathcal{U}_2\cos\beta)}, \tag{III.2.43}$$

$$\Gamma^1_{12}(\xi,\beta) = \frac{\epsilon(\mathcal{U}_1\cos\beta + \mathcal{U}_2\sin\beta)}{1+\epsilon(\mathcal{U}_1\sin\beta - \mathcal{U}_2\cos\beta)}, \tag{III.2.44}$$

$$\Gamma^2_{11}(\xi,\beta) = -\epsilon^{-1}(1+\epsilon(\mathcal{U}_1\sin\beta - \mathcal{U}_2\cos\beta))(\mathcal{U}_1\cos\beta + \mathcal{U}_2\sin\beta), \tag{III.2.45}$$

and $\Gamma^1_{22}(\xi,\beta) = \Gamma^2_{22}(\xi,\beta) = \Gamma^2_{12}(\xi,\beta) = 0$, where $\Gamma^c_{ab}(\xi,\beta)$ is the nondimensionalized form of $\Gamma^c_{ab}(S,\beta)$.

Second fundamental form Let $\boldsymbol{N}(\xi,\beta)$ be the outward pointing unit normal to the surface $\boldsymbol{\mathcal{S}}(\xi,\beta)$ given by

$$\boldsymbol{N}(\xi,\beta) = \varsigma(\cos\beta\,\boldsymbol{D}_1 + \sin\beta\,\boldsymbol{D}_2), \tag{III.2.46}$$

with $\varsigma = \operatorname{sign}(1+\epsilon(\mathcal{U}_1\sin\beta - \mathcal{U}_2\cos\beta))$. Then, according to equations (III.1.17), the coefficients of the second fundamental form read

$$\mathsf{e}(\xi) = -\sqrt{\mathsf{E}}(\mathcal{U}_1\sin\beta - \mathcal{U}_2\cos\beta), \qquad \mathsf{f}(\xi) = 0, \qquad \mathsf{g}(\xi) = -\varsigma\,\epsilon. \tag{III.2.47}$$

Geometric invariants Accordingly, the geometric invariants $(\varkappa_g, \varkappa_n, \varkappa_t)$ defined in equations (III.2.14–III.2.16) read

$$\varkappa_g(\xi) = \sqrt{\frac{\mathsf{E}\,\mathsf{G}}{(\mathsf{E}+\mathsf{G}\,\beta'^2)^3}}\left(\Gamma^2_{11} + \beta'' - \Gamma^1_{11}\,\beta' - 2\,\Gamma^1_{12}\,\beta'^2\right), \tag{III.2.48}$$

$$\varkappa_n(\xi) = \frac{\mathsf{e}+\mathsf{g}\,\beta'^2}{\mathsf{E}+\mathsf{G}\,\beta'^2}, \tag{III.2.49}$$

$$\varkappa_t(\xi) = \frac{(\mathsf{g}\,\mathsf{E} - \mathsf{e}\,\mathsf{G})\,\beta'}{(\mathsf{E}+\mathsf{G}\,\beta'^2)\sqrt{\mathsf{E}\,\mathsf{G}}}, \tag{III.2.50}$$

such that the governing equations (III.2.30–III.2.35) substantially simplify.

III.2.5 Application to torus knots

Due to their simplicity and topology, tori constitute an appealing subclass of normal ringed surfaces to investigate the behavior of rods in continuous contact. Open and closed curves lying

on the surface of a torus have indeed been studied from various perspectives, from knot theory to the quantization of energy levels in models of atoms (Jantzen, 2010). Additionally, free elasticae (understand weightless and contact-free) are known to lie on tori of revolution (Shi and Hearst, 1994; Ivey and Singer, 1999), however with a nearly but not precisely circular cross section. Closed solutions have further been shown to be in a 1-to-1 correspondence with torus knots.

In this Section, we consider a weightless and inextensible rod constrained to lie on the (circular) torus

$$\boldsymbol{\mathcal{S}}(S,\beta) = (R + Q\,\cos\beta)\cos\frac{S}{R}\,\boldsymbol{e}_1 + (R + Q\,\cos\beta)\sin\frac{S}{R}\,\boldsymbol{e}_2 + Q\,\sin\beta\,\boldsymbol{e}_3, \tag{III.2.51}$$

where $0 \leq S \leq 2\pi\,R$ and $0 \leq \beta \leq 2\pi$. Supposing $Q < R$, R and Q are referred to as the *major* and *minor* radii, respectively. Further assuming the constraining surface to be frictionless, the body couple is taken identically null such that the normal reaction pressure arising from the contact constitutes the sole loading acting on the elastica. In the following, we consider closed solutions on the (circular) torus that are topologically equivalent to (p,q)–torus knots, where p, q are relatively prime. These solutions, referred to as *elastic torus knots*, loop through the hole of a torus p times with q revolutions before joining their ends. As the length of a rod that circle around the torus and satisfies periodic boundary conditions is *a priori* unknown, the Eulerian formulation derived in this Chapter is particularly well adapted to investigate this family of solutions.

In this context, both the Eulerian coordinate and the geometric invariants are scaled by the major radius as $\xi = S/R$ and

$$\varkappa_g(\xi) = \kappa_g(S(\xi))\,R, \qquad \varkappa_n(\xi) = \kappa_n(S(\xi))\,R, \qquad \varkappa_t(\xi) = \tau_g(S(\xi))\,R, \tag{III.2.52}$$

such that, according to (III.1.20–III.1.22),

$$\varkappa_g(\xi) = \bar{\mathcal{J}}_1\vartheta' + \varkappa_\xi\,\cos\vartheta + \varkappa_\beta\,\sin\vartheta, \tag{III.2.53}$$

$$\varkappa_n(\xi) = \varkappa_1\,\cos^2\vartheta + \varkappa_2\,\sin^2\vartheta, \tag{III.2.54}$$

$$\varkappa_t(\xi) = (\varkappa_2 - \varkappa_1)\cos\vartheta\,\sin\vartheta, \tag{III.2.55}$$

where the elastica local inclination in the orthogonal parameterization of the torus, see equations (III.2.42), satisfies

$$\tan\vartheta = \frac{\epsilon\,\beta'}{1 + \epsilon\,\cos\beta}, \tag{III.2.56}$$

while the surface principal curvatures and the geodesic curvatures of the parameter lines read

(Gray, 1996, pp. 384–385, 587)

$$\varkappa_1(\xi) = -\frac{\cos\beta}{1+\epsilon\cos\beta}, \qquad \varkappa_2(\xi) = -\frac{1}{\epsilon}, \qquad \varkappa_\xi(\xi) = \frac{\sin\beta}{1+\epsilon\cos\beta}, \qquad \varkappa_\beta(\xi) = 0, \tag{III.2.57}$$

respectively, with $\epsilon = Q/R$ and the Jacobian (III.2.27) given by

$$\bar{\mathcal{J}}_1(\xi) = \frac{\cos\vartheta}{1+\epsilon\cos\beta}, \tag{III.2.58}$$

with $\vartheta \in [-\pi/2, \pi/2]$.

We consider first the planar solutions embedded on the torus. At any point of this surface, four families of circles can be drawn. One is parallel to the equatorial plane of the torus ($\vartheta = 0$), an other is perpendicular to it ($\vartheta = \pi/2$) and the other two are Villarceau circles, which meet every parallel circle at the same angle $\vartheta = \arcsin\epsilon$ (Melzak, 2014, pp. 63–72). According to equations (III.2.53–III.2.55), the former families of circles, *i.e.*, parallels ($\vartheta = 0$) and meridians ($\vartheta = \pi/2$), are characterized by constant values of the geometric invariants ($\varkappa_g, \varkappa_n = \text{cst.}, \varkappa_t = 0$) and, as expected, are solutions of the governing equations (III.1.46–III.1.47) provided

$$\varkappa_g \mathcal{F}_3 = 0, \tag{III.2.59}$$

where $\mathcal{F}_3$ is the constant axial force along the elastica. One may therefore distinguish geodesics ($\varkappa_g = 0$) that are associated with a non-zero reaction pressure $\rho = -\varkappa_n \mathcal{F}_3$ from non-geodesic parallels corresponding to $\vartheta = 0$ and $\beta \neq 0 + k\,\pi$ (with $k \in \mathbb{N}$), which are associated with a zero reaction pressure. On the other hand, accounting for the constant inclination $\sin\vartheta = \epsilon$ along the Villarceau circles, equation (III.2.56) can be integrated with, without loss of generality, $\beta(0) = 0$ such that the polar angle reads

$$\tan\frac{\beta}{2} = \sqrt{\frac{1+\epsilon}{1-\epsilon}}\tan\frac{\xi}{2}, \tag{III.2.60}$$

while equations (III.2.53–III.2.55) and (III.2.57) yield

$$\varkappa_g(\xi) = \sin\xi, \qquad \varkappa_n(\xi) = -\cos\xi, \qquad \varkappa_t(\xi) = -\frac{1-\epsilon\cos\xi}{\sqrt{1-\epsilon^2}}. \tag{III.2.61}$$

It can easily be shown that these circles are solutions of equations (III.1.46–III.1.47) for $\mathcal{F}_3(\xi) = 0$ and are associated with a zero reaction pressure.

Although the parallels and meridians are not *sensu stricto* knots, the Villarceau circles are probably the most simple knots on the torus with $(p, q) = (1, 1)$. Unfortunately, to the author's knowledge, no closed form solutions exists for higher order *elastic torus knots* and one must resort to numerical techniques to gain insight into these solutions. As their thorough study

and classification is beyond the scope of this work, only a few elastic torus knots are presented in the following. Using the collocation method detailed in Section IV.1.1.2, the system of differential-algebraic equations (III.2.30–III.2.35) is solved on the domain $\xi \in [0, 2\pi\, q]$ to account for overlapping of the torus and under periodic boundary conditions, that is

$$\beta\,(2\pi\, q) - \beta\,(0) = 2\pi\, p, \qquad\qquad \beta'\,(0) = \beta'\,(2\pi\, q) = c, \tag{III.2.62}$$

where c is chosen such that the rod internal force and moment are continuous across the boundaries of the domain. As it will become clear in Section III.3, imposing $\mathcal{F}_n\,(0) = \mathcal{F}_n\,(2\pi\, q)$ is sufficient to achieve this continuity and properly close the problem. According to the definition (III.2.48–III.2.50) of the geometric invariants $(\varkappa_g, \varkappa_n, \varkappa_t)$ and equation (III.1.37), this condition indeed ensures the periodicity of $\beta''\,(\xi)$ and, therefore, the continuity of the internal force and moment.

A gallery of trivial, *i.e.*, with either p or q equal to 1 or -1, elastic torus knots is presented in Figure III.2.2 for $\epsilon = 1/5$, $\mathcal{F}_3\,(0) = 0$ and $\mathcal{M}_3 = 0$. For each solution, the offset $\beta\,(S) - p\,\xi/q$ with respect to the corresponding torus solenoid as well as the reaction pressure $\rho\,(S)$ are depicted. It is seen that these knots are associated with positive reaction pressures, that is pointing outward along the constraint normal, and thus present a physical interest in exterior applications. Alternatively, large negative values of $\mathcal{F}_3\,(0)$ may lead to elastic torus knots associated with inward-pointing reaction pressure, *i.e.*, negative, such as the one depicted in Figure III.2.3(a). Figure III.2.4 depicts three simple nontrivial elastic torus knots, namely the trefoils $(2, 3)$ and $(3, 2)$ as well as the cinquefoil $(2, 5)$, for $\epsilon = 1/5$, $\mathcal{F}_3\,(0) = 0$ and $\mathcal{M}_3 = 0$.

Finally, this family of solutions allow us to validate the Eulerian formulation derived in this Chapter. According to the results presented in Section III.1.3.2, as the imposed axial force $\mathcal{F}_3\,(0)$ is increased, elastic torus knots indeed converge towards the closed geodesics to which they are topologically equivalent; the reaction pressure being proportional to the normal curvature, see equation (III.1.54). This is exemplified in Figure III.2.3 for the elastic torus knot $(1, 5)$.

III.3 Point contact with a differentiable surface

Although the notion of continuous contact is generally well apprehended, the concept of point contact is somehow less obvious. In the previous Sections, the continuous contact of elastic rods has been investigated through the theory of surface bound curves by assuming the space curve $\mathscr{E}$, materializing the rod centerline, to be restricted to the constraint surface $\mathscr{S}$ along its non-zero length. Emphasizing the influence of the constraint geometry on the rod deformed configuration and the reaction pressure, it was shown that these geometrical objects share fundamental geometric features. For instance, the surface normal curvature κ_n along the rod centerline was shown to match the orthogonal projection of the rod intrinsic curvature $\kappa\,\boldsymbol{n}$ on the unit normal $\boldsymbol{N}$ to the constraint surface, see equation (III.1.10). While it could be tempting to consider

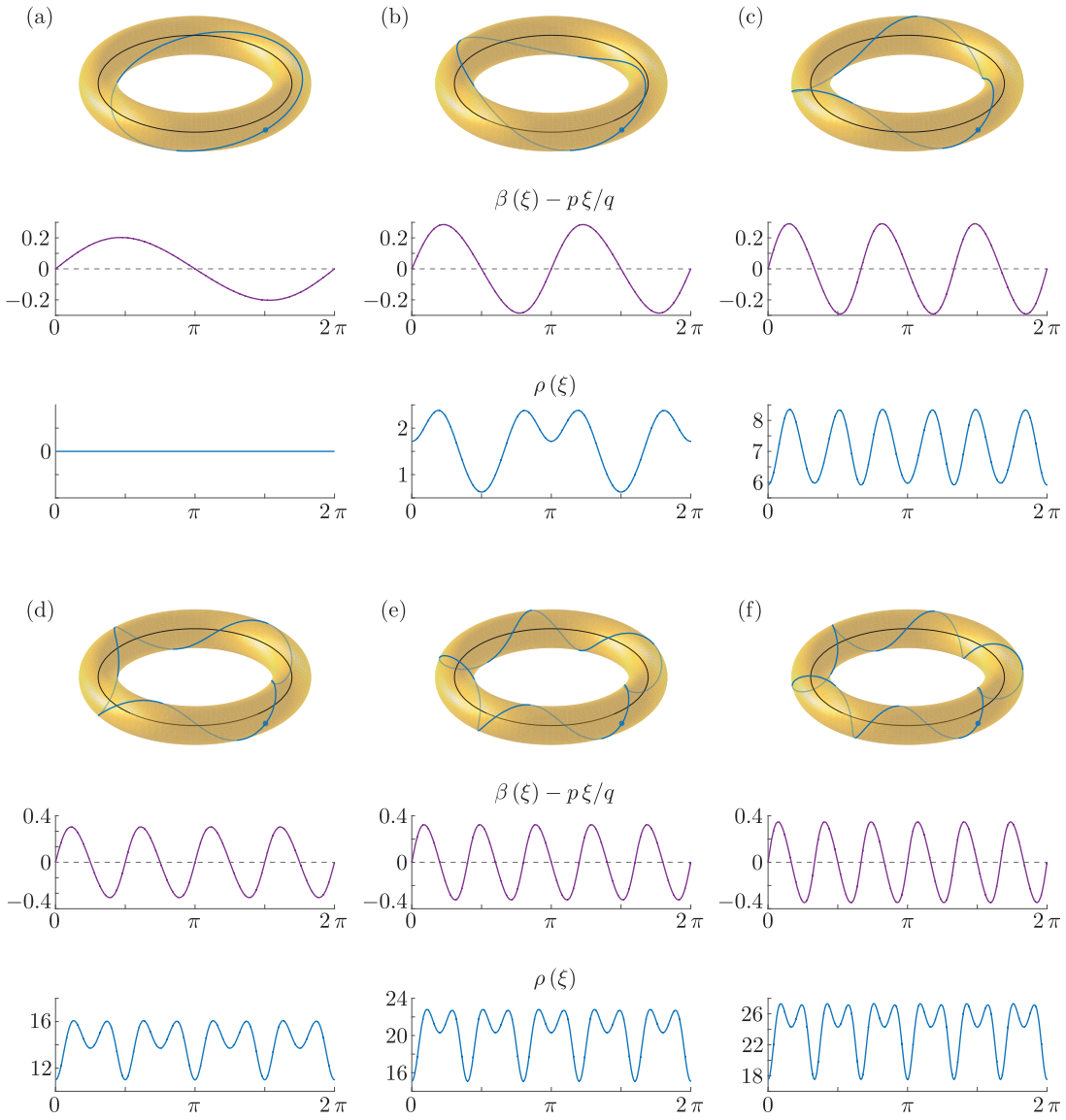

Figure III.2.2: Gallery of trivial elastic torus knots obtained for $\epsilon = 1/5$, $\mathcal{F}_3(0) = 0$ and $\mathcal{M}_3 = 0$: (a) Villarceau circle $(1,1)$, (b) type $(1,2)$, (c) type $(1,3)$, (d) type $(1,4)$, (e) type $(1,6)$, and (f) type $(1,6)$.

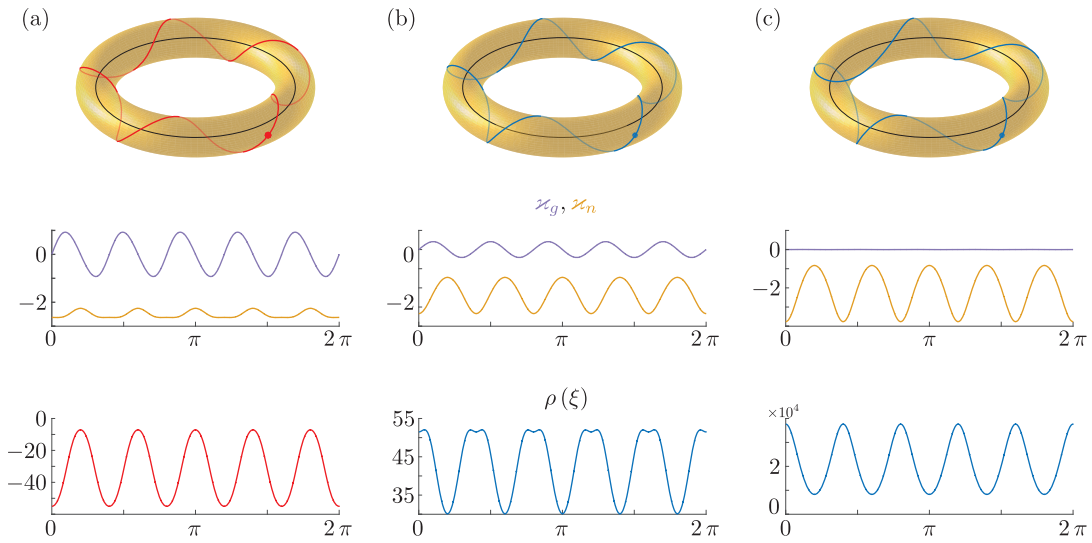

Figure III.2.3: Influence of the axial force on the elastic torus knots $(1,5)$ for $\epsilon = 1/5$ and $\mathcal{M}_3 = 0$: (a) $\mathcal{F}_3(0) = -20$, (b) $\mathcal{F}_3(0) = 10$ and (c) $\mathcal{F}_3(0) = 10^4$. On the torus, the elastica is drawn in blue where the reaction pressure is positive (exterior problem) and in red where it is negative (inside problem).

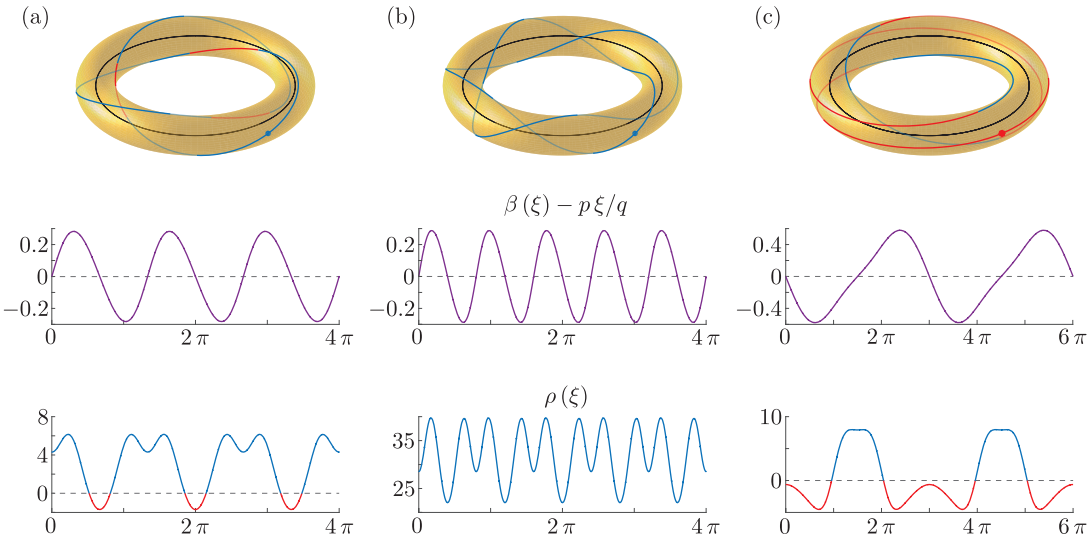

Figure III.2.4: Gallery of nontrivial elastic torus knots for $\epsilon = 1/5$, $\mathcal{F}_3(0) = 0$ and $\mathcal{M}_3 = 0$: (a) the trefoil knot $(2,3)$, (b) the cinquefoil $(2,5)$ and (c) the trefoil $(3,2)$. On the torus, the elastica is drawn in blue where the reaction pressure is positive and in red where it is negative.

point contacts as continuous ones whose lengths have shrunk to zero, this would lead to the erroneous conclusion that, at these points, this relation between the rod curvature and the constraint surface normal curvature remains valid. In the following, we indeed show that, at a point contact, the rod curvature is not determined by the constraint local geometry and, therefore, should be distinguished from continuous contacts of zero length.

III.3.1 Geometrical considerations

In differential geometry, the notion of contact slightly differs from the one commonly acknowledged in mechanics. Two geometrical objects (*e.g.* two curves or surfaces, a curve and a surface) are indeed said to have a contact on the sole condition that they share a common intersection point, therefore disregarding the tangency requirement essential in mechanics. The foundations of contact geometry of curves and surfaces were laid by Lagrange (1797) and Cauchy (1826) with the introduction of the concept of *contact order*. A space curve $\mathscr{E}$ parameterized by $\boldsymbol{r}(s)$ and a surface $\mathscr{S}$ defined by $\boldsymbol{\mathcal{S}}(u,v)$ are said to have a contact of order $n \in \mathbb{N}$ at $\boldsymbol{r}(s_c) = \boldsymbol{\mathcal{S}}(u_c, v_c)$ if there exists a regular parameter transform $s \mapsto (u^\star(s), v^\star(s))$ such that

$$\frac{\mathrm{d}^k}{\mathrm{d}s^k}\boldsymbol{r}(s_c) = \frac{\mathrm{d}^k}{\mathrm{d}s^k}\boldsymbol{\mathcal{S}}(u^\star(s_c), v^\star(s_c)), \tag{III.3.1}$$

for $k = 0, \dots, n$. The existence of a point contact between a rod and a regular constraint surface, in the conventional mechanical sense, therefore requires a contact order of at least 1.

III.3.2 Mechanical considerations

Assuming the constraint to be frictionless, the reaction force developing at a point contact between an elastic rod and a perfectly stiff constraint is aligned with the local normal to the constraint and balances the jump discontinuity in the shear components of the internal force. In the absence of concentrated external loading or other singularities, *e.g.* localized body couple or force, both the internal moment $\boldsymbol{\mathcal{M}}$ and the axial component $\mathcal{F}_3$ of the internal force are indeed continuous across the discrete contact.

Assuming a point contact at $\xi = \xi_c$, the tangency of the rod centerline with the constraint surface is sufficient to identify the Darboux frame $\{\boldsymbol{d}_3, \boldsymbol{N} \times \boldsymbol{d}_3, \boldsymbol{N}\}$ at this point of $\mathscr{S}$ and project the internal force $\boldsymbol{\mathcal{F}}(\xi_c)$ and moment $\boldsymbol{\mathcal{M}}(\xi_c)$ onto these directions. Hence, denoting by $\mathcal{R}$ the magnitude of the reaction force, the rod satisfies

$$[\![\mathcal{F}_g(\xi_c)]\!] = 0, \qquad [\![\mathcal{F}_n(\xi_c)]\!] = \mathcal{R}, \qquad [\![\mathcal{F}_3(\xi_c)]\!] = 0, \tag{III.3.2}$$

$$[\![\varkappa_g(\xi_c)]\!] = 0, \qquad [\![\varkappa_n(\xi_c)]\!] = 0, \qquad [\![\mathcal{M}_3(\xi_c)]\!] = 0, \tag{III.3.3}$$

where double brackets indicate the increment of the quantity across a discontinuity, *e.g.* $[\![\mathcal{F}(\xi_c)]\!] = \lim_{\partial\xi\to 0}(\mathcal{F}(\xi_c + \partial\xi) - \mathcal{F}(\xi_c - \partial\xi))$. The curvatures $\varkappa_g = \boldsymbol{\varkappa}\boldsymbol{n}\cdot(\boldsymbol{N}\times\boldsymbol{d}_3)$ and $\varkappa_n = \boldsymbol{\varkappa}\boldsymbol{n}\cdot\boldsymbol{N}$

are to be understood as the projections of the rod intrinsic curvature $\varkappa \boldsymbol{n}$ onto the geodesic and normal direction at the contact point and, therefore, generally differ from the definitions given in equations (III.1.13–III.1.18) in the context of continuous contacts. Additionally, the continuity of the director basis along the rod centerline and equations (III.3.3.c) ensure that $[\![\varkappa_t(\xi_c)]\!] = [\![\psi'(\xi_c)]\!] = 0$. Therefore, substituting (III.3.2–III.3.3) into equations (III.1.36–III.1.38) yields

$$[\![\alpha'(\xi_c)]\!] = \alpha\,\varkappa_n\,\eta^2\,\mathcal{R}, \tag{III.3.4}$$

$$[\![\varkappa_g'(\xi_c)]\!] = -\varkappa_g\,\varkappa_n\,\eta^2\,\mathcal{R}, \tag{III.3.5}$$

$$[\![\varkappa_n'(\xi_c)]\!] = -\left(1+\eta^2\,\kappa_n^2\right)\mathcal{R}, \tag{III.3.6}$$

which, for inextensible rods $\left(\eta \to 0, \alpha \to 1, \alpha' \to \eta^2 \mathcal{F}_3'\right)$, degenerates to

$$[\![\mathcal{F}_3'(\xi_c)]\!] = \varkappa_n\,\mathcal{R}, \tag{III.3.7}$$

$$[\![\varkappa_g'(\xi_c)]\!] = 0, \tag{III.3.8}$$

$$[\![\varkappa_n'(\xi_c)]\!] = -\mathcal{R}. \tag{III.3.9}$$

These expressions, which remain valid at the extremities of continuous contacts, emphasize that the first derivatives of the rod curvature and axial force possess finite jump discontinuities whose magnitude are proportional to the reaction force. One may conclude that contacts with order $n \geq 3$ are characterized by a zero reaction force and, therefore, mark the transition between contact and no contact.

III.3.3 From discrete to continuous contact

Equations (III.3.1) with $k = 0, 1$ constitute the necessary conditions for the rod to have a contact point with the constraint surface. They are however not sufficient to ensure the validity of the unilateral contact condition as the curvature of the rod centerline may be incompatible with the constraint surface local geometry. To be verified at a point contact, relation (III.1.10) indeed requires a contact of order $n \geq 2$. The normal curvature of a surface bound curve $\mathscr{E}$ being an extrinsic property of the surface $\mathscr{S}$ on which it lays, its magnitude is inevitably conditioned by the embedding of the surface in the ambient space and, by definition, ranges between the surface principal curvatures, see equation (III.1.21). As defined in equation (III.1.18), the normal curvature $\varkappa_n$ is positive if the surface bends towards its unit normal. Therefore, assuming the unit normal $\boldsymbol{N}$ to the constraint surface to be outward pointing for interior problems and inward pointing for exterior problems, the projection of the rod intrinsic curvature on the surface normal at a contact point must be smaller or equal to the surface normal curvature along the

rod centerline. That is

$$\varkappa \boldsymbol{n} \cdot \boldsymbol{N} \leq \varkappa_n, \tag{III.3.10}$$

where $\boldsymbol{n}$ is the unit normal to the space curve $\mathscr{E}$, see equation (II.1.4–II.1.5). Hence, this inequality is strictly satisfied at the transition from discrete to continuous contact and a discrete contact of order $n \geq 2$ is equivalent to a continuous contact of zero length. Note that, for a planar elastica inside a conduit of constant clearance, this criterion is equivalent to the results of Denoël and Detournay (2011) who showed that, for a contact to be discrete, the conduit wall curvature must be larger than the curvature of the contacting side of the rod.

III.4 Summary

Slender elastic rods are ubiquitous in nature and technology. For a vast majority of applications, the rod deflection is restricted by an external constraint and a significant part of the rod is in continuous contact with a constraining surface. To assess the influence of the constraint local geometry on the configuration of the rod centerline and the reaction pressure, the continuous contact between an elastic rod and a rigid surface has been investigated from a geometrical perspective. The equation governing the static equilibrium of elastic rods have been particularized to surface bound configurations by *(i)* specifying the location of the rod axis in terms of its coordinates in the parameter space associated with the constraint surface parameterization, and *(ii)* characterizing the orientation of the rod material frame through its rotation with respect to the surface normal. This formulation leads to an explicit representation of the rod centerline in which the strain variables, measuring the rod change of shape, are expressed in terms of the geometric invariants $(\kappa_g, \kappa_n, \tau_g)$. The resulting set of governing equations was additionally shown to properly degenerate into that of elastic curves by imposing zero twist and neglecting the stretch deformation, that is assuming the rod to be twist-free and inextensible.

Particularizing the Lagrangian description of surface bound rods to the continuous contact with normal ringed surfaces, an Eulerian formulation analogue to the one obtained in Section II.2 was then derived. Again, the restatement of the rod local equilibrium in terms of the Eulerian curvilinear coordinate is particularly appropriate to treat free boundary value problems that are subjected to self-feeding. The isoperimetric constraints that would otherwise ensue from a conventional Lagrangian formulation indeed vanish and the resolution reduces to that of a system of differential-algebraic equations associated with classical boundary conditions. As in Chapter II, this Eulerian formulation restricts the range of potential configurations adopted by the rod and prevents the appearance of parasitic solutions associated with curling or writhing. Similarly, this formulation reaches its limits with the single-valuedness of the mapping $S(s)$ and $s(S)$ which fail as a section along the constraint surface is crossed multiple times, *viz.* sections at which $\boldsymbol{d}_3 \cdot \boldsymbol{D}_3$ changes sign, or if the constraint self-intersects, *i.e.*, points where

$\boldsymbol{\mathcal{S}}_\xi \times \boldsymbol{\mathcal{S}}_\beta = \mathbf{0}$. Both situations are however avoided provided that $\epsilon\,(\mathcal{U}_2 \cos\beta - \mathcal{U}_1 \sin\beta) \geq 1$. Finally, degenerating this approach to a single point, the criterion governing the transition between discrete and continuous contacts.

As already emphasized, the physical interest of solutions associated with a normal reaction pressure of non-constant sign is limited. The rod would indeed leave the constraining surface where the pressure drops to zero and the solution computed with the proposed formulation ceases to be valid. More generally, global solutions for the applications mentioned in the introductory Chapter require the assemblage of finite pieces of solutions (with a reaction pressure of constant sign) of the constrained problem studied here with pieces of contact-free solutions investigated in Chapter II. This procedure is further investigated in the next Chapter.

"There is geometry in the humming of strings. There is music in the spacing of the spheres ".

Pythagoreas (5^{th} century BC)

Chapter IV

Computational Model

With the ambition to contribute to the modeling and understanding of real-world phenomena, the global objective of this thesis consists in the analysis of constrained elastic rod problems that involve both continuous contact and contact-free segments. Although these two elementary configurations have been investigated independently in Chapters II and III, their recombination towards the resolution of the complete problem has not been described yet. Focusing on the canonical problem defined in Section I.3.1, the methodology proposed in this work consists in partitioning the global problem in a sequence of rod segments either in continuous contact with the constraint or contact-free between their extremities. As emphasized in Chapter I, the nub of this segmentation strategy is the determination of the positions of the contacts between the rod and the constraint as well as the extent of these contacts. The methodology leading to the establishment of this contact pattern, essential to the resolution of the global problem, is detailed in this Chapter. Combining this segmentation strategy with the systematic resolution of the sequence of elementary problems, a computational model that solves the quasi-static deflection of an elastic rod constrained to deform inside or around a tube-like surface is formulated.

IV.1 Segmentation strategy

Conceptually the segmentation strategy is a very natural way to cope with complex problems involving multiple continuous and discrete contacts. By sequencing the global problem into elementary problems, comparatively simpler, one may resort to methods specifically designed to treat each type of elementary problem individually. The identification of the correct contact pattern, which ensures that the rod remains inside or outside the constraint and preserves the rod integrity along the global problem, however requires *(i)* the establishment of the number of contacts and their nature (either discrete or continuous), and *(ii)* the determination of the rod position, inclination and rotation angle at the connections between successive elementary problems. The identification of these features, which fully characterize the contact pattern, may

be systematized in an algorithm involving three nested loops. This strategy is conceptualized in Algorithm IV.1. The outer loop (ContactPatternSwitcher), concerned with the identification of the sequence of elementary problems satisfying the unilateral contact condition, establishes the number of contacts and their nature, that is either discrete or continuous. For a given sequence, the median loop (SolveSequence) determines the position and inclination of the connections that ascertain the continuity of the rod between elementary problems. This procedure requires the evaluation of the rod configuration along the global problem and, therefore, yield yet an additional loop (PropagateSolution) that resolves the sequence of the elementary problems. To ensure the correct transmission of the axial force and twisting moment, this resolution is conducted sequentially by propagating the solution from on extremity of the global problem to the other. The collocation method implemented to solve each elementary problem (SolveElmProb) is presented in the following Section. Then, starting from the inner loop and progressively working our way out, these procedures leading to the establishment of the correct contact pattern are investigated in the following Sections.

Algorithm IV.1 Resolution of the global problem through segmentation strategy

while wrong contact pattern **do** ▷ ContactPatternSwitcher
  modify contact pattern (add, delete, merge or split contacts)
  while not in equilibrium **do** ▷ SolveSequence
    adjust connections (position, inclination and rotation angle)
    loop on elementary problems ▷ PropagateSolution
      solve rod configuration ▷ SolveElmProb
    end loop
    check rod integrity at the connections
  end while
  check unilateral contact condition (penetration, positivity of the reactions, etc.)
end while
return rod configuration along the global problem

IV.1.1 Elementary problem (SolveElmProb)

Various numerical methods have been applied to two-point boundary value problems, see Ascher et al. (1995) and references therein. The so-called shooting method, which combines a root-finding algorithm and a high-order differential equation solver, has been frequently applied to the Lagrangian problem associated with rods of known length (van der Heijden et al., 2003; da Fonseca and de Aguiar, 2003; Li and Chen, 2014). Although this numerical technique has also been successfully extended to the Lagrangian free boundary value problem associated with a planar elastica and its Eulerian reformulation (Denoël and Detournay, 2011), a collocation

method was favored to treat the mixed order systems of nonlinear ordinary differential equations (II.2.48–II.2.53) and (III.2.30–III.2.35) associated with the boundary conditions (II.2.54–II.2.55) and (III.2.36–III.2.37), respectively.

Besides the recognized robustness and efficiency of collocation codes (Russell and Shampine, 1972; Ascher et al., 1979, 1981; Ascher and Spiteri, 1994), this choice is mainly motivated by the simplicity of the collocation procedure which makes its programming reasonably straightforward. While alternative methods often require the conversion of the problem to a first order system, the collocation maintains the algebraic structure of the discretized problem. Considering the relative complexity of the rod governing equations in the Eulerian framework, the collocation method presents a considerable advantage to reliably solve the boundary value problems under consideration. Due to the differences in their respective structures, we distinguish the contact-free and continuous contact configurations.

IV.1.1.1 Contact-free configuration

Defining a partition Π of the domain $[0,1]$ constituted of N subintervals, an approximate solution $\{\boldsymbol{\delta}^*, \varphi^*, \boldsymbol{\mathcal{F}}^*\}$ is formed as a linear combination of a suitable set of functions, the coefficients of which being determined by requiring the approximate solution to satisfy the boundary conditions (II.2.54–II.2.55) as well as the differential equations (II.2.48–II.2.53) at certain points (de Boor and Swartz, 1973). For reasons of efficiency, stability, and flexibility in order and continuity, B–splines are chosen as basis functions (Ascher et al., 1979) such that

$$\boldsymbol{\delta}^* \in \mathcal{P}_{k+3,\Pi} \cap C^2\,[0,1]\,, \tag{IV.1.1}$$

$$\varphi^* \in \mathcal{P}_{k+2,\Pi} \cap C^1\,[0,1]\,, \tag{IV.1.2}$$

$$\boldsymbol{\mathcal{F}}^* \in \mathcal{P}_{k+1,\Pi} \cap C^0\,[0,1]\,, \tag{IV.1.3}$$

where $k \geq 3$ is the number of collocation points per subinterval and $\mathcal{P}_{n,\Pi}$ is the set of all piecewise polynomial functions of order n on the partition Π. The differentiability class of the approximate solution components ensures the existence and continuity of their highest derivative entering the governing equations while the minimum number of collocation points is given by the highest differential order of the system.

In other words, over each of the N subintervals of the domain, the components of the eccentricity vector are approximated by B–splines (piecewise polynomial functions) of degree $k+3$. Accounting for the imposed C^2–continuity between intervals, the approximate solutions $\delta_i^\star$ $(i=1,2)$ are associated with $k\,N+3$ unknown coefficients, each. Similarly, to the approximate solutions $\varphi^\star$ for the rotation angle and $\mathcal{F}_j^\star$ $(j=1,2,3)$ for the components of the internal force, correspond $k\,N+2$ and $k\,N+1$ unknown coefficients, respectively, for a total of $6\,k\,N+11$ unknown coefficients. The value of 11 of these coefficients may readily be determined through the imposition of the 11 boundary conditions (II.2.54–II.2.55). The remaining $6\,k\,N$ unknown B–spline coefficients are determined by solving a system of $6\,k\,N$ nonlinear equations obtained

by collocating the governing equations (II.2.48–II.2.53) at k points on each subinterval of the domain.

IV.1.1.2 Continuous contact configuration

A similar method is applied to the system of differential-algebraic equations (III.2.30–III.2.35). For stability reasons, the prevailing approach to this general class of system of differential equations is however to eliminate the algebraic components of the system (Ascher and Spiteri, 1994). To this end, the normal component $\mathcal{F}_n$ of the internal force is isolated from equation (III.2.33) and substituted in the remaining equations of the system. Hence, an approximate solution $\left\{\beta^\star, \psi^\star, \mathcal{F}_g^\star, \mathcal{F}_3^\star\right\}$ satisfying

$$\beta^* \in \mathcal{P}_{k+3,\Pi} \cap C^2\left[0,1\right], \tag{IV.1.4}$$

$$\psi^* \in \mathcal{P}_{k+2,\Pi} \cap C^1\left[0,1\right], \tag{IV.1.5}$$

$$\mathcal{F}_g^*, \mathcal{F}_3^* \in \mathcal{P}_{k+1,\Pi} \cap C^0\left[0,1\right], \tag{IV.1.6}$$

is build by imposing the 7 boundary conditions (III.2.36–III.2.37) and solving a system of $4\,k\,N$ nonlinear equations obtained by collocating the governing equations (III.2.30, III.2.32, III.2.34–III.2.35) at k Gaussian points on each subinterval of the domain. The normal component $\mathcal{F}_n$ of the internal force and the algebraic component of the system, namely the reaction pressure ρ, are ulteriorly obtained from equations (III.2.33) and (III.2.31), respectively.

IV.1.1.3 Determination of the B–spline coefficients

In both contact-free and continuous contact configurations, the resolution of an elementary boundary value problem by collocation requires to identify the B–splines coefficients by solving a system of nonlinear equations. This procedure has been implemented in MATLAB by combining the *Spline Toolbox* (de Boor, 2005) to evaluate the B–splines and their derivatives with a backtracking line-search algorithm (Dennis and Schnabel, 1996) to solve the system of nonlinear collocation equations. This general procedure, outlined in Algorithm IV.2, is further described in the following.

Gathering the unknown B–spline coefficients in a vector $\mathbf{x}$, we denote by $\mathbf{F}\left(\mathbf{x}, \mathsf{BC}\right) = \mathbf{0}$ the system of nonlinear equations obtained by collocating the appropriate set of governing equations, that is either (II.2.48–II.2.53) or (III.2.30, III.2.32, III.2.34–III.2.35), and the corresponding boundary conditions BC, (II.2.54–II.2.55) or (III.2.36–III.2.37), respectively. We additionally define the associated Jacobian matrix $\mathbf{J}\left(\mathbf{x}\right)$ such that $\mathsf{J}_{ij} = \partial \mathsf{F}_i / \partial \mathsf{x}_j$. Although this matrix could theoretically be evaluated analytically, the present implementation relies on a finite difference scheme to approximate its non-zero elements.

Starting from and initial guess $\mathbf{x}^0$, the algorithm associates the Newton's method and a backtracking line-search strategy to guarantee some progress towards the solution at each iteration.

The basic idea of this globally convergent method is to ensure that the norm $\mathsf{f}\left(\mathbf{x}^i\right) = \frac{1}{2}\left\|\mathbf{F}\right\|^2$ sufficiently decreases at each iteration (Press et al., 2007, pp. 477–483). In practice, we require the average rate of decrease of $\mathsf{f}\left(\mathbf{x}^i\right)$ to be at least some fraction $c_1 \in [0, 1]$ of the initial rate of decrease $\nabla \mathsf{f}^i\,\mathbf{p}$, that is

$$\mathsf{f}\left(\mathbf{x}^i + \lambda\,\mathbf{p}\right) \leq \mathsf{f}\left(\mathbf{x}^i\right) + c_1\,\lambda\,\nabla \mathsf{f}^i\,\mathbf{p}, \tag{IV.1.7}$$

where $\mathbf{p} = -\mathbf{J}\,\mathbf{F}$ is the Newton step for the set of equations $\mathbf{F}\left(\mathbf{x}^i, \mathsf{BC}\right) = \mathbf{0}$ and $\nabla \mathsf{f}^i\,\mathbf{p} = \mathbf{F}\,\mathbf{J}\,\mathbf{p} < 0$ is a descent direction for $\mathsf{f}\left(\mathbf{x}^i\right)$. The common procedure is to try the full Newton step and, if $\lambda = 1$ fails to satisfy criterion (IV.1.7), to backtrack along the direction defined by this step until an acceptable point is found. A relatively efficient strategy consists in using a polynomial interpolation to estimate the location of the minimum of $\mathsf{m}\left(\lambda\right) = \mathsf{f}\left(\mathbf{x}^i + \lambda\,\mathbf{p}\right)$. Knowing $\mathsf{f}\left(\mathbf{x}^i\right)$, $\nabla \mathsf{f}^i\,\mathbf{p}$ and $\mathsf{f}\left(\boldsymbol{x}^i + \mathbf{p}\right)$ at the end of the first step, a new step size $\hat{\lambda}$ minimizing the quadratic approximation of $\mathsf{m}\left(\lambda\right)$ is computed. It can be shown that, since the Newton step failed, this new step size satisfies $0 < \hat{\lambda} \lesssim 1/2$ for small c_1 (Dennis and Schnabel, 1996, pp. 126–129); in the current implementation $c_1 = 10^{-4}$. For the subsequent steps, the preceding trial step $(\lambda_s, \mathsf{m}(\lambda_s))$ is stored and a cubic approximation of $\mathsf{m}\left(\lambda\right)$ may be used to locate its minimum (MinCubic). The step size selection Algorithm IV.3 further ensures that $\hat{\lambda}$ lies between $\lambda_s/10$ and $\lambda_s/2$.

Algorithm IV.2 Resolution of an elementary problem

Description: Given the boundary conditions BC of the elementary problem and an initial guess $\mathbf{x}^0$ for the B–spline coefficients of the approximate solution, finds the root of $\mathbf{F}\left(\mathbf{x}, \mathsf{BC}\right)$ by a globally convergent method.

procedure SolveElmProb($\mathbf{x}^0, \mathsf{BC}$)
  $i \leftarrow 0$
  while not converged **do**
    $\mathbf{F} \leftarrow \mathbf{F}\left(\mathbf{x}^i, \mathsf{BC}\right)$ ▷ collocation of the governing equations and BC
    $\mathbf{J} \leftarrow$ JacobianMatrix $\left(\mathbf{x}^i, \mathsf{BC}\right)$ ▷ finite difference
    $\mathbf{p} \leftarrow -\mathbf{J}\,\mathbf{F}, \nabla \mathsf{f}^i \leftarrow \mathbf{F}\,\mathbf{J}$
    $\lambda \leftarrow$ StepSize$\left(\mathbf{x}^i, \mathbf{p}, \nabla \mathsf{f}^i\right)$ ▷ see Algorithm IV.3
    $\mathbf{x}^{i+1} \leftarrow \mathbf{x}^i + \lambda\,\mathbf{p}, i \leftarrow i + 1$
  end while
  return $\mathbf{x}^i$ ▷ rod configuration along the elementary problem
end procedure

The termination criterion of this procedure determines if a suitable $\mathbf{x}^i$ was found at the end of the current iteration. Due to the inherent finite-precision of numerical algorithms, only an approximate solution to the system $\mathbf{F}\left(\mathbf{x}\right) = 0$ may possibly be found. Practically, to prevent

Algorithm IV.3 Step size selection for the backtracking line-search algorithm

Description: Given a point $\mathbf{x}$, the gradient $\nabla \mathsf{f}_0$ of a function $\mathsf{f}(\mathbf{x})$ at this point, and a direction $\mathbf{p}$, finds a step size along $\mathbf{p}$ from $\mathbf{x}$ that *sufficiently* decreases the function $\mathsf{f}(\mathbf{x})$.

1: **procedure** StepSize($\mathbf{x}, \mathbf{p}, \nabla \mathsf{f}_0$)
2: $\quad \mathsf{f}_0 \leftarrow \mathsf{f}(\mathbf{x}), \lambda \leftarrow 1$ ▷ start with a Newton step
3: $\quad$ **while** $\lambda \geq \lambda_{min}$ **do**
4: $\quad\quad \mathsf{f}_\lambda \leftarrow \mathsf{f}(\mathbf{x} + \lambda \mathbf{p})$
5: $\quad\quad$ **if** $\mathsf{f}_\lambda \leq \mathsf{f}_0 + c_1 \lambda \nabla \mathsf{f}_0$ **then**
6: $\quad\quad\quad$ **return** λ ▷ sucessful search
7: $\quad\quad$ **else**
8: $\quad\quad\quad$ **if** $\lambda = 1$ **then**
9: $\quad\quad\quad\quad \lambda_{tmp} \leftarrow -\nabla \mathsf{f}_0 / 2 (\mathsf{f}_\lambda - \mathsf{f}_0 - \nabla \mathsf{f}_0)$ ▷ first backtrack
10: $\quad\quad\quad$ **else**
11: $\quad\quad\quad\quad \lambda_{tmp} \leftarrow$ MinCubic($\mathsf{f}_0, \nabla \mathsf{f}_0, \lambda, \mathsf{f}_\lambda, \lambda_s, \mathsf{f}_s$) ▷ subsequent backtrack
12: $\quad\quad\quad$ **end if**
13: $\quad\quad\quad \lambda_s \leftarrow \lambda, \mathsf{f}_s \leftarrow \mathsf{f}_\lambda, \lambda \leftarrow \max(\lambda/10, \min(\lambda/2, \lambda_{tmp}))$
14: $\quad\quad$ **end if**
15: $\quad$ **end while**
16: $\quad$ **return** λ_{min} ▷ failed search
17: **end procedure**

divergent iterations to run endlessly, a maximum number of iterations `i_max` is fixed. Additionally, the decision on wether to stop or not the procedure at the end of the current iteration may be based on the absolute residual $\left\|\mathbf{F}\left(\mathbf{x}^i\right)\right\| \leq$ `tol_Fn` and on the relative change of the solution $\left\|\mathbf{x}^{i+1} - \mathbf{x}^i\right\| / \left\|\mathbf{x}^i\right\| \leq$ `tol_step`, which is not sensitive to the characteristic size of $\mathbf{x}$. The convergence of the algorithm towards the solution is however not guaranteed. This procedure may indeed fail at solving the elementary problem if the initial guess $\mathbf{x}^0$ is chosen close to a local minimizer of $\mathsf{f}(\mathbf{x})$ that is not a root of $\mathbf{F}(\mathbf{x})$. When facing such a situation, a simple strategy consists in providing a new initial guess that is closer to the root of $\mathbf{F}(\mathbf{x})$, if possible. This situation is however infrequent in practice as, whenever possible, a continuation method is used to "educate" the guess $\mathbf{x}^0$ through the incremental loading of the structure.

IV.1.2 Propagation of the solution (PropagateSolution)

As defined in Section I.3.1, the global boundary value problem prescribes the rod position and inclination with respect to the reference curve at its extremities although the rod length is unknown. In terms of standard support conditions, one extremity of the rod is clamped while the other may be seen as moving freely through a frictionless sliding sleeve under the combined action of known axial force and twisting moment. Recasting these boundary conditions in the Eulerian framework, the global problem that spans the constraint axis between $S = 0$ and $S = L$

is subjected to global boundary conditions BC^{G} of the form (II.2.54–II.2.55), *viz.*

$$\{\varphi(0), \Delta_i(0), \Delta_i'(0)\}, \qquad \{\alpha(L), \varphi'(L), \Delta_i(L), \Delta_i'(L)\}, \tag{IV.1.8}$$

with $i = 1, 2$. Assuming a contact pattern of n elementary problems and the associated position $\Delta_i(S_k)$, inclination $\Delta_i'(S_k)$ and rotation angle $\varphi(S_k)$ at the connexions S_k $(k = 1, \ldots, n-1)$, the evaluation of the rod configuration along the global problem may be organized sequentially by propagating the solution from one extremity to the other. The determination of these features of the contact pattern is the central concern of the procedure SolveSequence that is described in the following Section. Denoting by Elm_k the elementary problem with domain $S \in [S_{k-1}, S_k]$ and boundary conditions BC^k

$$\{\varphi(S_{k-1}), \Delta_i(S_{k-1}), \Delta_i'(S_{k-1})\}, \qquad \{\alpha(S_k), \varphi'(S_k), \Delta_i(S_k), \Delta_i'(S_k)\}, \tag{IV.1.9}$$

with $k = 1, \ldots, n$ and $0 = S_0 < \cdots < S_k < \cdots < S_n = L$, the resolution of the sequence starts with the evaluation of the rod configuration along the elementary problem Elm_n. Both the stretch $\alpha(L)$ and twist $\varphi'(L)$at its extremity $S_n = L$ resulting from the global boundary conditions (IV.1.8), this boundary value problem is well defined and can be solved. The stretch $\alpha(S_{n-1})$ and twist $\varphi'(S_{n-1})$ at its extremity S_{n-1} may then be evaluated and transmitted to the boundary condition of Elm_{n-1}, which in turn yields the values of these quantities at its origin. Hence, the set of elementary problem may be resolved sequentially by propagating the solution from Elm_n to Elm_1. This procedure is conceptualized in Algorithm IV.4.

The $n-1$ connections resulting from the segmentation of the global problem are either discrete contacts or extremities of continuous contacts and, therefore, correspond to points at which the rod contacts the constraint surface. At these points, the tangency condition requires that the components of the eccentricity vector satisfy

$$\Delta_1(S_k) = Q\cos\beta, \qquad \Delta_1'(S_k) = Q'\cos\beta - \beta' Q\sin\beta, \tag{IV.1.10}$$

$$\Delta_2(S_k) = Q\sin\beta, \qquad \Delta_2'(S_k) = Q'\sin\beta + \beta' Q\cos\beta, \tag{IV.1.11}$$

where $Q(S)$ is the known radius function of the constraint surface. Additionally, the rotation of the rod cross section about the director $\boldsymbol{d}_3$ may equivalently be identified through its rotation with respect to the intermediate $\{\boldsymbol{k}_j\}$–basis or with respect to the normal and geodesic directions at this point of the constraint surface, that is in terms of either $\varphi(S_k)$ or $\psi(S_k)$. The definitions (II.2.10–II.2.11) and (III.2.9–III.2.10) of these angles indeed lead to the relations

$$\cos\psi = -\sin\varphi\,\boldsymbol{k}_1\cdot\boldsymbol{N} + \cos\varphi\,\boldsymbol{k}_2\cdot\boldsymbol{N}, \tag{IV.1.12}$$

$$\sin\psi = \cos\varphi\,\boldsymbol{k}_1\cdot\boldsymbol{N} + \cos\varphi\,\boldsymbol{k}_2\cdot\boldsymbol{N}, \tag{IV.1.13}$$

while equations (II.2.19) and (III.1.25) for the twist density yield

$$\psi' = \varphi' + J_1^{-1}\left(\widetilde{w}_3 - \alpha\,\tau_g\right). \tag{IV.1.14}$$

Hence, for elementary problems corresponding to rod segments in continuous contact with the constraint, the boundary conditions (IV.1.9) may easily be re-expressed in a form similar to (III.2.36–III.2.37) that involves the polar angle β and the rotation angle ψ rather than the components of the eccentricity vector Δ_1, Δ_2 and the rotation angle φ. Accounting for the known magnitude of the eccentricity vector at the connections, it will be convenient to use

$$\left\{\varphi_{k-1}, \beta_{k-1}, \beta'_{k-1}\right\}, \qquad \left\{\alpha_k, \varphi'_k, \beta_k, \beta'_k\right\}, \tag{IV.1.15}$$

as a shorthand for the elementary boundary conditions (IV.1.9).

Algorithm IV.4 Propagation of the solution along the sequence of elementary problems

Description: Given the global boundary conditions BC^{G}, and the rod position, inclination and rotation angle at the connections $\mathbf{y} = \{S_k, \varphi_k, \beta_k, \beta'_k\}$ with $k = 1, \ldots, n-1$, propagates the resolution of elementary problems along the global problem.

1: **procedure** PROPAGATESOLUTION($\mathbf{y}, \mathsf{BC}^{\mathsf{G}}$)
2: deduce BC^n from $\mathbf{y}$ and BC^{G}
3: provide initial guess $\mathbf{x}_0^n$ for the solution of Elm^n
4: $\mathbf{x}^n \leftarrow$ SOLVEELMPROB($\mathbf{x}_0^n, \mathsf{BC}^n$)
5: **for** $k = n-1 \rightarrow 2$ **do**
6: deduce BC^k from $\mathbf{y}$ and $\mathbf{x}^{k+1}$ ▷ see equation (IV.1.9)
7: provide initial guess $\mathbf{x}_0^k$ for the solution of Elm^k
8: $\mathbf{x}^k \leftarrow$ SOLVEELMPROB$\left(\mathbf{x}_0^k, \mathsf{BC}^k\right)$ ▷ see Algorithm IV.2
9: **end for**
10: deduce BC^1 from BC^{G} and $\mathbf{x}^2$
11: provide initial guess $\mathbf{x}_0^1$ for the solution of Elm^1
12: $\mathbf{x}^1 \leftarrow$ SOLVEELMPROB$\left(\mathbf{x}_0^1, \mathsf{BC}^1\right)$
13: **return** $\mathbf{X} \leftarrow \left\{\mathbf{x}^1, \ldots, \mathbf{x}^n\right\}$ ▷ rod configuration along each Elm
14: **end procedure**

IV.1.3 Continuity of the sequence (SOLVESEQUENCE)

Although the clamped-sliding sleeve boundary conditions (IV.1.9) imposed at each elementary problem guarantee the continuity of both the space curve $\mathscr{E}$ and its tangent, the rod curvature and, therefore, the bending moment may present jump discontinuities at these connections. In the absence of concentrated body couple or other singularities at the connections, these

discontinuities are however not physical. Similarly, the boundary conditions (IV.1.9) fail to maintain a smoothness of the rotation angle φ sufficient to ensure the continuity of the directors $\{\boldsymbol{d}_j\}$ along the rod. Finally, while the propagation of the axial force and twisting moment from one extremity of the global problem to the other assure the continuity of these internal efforts, the component F_g of the shear force may also present unrealistic jump discontinuities at these connections. The median loop, which is concerned with the determination of the rod position $\beta(S_k)$, inclination $\beta'(S_k)$ and rotation angle $\varphi(S_k)$ at the connections, reestablishes the integrity of the rod between elementary problems.

The role of this procedure is therefore to identify the $4(n-1)$ quantities

$$\{S_k, \varphi_k, \beta_k, \beta'_k\}, \qquad k = 1, \dots, n-1, \tag{IV.1.16}$$

entering the boundary conditions (IV.1.15) that ensure the rod integrity along the global problem, *viz.* satisfying the $4(n-1)$ equations

$$[\![\varphi(S_k)]\!] = 0, \qquad [\![\kappa_g(S_k)]\!] = 0, \qquad [\![\kappa_n(S_k)]\!] = 0, \qquad [\![F_g(S_k)]\!] = 0. \tag{IV.1.17}$$

Note that, according to equations (III.3.8–III.3.9), the curvatures derivatives need not to be continuous at these connections. Generally, this nonlinear system of equations cannot be solved analytically (*e.g.* based on symmetry arguments) and one must resort to a root-finding algorithm.

The method adopted for the applications presented in this thesis is inspired by the backtracking line-search algorithm described in Section IV.1.1.3 for the resolution of the elementary problems. Gathering the $4(n-1)$ unknowns (IV.1.16) in a vector $\mathbf{y}$, we denote by $\mathbf{G}(\mathbf{X}|\mathbf{y}) = \mathbf{0}$ the system of nonlinear equations (IV.1.17) obtained by propagating the resolution of the elementary problems according to the procedure detailed in Section IV.1.2. The Jacobian matrix $\mathbf{J}(\mathbf{X}|\mathbf{y})$ associated with this system and defined such that $\mathsf{J}_{ij} = \partial \mathsf{G}_i / \partial \mathsf{y}_j$ is again approximated by finite difference. Starting from and initial guess $\mathbf{y}^0$, the algorithm ensures that the norm $\mathsf{g}(\mathbf{X}|\mathbf{y}) = \frac{1}{2}\|\mathbf{G}\|^2$ sufficiently decreases at each iteration according to the criterion

$$\mathsf{g}\left(\mathbf{X}|\mathbf{y}^i + \lambda\,\mathbf{p}\right) \leq \mathsf{g}\left(\mathbf{X}|\mathbf{y}^i\right) + c_2\,\lambda\,\nabla\mathsf{g}^i\,\mathbf{p}, \tag{IV.1.18}$$

where $c_2 \in [0,1]$, $\mathbf{p} = -\mathbf{J}\,\mathbf{G}$ is the Newton step for the set of equations $\mathbf{G}\left(\mathbf{X}|\mathbf{y}^i\right) = \mathbf{0}$ and $\nabla\mathsf{g}^i\,\mathbf{p} = \mathbf{G}\,\mathbf{J}\,\mathbf{p} < 0$ is a descent direction for $\mathsf{g}\left(\mathbf{X}|\mathbf{y}^i\right)$. This procedure is outlined in Algorithm IV.5.

As in Section IV.1.1.3, the termination criterion of this procedure determines if a suitable $\mathbf{y}^i$ was found at the end of the current iteration. Similarly, a maximum number of iterations `i_max` is fixed and the stopping decision relies on the absolute residual $\left\|\mathbf{G}\left(\mathbf{X}|\mathbf{y}^i\right)\right\| \leq$ `tol_Gn` as well as the relative change of the solution $\left\|\mathbf{y}^{i+1} - \mathbf{y}^i\right\| / \left\|\mathbf{y}^i\right\| \leq$ `tol_step`. Again, the convergence towards the solution is not guaranteed for all $\mathbf{y}^0$.

Algorithm IV.5 Resolution of the sequence of elementary problems

Description: Given an initial guess $\mathbf{y}^0$ for the rod position, inclination and rotation angle at the connections, finds the root of $\mathbf{G}(\mathbf{X}|\mathbf{y})$ by a globally convergent method.

procedure SolveSequence($\mathbf{y}^0$)
  $i \leftarrow 0$
  while not converged **do**
    $\mathbf{X} \leftarrow$ PropagateSolution$\left(\mathbf{y}^i, \mathsf{BC}^{\mathsf{G}}\right)$ ▷ see Algorithm IV.4
    $\mathbf{G} \leftarrow \mathbf{G}\left(\mathbf{X}|\mathbf{y}^i\right)$ ▷ see equation (IV.1.17)
    $\mathbf{J} \leftarrow$ JacobianMatrix $\left(\mathbf{y}^i\right)$ ▷ finite difference
    $\mathbf{p} \leftarrow -\mathbf{J}\,\mathbf{G}, \nabla \mathsf{g}^i \leftarrow \mathbf{G}\,\mathbf{J}$
    $\lambda \leftarrow$ StepSize$\left(\mathbf{y}^i, \mathbf{p}, \nabla \mathsf{g}^i\right)$ ▷ see Algorithm IV.3
    $\mathbf{y}^{i+1} \leftarrow \mathbf{y}^i + \lambda\,\mathbf{p}, i \leftarrow i+1$
  end while
  return $\mathbf{y}^i, \mathbf{X}$ ▷ rod configuration along each Elm, preserving its continuity
end procedure

IV.1.4 Number and nature of contacts (ContactPatternSwitcher)

Although, for some idealistic problems, one may imagine to test every (reasonable) sequence of elementary problems, this approach is certainly not efficient nor realistic in most circumstances. In this Section we propose to establish a pragmatic procedure leading to the identification of the correct contact pattern, *viz.* that satisfies the unilateral contact condition. The crux of this procedure is that it cannot be cast in a conventional form involving a finite set of unknowns and objective functions that must be minimized or zeroed. One must instead establish a collection of verifications that, once demonstrated true, ensure the correctness of the contact pattern. Based on a diagnostic of the configuration, each unsatisfied verification must additionally be associated with measures that secure the convergence towards the correct contact pattern.

The verification of the contact pattern is twofold. Firstly, the non-penetration condition requires that, for interior (resp. exterior) problems, new contacts be created whenever the magnitude $\Delta = \sqrt{\Delta_1^2 + \Delta_2^2}$ of the eccentricity vector exceeds (resp. is inferior to) the radius Q of the constraint, while the rod curvature at existing discrete contacts complies with the constraint local geometry. Secondly, reaction forces at discrete contacts and reaction pressures along continuous contacts must not be tensile. As schematized in Figure IV.1.1, these verifications are associated with three fundamental operations: the creation and elimination of discrete contacts, and the conversion between different types of contacts.

In practice, due to the finite precision of the numerical scheme, the establishment of this theoretically unique contact pattern is idealistic and one must generally settle for an *acceptable* one, that is within a certain tolerance. This deviation from the actual contact pattern is attributable to diverse origins. For instance, in Sections IV.1.1, it has been emphasized that the rod governing equations are not precisely satisfied and only an approximate solution of the rod

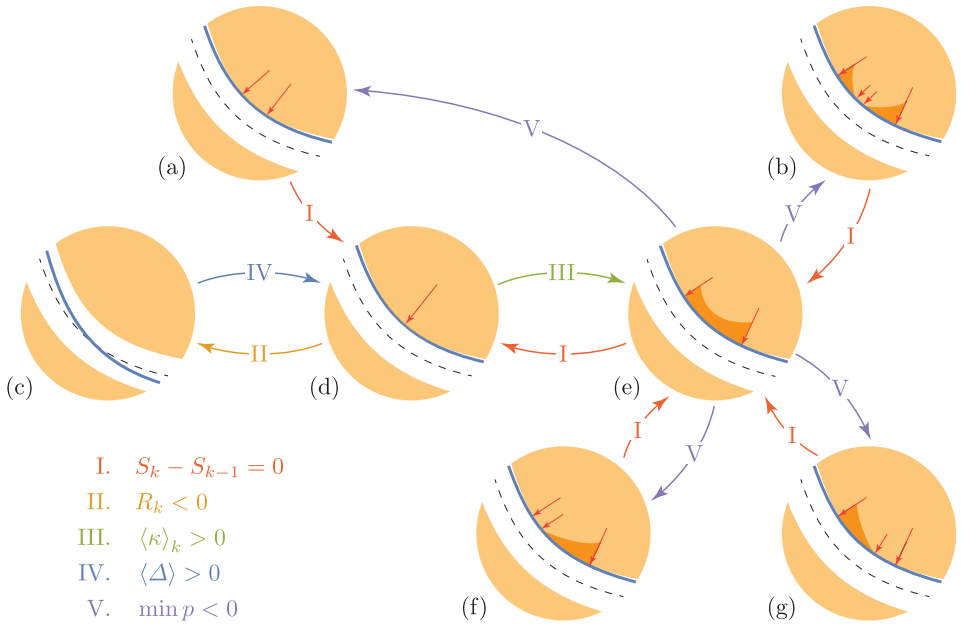

Figure IV.1.1: Fundamental operations associated with the contact pattern switcher: the creation and elimination of discrete contacts, and the conversion between different types of contacts

configuration can be obtained along each elementary problem. Similarly, the rod configuration at the connections, determined through the procedure described in Section IV.1.3, do not exactly ensure the rod integrity at these sections but rather guarantee that the discontinuities remain sufficiently small. These approximations reverberate through the estimation of the reaction forces and pressures, the evaluation of the rod curvature, the magnitude of the eccentricity vector and, therefore, to the subsequent verification of the unilateral contact condition. As already emphasized, further simplifications of the governing equations, such as the small inclination approximation presented in Section II.2.4, introduce additional inaccuracies on the detection of emerging contacts or the distinction between continuous and discrete contacts. Also, elementary problems whose shortness may lead to instabilities of the numerical scheme should be identified and removed from the sequence, hence contributing to the general inexactitude of the contact pattern. These approximations are however expected to have a limited impact on the global behavior of the rod and to marginally modify the nature of the solution. These aspects of the problem have been discussed more rigorously by Denoël and Detournay (2011) in the context of a planar elastica constrained to deform inside a sinuous conduit.

In contrast with the propagation of the solution along the global problem, this verification is not organized sequentially and, instead, is conducted iteratively by progressively adjusting the contact pattern. Drastic modifications could indeed fail to converge to the correct contact

pattern or cause instabilities of the numerical scheme. Also, for evolutive problems, events leading to the modification of the contact pattern are expected to rarely arise simultaneously such that, in general, none or only a few iterations are required between each loading step.

I. Length $S_k - S_{k-1}$ Sweeping through each elementary problem, the procedure starts with the suppression of every elementary problem that is considered to short, that is such that

$$\frac{S_k - S_{k-1}}{L} \leq \texttt{tol\_span}. \tag{IV.1.19}$$

Irrespectively of the nature of the elementary problem under consideration, this operation consists in merging the connections at its extremities; if the adjoining elementary problems are both in continuous contact with the constraint, they should however be combined in one sole elementary problem. In Figure IV.1.1, this operation is indicated by the arrows marked I. It is assumed that removing these elementary problems does not profoundly affect the global pattern and, therefore, proceed with the verification. In the meantime, depending on the nature of elementary problem under consideration and if its span does not satisfy inequality (IV.1.19), the magnitude of the eccentricity vector or the reaction pressure is evaluated and their respective extrema stored. Similarly, the reaction force and the rod curvature are recorded at its extremities.

II. Reaction R_k The verification proceeds then with the identification of the lowest reaction force R_{min} and, be it tensile, the suppression of the corresponding connection by merging the adjacent contact-free elementary problems, see Figure IV.1.1 transition II. This operation terminates the current iteration and the subsequent verifications are by-passed, the rod configuration along the resulting sequence of elementary is evaluated and the verification process re-initiated.

III. Curvature compatibility $\langle\kappa\rangle_k$ If no such connection is however diagnosed, the rod curvature (relative) compatibility

$$\langle\kappa\rangle_k = Q\left(\kappa\,\boldsymbol{n}\cdot\boldsymbol{N} - \kappa_n\right), \tag{IV.1.20}$$

is evaluated at every discrete contacts, that is according to equation III.3.10, and the most critical contact with $\langle\kappa\rangle_{\max}$ identified. If this quantity exceeds the tolerance `tol_curv`, the discrete contact is converted into a continuous one (transition III in Figure IV.1.1) and the procedure re-initiated with the new contact pattern.

IV. Penetration $\langle \Delta \rangle$ Provided both previous verifications do not require a modification of the contact pattern, the section associated with the highest relative penetration

$$\langle \Delta \rangle = \pm \frac{\Delta - Q}{Q}, \tag{IV.1.21}$$

is identified. The sign of the relative penetration depends on the nature of the problem, we define this quantity such that it is positive for interior problem and negative for exterior ones. While, within the Lagrangian framework, this task would require the comparison of two curves parameterized by distinct curvilinear coordinates (*i.e.*, the constraint axis and the rod centerline), it is trivialized by the Eulerian formulation. If $\langle \Delta \rangle_{max} \geq$ `tol_pene`, the corresponding elementary problem is split by creating a discrete contact at this critical section (transition IV in Figure IV.1.1); hence, terminating the verification and requiring the evaluation of the rod configuration along the new sequence.

V. Reaction pressure p Alternatively, in the absence of such penetration, one must eventually ensure that the reaction pressure remains positive, *i.e.*, compressive, along each continuous contact. The elementary problem associated with the lowest negative reaction pressure $p_{\min}$ is therefore identified and, depending on its profile, replaced by a contact-free elementary problem, split into two continuous contact delimiting a contact-free elementary problem, or in a continuous contact and a discrete contact. In Figure IV.1.1, these transitions are marked V. If none of these verifications leads to a modification of the contact pattern, the procedure is terminated and the correct contact pattern established. This procedure is outlined in Algorithm IV.6.

IV.1.5 Summary

The numerical scheme obtained by combining the procedures described in Sections IV.1.1 to IV.1.4 solve the quasi-static deflection of an elastic rod constrained inside or around a perfectly stiff, frictionless, normal ringed surface. The main objective of this computational model is to identify the contact pattern (*i.e.*, the number of contacts and their nature, the rod configuration at the connections) that satisfies the unilateral contact condition and preserves the rod integrity along the sequence of elementary problems. To establish this *map of the contacts* along the global problem, the procedure is systematized in an algorithm that involves three nested loops. Assuming a contact pattern and the associated rod configuration at the connections, the inner loop propagates the resolution of elementary problems along the sequence, from one extremity to the other. The median loop then restores the rod continuity at the connections by adjusting the position and inclination of the connections. Eventually, the outer loop ensures that the unilateral contact condition is respected along the global problem and, if required, modifies the contact pattern. These procedures heavily rely on the resolution of the rod configuration along each elementary problem and the assessment of the non-penetration. Both have been drastically simplified through the reformulation of the elementary problems within the Eulerian

Algorithm IV.6 Identification of the correct contact pattern

Description: Given an assumed contact pattern and an initial guess $\mathbf{y}^0$ for the rod position, inclination and rotation angle at the connections, establishes the contact pattern that satisfies the unilateral contact condition.

1: **procedure** ContactPatternSwitcher($\mathbf{y}^0$)
2: **while** wrong contact pattern **do**
3: $\mathbf{y}, \mathbf{X} \leftarrow$ SolveSequence$\left(\mathbf{y}^0\right)$ ▷ get rod configuration
4: **for** $k = 1 \rightarrow n$ **do**
5: **if** $\left(S_k - S_{k-1}\right)/L \leq$ `tol_span` **then**
6: $\mathbf{y}^0 \leftarrow$ remove Elm^k ▷ Figure IV.1.1(a) → (d),(a,b,f,g) → (e)
7: **else**
8: $\left[\langle \Delta \rangle_k, p_k\right] \leftarrow$ TestElmProb$\left(\mathsf{Elm}^k\right)$
9: $\left[R_k, \langle \kappa \rangle_k\right] \leftarrow$ TestConnection$\left(\mathsf{Elm}^k\right)$
10: **end if**
11: **end for**
12: $\langle \Delta \rangle_{max} \leftarrow \max \langle \Delta \rangle_k, p_{min} \leftarrow \min p_k$
13: $R_{min} \leftarrow \min R_k, \langle \kappa \rangle_{max} \leftarrow \max \langle \kappa \rangle_k$
14: **if** $L^2 R_{min}/B \leq$ `tol_reac` **then**
15: $\mathbf{y}^0 \leftarrow$ remove discrete contact ▷ Figure IV.1.1(d) → (c)
16: **else if** $\langle \kappa \rangle_{max} \geq$ `tol_curv` **then**
17: $\mathbf{y}^0 \leftarrow$ convert conection to continuous contact ▷ Figure IV.1.1(d) → (e)
18: **else if** $\langle \Delta \rangle_{max} \geq$ `tol_pene` **then**
19: $\mathbf{y}^0 \leftarrow$ add a discrete contact ▷ Figure IV.1.1(c) → (d)
20: **else if** $L^3 p_{min}/B \leq$ `tol_reac` **then**
21: $\mathbf{y}^0 \leftarrow$ split continuous contact ▷ Figure IV.1.1(e) → (a,b,f,g)
22: **end if**
23: **end while**
24: **end procedure**

framework associated with the constraint surface, which eliminates the isoperimetric constraints and trivializes the detection of new contacts.

The approach that is proposed in this thesis to establish the correct contact pattern is unfortunately not guaranteed to converge. Additionally, it requires to fine tune the tolerance involved in each loop and, especially, the verification of the contact pattern. As shown in the following Sections, this approach however proves to be fairly conclusive for reasonably complex contact patterns. The resulting approximate solutions further demonstrated a relatively low dependence on these tolerances.

Finally, both the resolution of the elementary problems (SolveElmProb) and the verification of the contact pattern (ContactPatternSwitcher) require the knowledge of the constraint surface geometry along the global problem, *viz.* the components $U_j(S)$ of the Darboux vector $\boldsymbol{U}$ and the radius function $Q(S)$. In the absence of analytical expressions, these quantities may approximated by piecewise polynomial functions. To ensure the existence and continuity of their highest derivative entering the governing equations and, therefore, a sufficient smoothness of the approximate solution, these approximation must satisfy

$$\boldsymbol{U}^\star \in \mathcal{P}_{k+2,\Omega} \cap C^1[0,L], \tag{IV.1.22}$$

$$Q^\star \in \mathcal{P}_{k+3,\Omega} \cap C^2[0,L], \tag{IV.1.23}$$

where Ω is a partition of the global domain $[0,L]$ and $k \geq \bar{k}$ with $\bar{k}$ the largest number of collocation points used in the resolution of the elementary problems.

IV.2 Illustration

To illustrate this computational model, we propose to further investigate the progressive buckling of an elastic rod constrained inside a helical conduit whose response has been initiated in Section II.3.3. The constraint consists in the canal surface defined by its helical axis, with pitch angle $\Theta = \pi/4$ and radius $\Sigma = R/L = \left(\pi\sqrt{2}\right)^{-1}$, and constant radius $\epsilon = Q/L$ where the length $L = \pi R/\sin\Theta$ of the problem under consideration corresponds to a half helical turn. Although axially unconstrained, *i.e.*, free to flow in/out of the conduit, the rod is assumed to be transversally clamped on the conduit axis at both extremities and subjected to an end torque $\mathcal{M}_3(1) = -1$ and axial force $\mathcal{F}_3(1) = \mathcal{T}$. With $\eta = 1/20$ and $\nu = 1/3$ and for two radii $\epsilon = 1/40$ and $1/20$, we analyze the rod behavior as the axial force $\mathcal{T}$ is varied from $\mathcal{T}_0 = -7.069$ that corresponds to a helical deformation centered on the constraint axis, see equation (II.3.19).

Maintaining the torque $\mathcal{M}_3$ constant, the magnitude of the end force $\mathcal{T}$ is progressively increased causing the rod to gradually leave the constraint axis and, eventually, contact the constraint. The earliest steps of the loading, corresponding to the contact-free rod and the rod contacting the constraint at one point, have been detailed in Section II.3.3. This Section ends as, at the discrete contact, the projection of the rod curvature on the unit normal to the

constraint reaches the surface normal curvature. At this stage of the loading, further increasing the magnitude of the end force $\mathcal{T}$ would indeed lead to a violation of the unilateral contact condition unless the discrete contact is replaced by a continuous contact. This forthcoming stage is analyzed in this Section.

Figure IV.2.1, which extends the result presented in Figure II.3.2, depicts the evolution of the unstretched length ℓ/L, the magnitude of the reaction forces $\mathcal{R}, \mathcal{R}_{l,r}$, and the scaled contact length L_c/L as the axial force $\mathcal{T}$ is varied. As the first derivatives of the geodesic and normal curvatures at the extremities of the continuous contact are not continuous, the reaction pressure is supplemented by two concentrated reaction forces $\mathcal{R}_l$ and $\mathcal{R}_r$. Due to the symmetry of the problem under consideration these forces remain equal. At the transition between discrete and continuous contact, marked by rhombuses, the length of the continuous contact is null and the magnitude of these forces is half that of the concentrated reaction prior to the transition. As the magnitude of the end force increases, these forces and the contact length L_c progressively grow. Various intermediate configurations for $\epsilon = 1/40$ are pictured in Figures IV.2.2 and IV.2.3.

For $\epsilon = 1/20$, as the end force reach $\mathcal{T} = -24.37\,|\mathcal{T}_0|$, the reaction pressure along the central element becomes locally outward pointing (*i.e.*, positive) and this element must therefore be split to allow for the central part of the rod to leave the constraint. This configuration is pictured in Figure IV.2.4. As the magnitude of the end force is further increased, the length of this contact-free element progressively grows.

Note that the oscillations observed in the deformed configuration presented in Figures IV.2.3(b) and IV.2.4 are typical of the buckled configurations experienced by oilfield tubulars and emphasized experimentally for horizontal cylindrical constraint (Su et al., 2013; Miller et al., 2015).

"Children and scientists share an outlook on life. 'If I do this, what will happen?' is both the motto of the child at play and the defining refrain of the physical scientist. [...] The unfamiliar and the strange – these are the domain of all children and scientists".

Gleick (2011)

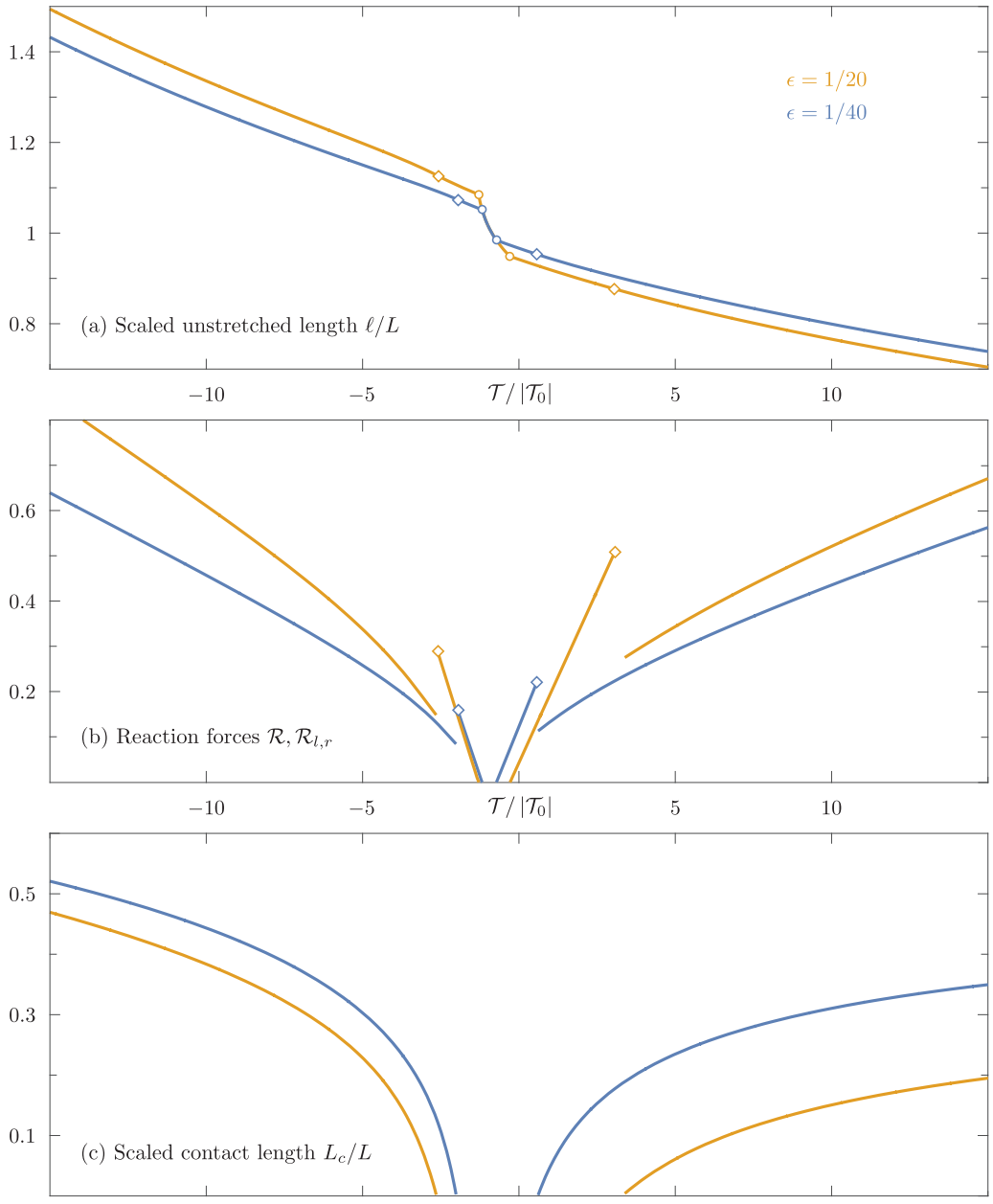

Figure IV.2.1: Progressive buckling of an initially straight elastic rod constrained inside a helical conduit. The rod is subjected to an end torque $\mathcal{M}_3 = -1$ and axial force $\mathcal{T}$. (a) Scaled unstretched length of the rod ℓ/L, (b) reaction forces $\mathcal{R}$ at the discrete contact and $\mathcal{R}_{l,r}$ at the extremities of the continuous contact, and (c) scaled contact length L_c/L as functions of the end force $\mathcal{T}/|\mathcal{T}_0|$ with $\mathcal{T}_0 = -7.069$. Results obtained for $\epsilon = 1/40$ and $\epsilon = 1/20$ are plotted in blue and orange, respectively. Circles mark the appearance of the discrete contacts and squares identify the transition from discrete to continuous contact.

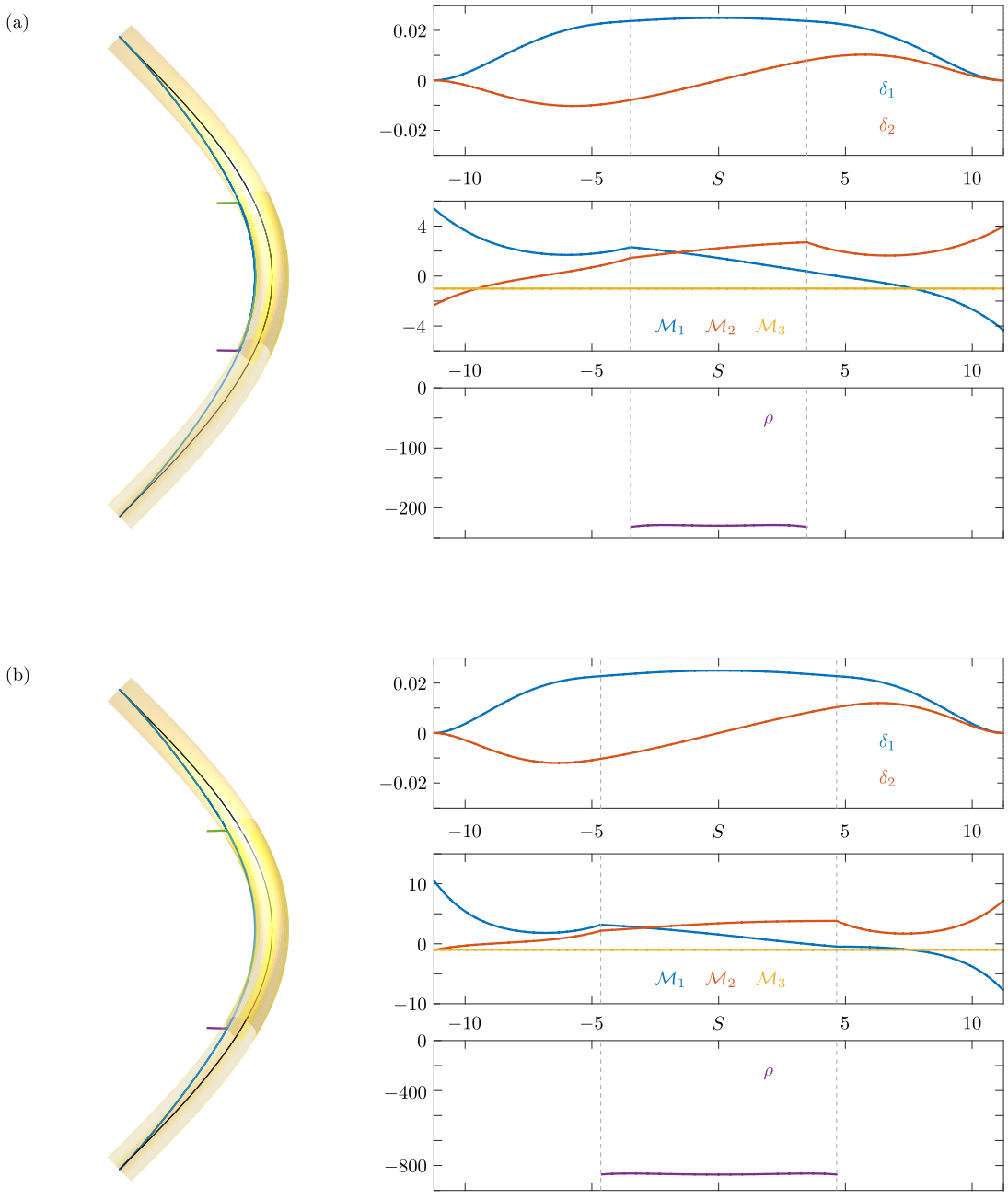

Figure IV.2.2: Deformed rod constrained inside a helical conduit of radius $\epsilon = 1/40$ for (a) $\mathcal{T} = 10\,|\mathcal{T}_0|$ and (b) $\mathcal{T} = 35\,|\mathcal{T}_0|$. The arrows picture the concentrated reaction forces at the extremities of the continuous contact.

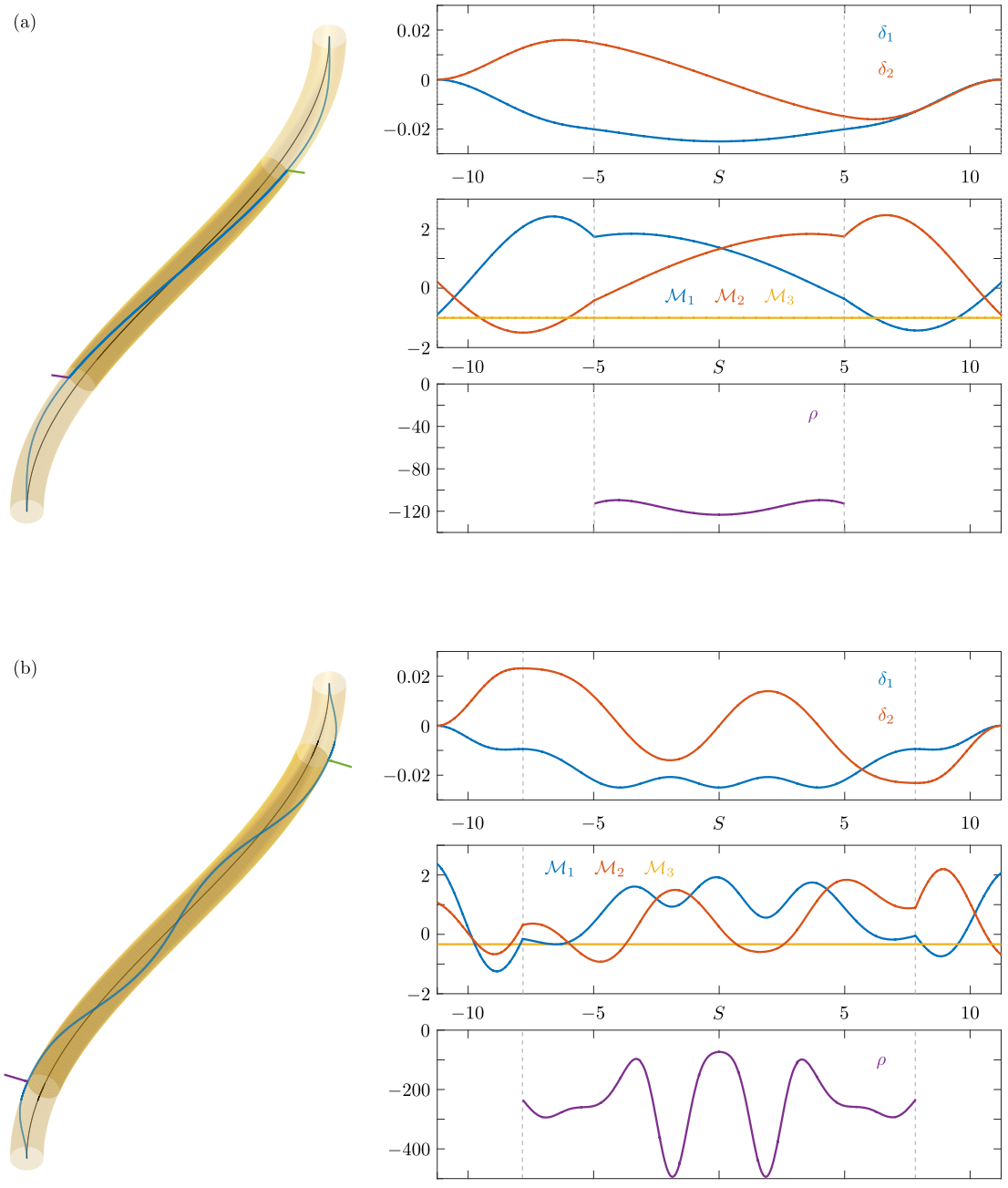

Figure IV.2.3: Buckled rod constrained inside a helical conduit of radius $\epsilon = 1/40$ for (a) $\mathcal{T} = -10\ |\mathcal{T}_0|$ and (b) $\mathcal{T} = -35\ |\mathcal{T}_0|$. The arrows picture the concentrated reaction forces at the extremities of the continuous contact.

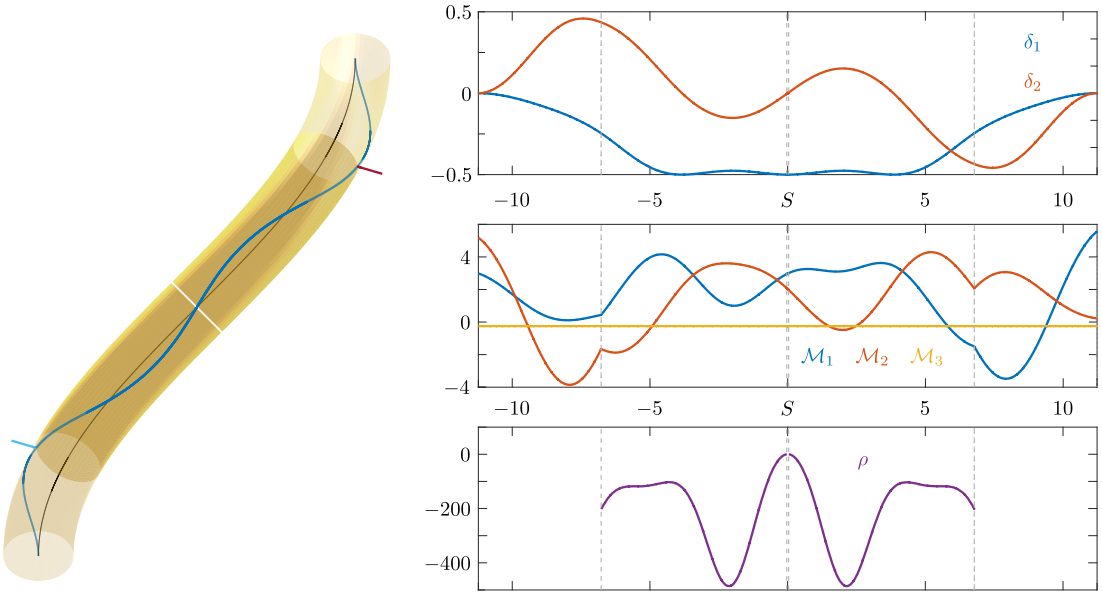

Figure IV.2.4: Buckled rod constrained inside a helical conduit of radius $\epsilon = 1/20$ for $\mathcal{T} = -24.37\ |\mathcal{T}_0|$.

Chapter V

Conclusion & Discussion

V.1 Contributions

Driven by the wealth of biological, medical and engineering applications concerned with the constrained deformation of slender elastic structures, the research work presented in this manuscript has lead to the formulation of a computational model for the solution of elastic rods constrained inside or around tube-like surfaces. The segmentation strategy adopted to cope with this complex class of problems consists in sequencing the global problem into, comparatively simpler, elementary problems either in continuous contact with the constraint or contact-free between their extremities. Within the conventional Lagrangian formulation of elastic rods, this approach is however associated with two major drawbacks. First, the boundary conditions specifying the locations of the rod centerline at both extremities of each elementary problem lead to the establishment of isoperimetric constraints, *i.e.*, integral constraints on the unknown length of the rod. Second, the assessment of the unilateral contact condition requires, in principle, the comparison of two curves parametrized by distinct curvilinear coordinates, *viz.* the rod centerline and the constraint axis. Both conspire to burden the (numerical) computations associated with the method. To streamline the solution along the elementary problems and rationalize the assessment of the unilateral contact condition, we reformulated the rod governing equations within the Eulerian framework of the constraint. The methodical exploration of both types of elementary problems led to specific formulations of the rod governing equations that stress the profound connection between the mechanics of the rod and the geometry of the constraint surface.

Eulerian formulation of elastic rods deforming in space

Both elementary configurations corresponding to rod segments either in continuous contact with the constraint or contact-free have been investigated simultaneously on the assumption that

they essentially differ by the nature of the body force acting along the rod. A *general* Eulerian formulation of elastic rods was derived by *(i)* describing the rod deformed configuration $\mathscr{E}$ by means of its relative deflection with respect to the constraint axis $\mathscr{C}$, and *(ii)* expressing the kinematical as well as mechanical quantities pertaining to the rod in terms of the curvilinear coordinate associated with the reference curve.

This formulation circumvents both drawbacks that afflict the conventional Lagrangian approach associated with segmentation strategy. The restatement of the rod local equilibrium in terms of the Eulerian curvilinear coordinate indeed untangles the solution of free boundary problems associated with rods forced to go through two distinct fixed points in space. The isoperimetric constraints vanish and the resolution reduces to that of a classical boundary value problem of mixed order. Additionally, the description of the rod deflection by means of its eccentricity with respect to the constraint axis trivializes the assessment of the unilateral contact condition. The detection of emerging contacts throughout contact-free problems reduces to the comparison of the eccentricity magnitude with the constraint radius while, along continuous contacts, the rod is compelled to lay on the constraining surface by straightforwardly imposing the amplitude of this eccentricity.

Lagrangian formulation of surface bound elastic rods

Focusing on the continuous contact between an elastic rod and a rigid surface, the equation governing the static equilibrium of rods have been recast to emphasize the influence of the constraint local geometry on the configuration of the rod centerline and the reaction pressure. The resulting Lagrangian formulation, adapted to surface bound configurations, was obtained by *(i)* specifying the location of the rod axis in terms of its coordinates in the parameter space associated with the constraint surface parameterization, and *(ii)* characterizing the orientation of the rod material frame through its rotation with respect to the normal to the surface. This formulation led to an explicit representation of the rod centerline in which the strain variables, measuring the rod change of shape, are expressed in terms of the geometric invariants $(\kappa_g, \kappa_n, \tau_g)$.

Considering a spherical constraining surface, the proposed formulation was further investigated and validated by recovering known results. It was shown that the geodesic curvature of an elastica constrained on a sphere and the intrinsic curvature of a planar elastica satisfy identical governing equations. Accounting for the symmetry of the problem, the conditions under which the elastica closes around the sphere were derived. Although the relaxation of the inextensibility assumption was associated with the loss of integrability, the parallelism with planar configurations was shown to be maintained and the distinction between wavelike and orbit-like solutions preserved.

Eulerian formulation of elastic rods deforming on a normal ringed surface

Particularizing the Lagrangian description of surface bound rods to the continuous contact with normal ringed surfaces, an Eulerian formulation was derived by *(i)* describing the rod deformed configuration $\mathscr{E}$ by means of its angular position on the constraint surface and *(ii)* expressing the kinematical as well as mechanical quantities pertaining to the rod in terms of the curvilinear coordinate associated with the constraint axis.

The restatement of the rod local equilibrium in terms of the Eulerian curvilinear coordinate again prove to be particularly appropriate to treat free boundary value problems that are subjected to self-feeding. The isoperimetric constraints indeed vanish and the solution reduces to that of a system of differential-algebraic equations associated with classical boundary conditions. To illustrate this formulation, periodic solutions on the torus were then investigated and shown to be topologically equivalent to torus knots.

Global computational model

Formalizing the segmentation strategy, a computational model that exploits the Eulerian formulation of the rod governing equation has been assembled. To solve the quasi-static deflection of elastic rods constrained inside or around a perfectly stiff, frictionless, normal ringed surface, it identifies the contact pattern (*i.e.*, the number of contacts and their nature, the rod configuration at the connections) that satisfies the unilateral contact condition and preserves the rod integrity along the sequence of elementary problems. This procedure was systematized in an algorithm that involves three nested loops. Assuming a contact pattern and the associated rod configuration at the connections, the inner loop propagates the resolution of elementary problems along the sequence, from one extremity to the other. The median loop then restores the rod continuity at the connections by adjusting the position and inclination of the connections. Eventually, the outer loop ensures that the unilateral contact condition is respected along the global problem and, if required, modifies the contact pattern.

V.2 Limitations

Although, associated with a segmentation strategy, the Eulerian formulation for elastic rods developed in this manuscript simplifies both the solution of the rod configuration along each elementary problem and the assessment of the non-penetration condition, it limits the range of potential configurations adopted by the rod. Selecting the positive sign in equations (II.2.3) and (III.2.4) indeed imposes the mapping from Eulerian to Lagrangian coordinates to be increasing and prevents the appearance of solutions associated with curling or writhing, or even the formation of plies. While, in a vast majority of applications, these configurations are unlikely to occur and may be regarded as parasitic, they may be essential to the simulation and understanding of other phenomena such as DNA supercoiling. The proposed Eulerian formulation

actually prohibits solutions along which the tangent to the rod centerline is, at some points, orthogonal to the constraint axis.

Build upon the rod theory, the Eulerian formulation shares its fundamental assumptions and, therefore, inherits its limitations. This theory of one-dimensional elastic body, which allows for approximate solutions of the three-dimensional equations of nonlinear elasticity, is only satisfactory for a limited range configurations, loading and boundary conditions. Essential to its validity, the slenderness assumption requires that the rod transverse dimensions be significantly smaller than its length. This restriction may indeed limit the applicability of the method to industrial or medical applications in which the rod is not sufficiently thin/long. Although rotations with respect to the initial configuration may be large, the strains associated with the deformed configuration must remain small. Also, the hypothesis of isotropic and perfectly elastic Hookean material fails to account for the potential plastic deformations of the rod, which may occur in some applications (*e.g.* oil and gas industry.) In this work, the shear deformations were further neglected. For rods with a circular cross section, this assumption is however expected to have little impact on the global solution.

As already emphasized, the approach proposed in this thesis to establish the correct contact pattern is unfortunately not guaranteed to converge. In exceptional circumstances, several adaptations of the contact pattern may indeed be required simultaneously, situations that the present implementation of the procedure fail to account for. In this context, it may be beneficial to punctually *steer* the procedure towards an educated guess of the correct contact pattern.

V.3 Directions for future work

As for every mathematical or numerical model, the computational model developed in this research work requires to be verified and validated. These crucial steps not only allow to evaluate the degree to which the model is an accurate representation of the real world, but also quantify the confidence in its predictive capability. Although the Eulerian formulation, in both contact-free and continuous contact configurations, has been shown to properly degenerate to known analytical solutions, the numerical implementation of the global computational model presented in the previous Chapter should be further verified through rigorous comparison with benchmarks, experimental data and/or simulations obtained with commercial codes. Similarly, a proper calibration of the parameters involved in this algorithm (such as the tolerances, the degree of the B–spline approximations, etc.) should be conducted. As emphasized in the previous Section, the contact pattern switcher, as presented in this work, should be seen as a proof of concept that requires further investigations as well as the identification of its strength and potential flaws.

Although the Eulerian formulations proposed in Sections II.2 and III.2 are restricted to quasi-static solutions of the governing equations, they can readily be extended to incorporate the rod dynamics by adding inertial terms to equations (II.1.12–II.1.13) and redefining the eccentricity vector and the polar angle, as well as every other dependent quantity, as time-dependent.

Similarly, the assumption of frictionless interaction between the rod and the constraining surface may be relaxed and friction forces introduced through the components (f_g, f_3) of the body forces, however requiring to deal with evolutive problems as solutions become history dependent. Finally, the definition of the constraint surface may be extended to include constraints with non-circular cross sections, *e.g.,* by describing its local geometry in the $\{\boldsymbol{D}_1, \boldsymbol{D}_2\}$–basis, and account for its deformability, which is essential to biomedical applications.

The numerical solution of boundary value problems for ordinary differential equations, let alone differential-algebraic equations, is an incredibly complex field of research involving numerous areas of both mathematics and numerical analysis. Similarly, the techniques that may be applied to the solution of system of nonlinear equations far outreach the scope of this thesis. The numerical implementation outlined in this manuscript is intentionally simple. However inevitable, the means and methods that have been implemented indeed do not fundamentally characterize the methodology formulated in this work and were essentially serving an illustrative purpose. Hence, various enhancements could be brought to this numerical implementation in order to streamline and accelerate the solution. One can for instance consider adaptive knot sequences that optimize the error of the approximate solution along each elementary problem by varying the number of Gauss points per subinterval, as well as the number and extent of these subintervals. For higher order convergence and more stable numerical scheme, an alternative basis could also be used for the piecewise polynomial solutions (Ascher et al., 1983; Bader and Ascher, 1987). To lessen the computational expense incurred at every iteration, the Jacobian matrix associated with the system (IV.1.17) could potentially be updated using Broyden's method (Dennis and Schnabel, 1996; Press et al., 2007). For the same purpose and allow real-time simulations, alternative programming languages should also be considered.

"[...] every word or concept, clear as it may seem to be, has only a limited range of applicability".

Heisenberg (1958)

References

Aadnøy, B. and K. Andersen (2001). Design of oil wells using analytical friction models. *Journal of Petroleum Science and engineering 32*(1), 53–71.

Alderliesten, T., M. Konings, and W. Niessen (2007). Modeling friction, intrinsic curvature, and rotation of guide wires for simulation of minimally invasive vascular interventions. *Biomedical Engineering, IEEE Transactions on 54*(1), 29–38.

Antman, S. (2005). *Nonlinear problems of elasticity* (3rd ed.), Volume 107, Chapter 8. Springer Verlag.

Antman, S. and C. Kenney (1981). Large buckled states of nonlinearly elastic rods under torsion, thrust, and gravity. *Archive for rational mechanics and analysis 76*(4), 289–338.

Ascher, U., J. Christiansen, and R. D. Russell (1979). A collocation solver for mixed order systems of boundary value problems. *Mathematics of Computation 33*(146), 659–679.

Ascher, U., J. Christiansen, and R. D. Russell (1981). Collocation software for boundary-value ODEs. *ACM Trans. Math. Softw. 7*(2), 209–222.

Ascher, U., R. Mattheij, and R. D. Russell (1995). *Numerical Solution of Boundary Value Problems for Ordinary Differential Equations*. Society for Industrial and Applied Mathematics.

Ascher, U., S. Pruess, and R. D. Russell (1983). On spline basis selection for solving differential equations. *SIAM Journal on Numerical Analysis 20*(1), 121–142.

Ascher, U. M. and R. J. Spiteri (1994). Collocation software for boundary value differential-algebraic equations. *SIAM Journal on Scientific Computing 15*, 938–952.

Audoly, B. and Y. Pomeau (2010). *Elasticity and geometry: from hair curls to the non-linear response of shells*. Oxford University Press.

Aumann, G. (1995). Curvature continuous connections of cones and cylinders. *Computer-Aided Design 27*(4), 293 – 301.

Bader, G. and U. Ascher (1987). A new basis implementation for a mixed order boundary value ode solver. *SIAM Journal on Scientific and Statistical Computing 8*(4), 483–500.

Baim, D. (2005). *Grossman's cardiac catheterization, angiography, and intervention*, Volume 1. Lippincott Williams & Wilkins.

Bastl, B., B. Jüttler, M. Lávička, T. Schulz, and Z. Šír (2014). On the parameterization of rational ringed surfaces and rational canal surfaces. *Mathematics in Computer Science 8*(2), 299–319.

Bergou, M., B. Audoly, E. Vouga, M. Wardetzky, and E. Grinspun (2010). Discrete viscous threads. *ACM Transactions on Graphics 29*(4), 116:1–116:10.

Bergou, M., M. Wardetzky, S. Robinson, B. Audoly, and E. Grinspun (2008). Discrete elastic rods. *ACM Transactions on Graphics 27*(3).

Bernoulli, J. (1694). Curvatura laminae elasticae. *Acta Eruditorum 13*, 262–276.

Bishop, R. L. (1975). There is more than one way to frame a curve. *The American Mathematical Monthly 82*(3), 246–251.

Bizzarri, M. and M. Lávička (2015). On modeling with rational ringed surfaces. *Computer-Aided Design 58*(0), 151 – 161. Solid and Physical Modeling 2014.

Bosi, F., D. Misseroni, F. Dal Corso, and D. Bigoni (2014). An elastica arm scale. *Proceedings of the Royal Society A: Mathematical, Physical and Engineering Science 470*(2169).

Bosi, F., D. Misseroni, F. Dal Corso, and D. Bigoni (2015). Self-encapsulation, or the 'dripping' of an elastic rod. *Proceedings of the Royal Society of London A: Mathematical, Physical and Engineering Sciences 471*(2179).

Brett, J. F., A. D. Beckett, C. A. Holt, and D. L. Smith (1989, September). Uses and limitations of drillstring tension and torque models for monitoring hole conditions. *SPE Drilling Engineering 4*(SPE 16664), 223–229.

Brunnett, G. (1993). The curvature of plane elastic curves. *NASA STI/Recon Technical Report N 93*, 28516.

Brunnett, G. and P. E. Crouch (1994). Elastic curves on the sphere. *Advances in Computational Mathematics 2*(1), 23–40.

Cartan, E. (1937). *La théorie des groupes finis et continus et la géométrie différentielle: traitées par la méthode du repère mobile.* Gauthier-Villars.

Cauchy, A. L. (1826). *Leçons sur les applications du calcul infinitésimal à la géométrie.* Leçons sur les applications du calcul infinitésimal à la géométrie. Paris: Imprimerie Royale.

Chai, H. (2002, June). On the post-buckling behavior of bilaterally constrained plates. *International Journal of Solids and Structures 39*(11), 2911–2926.

Chai, H. (2006, September). On the crush worthiness of a laterally confined bar under axial compression. *Journal of Applied Mechanics - Transactions of the Asme 73*(5), 834–841.

Chen, J.-S. and C.-W. Li (2007). Planar elastica inside a curved tube with clearance. *International Journal of Solids and Structures 44*(18–19), 6173–6186.

Chen, J.-S. and H.-C. Li (2011). On an Elastic Rod Inside a Slender Tube Under End Twisting Moment. *Journal of Applied Mechanics 78*(4), 041009.

Chen, J.-S. and W.-C. Ro (2010). Deformations and Stability of an Elastica Subjected to an Off-Axis Point Constraint. *Journal of Applied Mechanics - Transactions of the Asme 77*(3).

Cheng, H. and K. C. Gupta (1989). An historical note on finite rotations. *Journal of Applied Mechanics 56*(1), 139–145.

Chui, C., Z. Li, J. Anderson, K. Murphy, A. Venbrux, X. Ma, Z. Wang, P. Gailloud, Y. Cai, Y. Wang, et al. (2002). Training and pretreatment planning of interventional neuroradiology procedures–initial clinical validation. *Studies in health technology and informatics 85*, 96.

Clebsch, A. (1862). *Theorie der elasticität fester körper*. B.G. Teubner, Leipzig.

Cooke, W. (2000, June). *Mathematics of crimping*. Ph. D. thesis, University of Oxford.

Cosserat, E. and F. Cosserat (1909). *Théorie des corps déformables*, Chapter 2. Librairie Scientifique A. Hermann et fils, Paris.

Cotin, S., S. Dawson, D. Meglan, D. Shaffer, M. Ferrell, R. Bardsley, F. Morgan, T. Nagano, J. Nikom, P. Sherman, et al. (2000). Icts, an interventional cardiology training system. *Studies in health technology and informatics*, 59–65.

Cotin, S., C. Duriez, J. Lenoir, P. Neumann, and S. Dawson (2005). New approaches to catheter navigation for interventional radiology simulation. *Medical Image Computing and Computer-Assisted Intervention–MICCAI 2005*, 534–542.

Cunha, J. (2004). Buckling of tubulars inside wellbores: a review on recent theoretical and experimental works. *SPE Drilling & Completion 19*(1), 13–19.

da Fonseca, A. F. and M. A. de Aguiar (2003). Solving the boundary value problem for finite Kirchhoff rods. *Physica D: Nonlinear Phenomena 181*(1 – 2), 53 – 69.

Dawson, S. (2006). Procedural simulation: a primer. *Radiology 241*(1), 17–25.

de Boor, C. (2005). *Spline toolbox for use with MATLAB: user's guide*. MathWorks.

de Boor, C. and B. Swartz (1973). Collocation at gaussian points. *SIAM Journal on Numerical Analysis 10*(4), 582–606.

Dennis, J. E. and R. B. Schnabel (1996). *Numerical Methods for Unconstrained Optimization and Nonlinear Equations*. Society for Industrial and Applied Mathematics.

Denoël, V. (2008). Advantages of a semi-analytical approach for the analysis of an evolving structure with contacts. *Communications in Numerical Methods in Engineering 24*(12), 1667–1683.

Denoël, V. and E. Detournay (2009a). Multiple scales solution for a beam with a small bending stiffness. *Journal of engineering mechanics 136*(1), 69–77.

Denoël, V. and E. Detournay (2009b, March). The problem of a drillstring inside a curved borehole: a perturbed eulerian approach. In *First International Colloquium on Non-linear Dynamics of Deep Drilling Systems*, pp. 89–95.

Denoël, V. and E. Detournay (2011). Eulerian formulation of constrained elastica. *International Journal of Solids and Structures 48*(3-4), 625 – 636.

Deweese, J. E., M. A. Osheroff, and N. Osheroff (2008). Dna topology and topoisomerases: Teaching a "knotty"subject. *Biochemistry and molecular biology education : a bimonthly publication of the International Union of Biochemistry and Molecular Biology 37*(1), 2–10.

Dill, E. (1992). Kirchhoff's Theory of Rods. *Archive for History of Exact Sciences 44*(1), 1–23.

Do Carmo, M. P. (1976). *Differential geometry of curves and surfaces*. Prentice-Hall, Inc.

Donato, C. C., M. A. F. Gomes, and R. E. de Souza (2003). Scaling properties in the packing of crumpled wires. *Phys. Rev. E 67*, 026110.

Donea, J., A. Huerta, J.-P. Ponthot, and A. Rodríguez-Ferran (2004). *Arbitrary Lagrangian–Eulerian Methods*, Chapter 14, pp. 413–437. John Wiley & Sons, Ltd.

Euler, L. (1744). *Methodus inveniendi lineas curvas maximi minimive proprietate gaudentes, sive solutio problematis isoperimetrici lattissimo sensu accepti (Additamentum I: De curvis elasticis)*, Volume 24 of *Opera Omnia, Series 1*. Bousquent, Lausanne.

Fang, J., S.-Y. Li, and J.-S. Chen (2013). On a compressed spatial elastica constrained inside a tube. *Acta Mechanica 224*(11), 2635–2647.

Friedman, A. (2000). Free boundary problems in science and technology. *Notices of the AMS 47*(8), 854–861.

Gleick, J. (2011). *Genius: The Life and Science of Richard Feynman*. Open Road Media.

Gomes, M. A. F., V. P. Brito, and M. S. Araújo (2008). Geometric properties of crumpled wires and the condensed non-solid packing state of very long molecular chains. *Journal of the Brazilian Chemical Society 19*, 293 – 298.

Goriely, A. and S. Neukirch (2006, Nov). Mechanics of climbing and attachment in twining plants. *Phys. Rev. Lett. 97*, 184302.

Goriely, A., M. Robertson-Tessi, M. Tabor, and R. Vandiver (2008). Elastic growth models. In *Mathematical Modelling of Biosystems*, Volume 102 of *Applied Optimization*, pp. 1–44. Springer.

Goriely, A. and M. Tabor (1997c). Nonlinear dynamics of filaments: III. instabilities of helical rods. *Proceedings of the Royal Society of London. Series A: Mathematical, Physical and Engineering Sciences 453*(1967), 2583–2601.

Goyal, S., N. Perkins, and C. Lee (2005). Nonlinear Dynamics and Loop Formation in Kirchhoff Rods with Implications to the Mechanics of DNA and Cables. *Journal of Computational Physics 209*(1), 371–389.

Gray, A. (1996). *Modern Differential Geometry of Curves and Surfaces with Mathematica*. CRC Press, Inc.

Guarracino, F. and V. Mallardo (1999). A refined analytical analysis of submerged pipelines in seabed laying. *Applied Ocean Research 21*(6), 281 – 293.

Guven, J., D. María Valencia, and P. Vázquez-Montejo (2014). Environmental bias and elastic curves on surfaces. *Journal of Physics A Mathematical General 47*, I5201.

Guven, J. and P. Vázquez-Montejo (2012). Confinement of semiflexible polymers. *Phys. Rev. E 85*, 026603.

Hartmann, E. (2001). Gn-continuous connections between normal ringed surfaces. *Computer Aided Geometric Design 18*(8), 751–770.

Heisenberg, W. (1958). *Physics and Philosophy: The Revolution in Modern Science*. Great minds series.

Hicks, J. (2015). This FDA approved device performs robotic angioplasty and reduces radiation for cardiologists. Forbes, http://onforb.es/1hLlTzz. Last checkes November 16, 2015.

Ho, H. (1988). An improved modeling program for computing the torque and drag in directional and deep wells. In *SPE Annual Technical Conference and Exhibition*.

Huang, N. and P. Pattillo (2000). Helical buckling of a tube in an inclined wellbore. *International journal of non-linear mechanics 35*(5), 911–923.

Huynen, A., E. Detournay, and V. Denoël (2013). Eulerian formulation for an extensible elastic rod. In *Porceedings of the Fifth International Conference on Structural Engineering, Mechanics and Computation*.

Huynen, A., E. Detournay, and V. Denoël (2014). Eulerian formulation of the torque and drag problem. In *Third International Colloquium on Nonlinear Dynamics and Control of Deep Drilling Systems*, pp. 191 – 200.

Huynen, A., E. Detournay, and V. Denoël (2015). Surface constrained elastic rods with application to the sphere. *Journal of Elasticity*, 1–21.

Huynen, A., E. Detournay, and V. Denoël (submitted). Eulerian formulation of elastic rod.

Inglis, T. (1988). *Directional drilling*, Volume 2. Springer.

Ivey, T. A. and D. A. Singer (1999). Knot types, homotopies and stability of closed elastic rods. *Proceedings of the London Mathematical Society 79*, 429–450.

Jantzen, R. T. (2010). Geodesics on the Torus and other Surfaces of Revolution Clarified Using Undergraduate Physics Tricks with Bonus: Nonrelativistic and Relativistic Kepler Problems.

Johancsik, C., D. Friesen, and R. Dawson (1984). Torque and drag in directional wells – Prediction and measurement. *Journal of Petroleum Technology 36*(6), 987–992.

Johnstone, J. K. (1993). A new intersection algorithm for cyclides and swept surfaces using circle decomposition. *Comput. Aided Geom. Des. 10*(1), 1–24.

Kehrbaum, S. and J. Maddocks (1997). Elastic rods, rigid bodies, quaternions and the last quadrature. *Philosophical Transactions: Mathematical, Physical and Engineering Sciences*, 2117–2136.

Kirchhoff, G. (1859). Über das gleichgewicht und die bewegung eines unendlich dünnen elastischen stabes. *Journal für die reine und angewandte Mathematik 56*, 285–313.

Kirchhoff, G. (1876). *Vorlesungen über mathematische Physik: Mechanik*. B. G. Teubner (Leipzig).

Konings, M., E. Van de Kraats, T. Alderliesten, and W. Niessen (2003). Analytical guide wire motion algorithm for simulation of endovascular interventions. *Medical and Biological Engineering and Computing 41*(6), 689–700.

Lagrange, J.-L. (1797). *Théorie des fonctions analytiques*. Paris: Imprimerie de la Republique.

LaMarque, J. C., T.-v. L. Le, and S. C. Harvey (2004). Packaging double-helical dna into viral capsids. *Biopolymers 73*(3), 348–355.

Langer, J. and D. A. Singer (1984a). Knotted elastic curves in R^3. *Journal of the London Mathematical Society 30*, 512–520.

Langer, J. and D. A. Singer (1984b). The total squared curvature of closed curves. *Journal of Differential Geometry 20*(1), 1–22.

Langer, J. and D. A. Singer (1996). Lagrangian aspects of the Kirchhoff elastic rod. *SIAM Review 38*(4), 605–618.

Lee, E. H. and G. E. Forsythe (1973). Variational study of nonlinear spline curves. *SIAM Review 15*(1), pp. 120–133.

Levien, R. (2008). The elastica: a mathematical history. Technical Report UCB/EECS-2008-103, EECS Department, University of California, Berkeley.

Li, S.-Y. and J.-S. Chen (2014). A twisted elastica constrained inside a tube. *European Journal of Mechanics - A/Solids 44*(0), 61 – 74.

Love, A. (1927). *A Treatise on the Mathematical Theory of Elasticity* (4^{th} ed.). Cambridge University Press.

Lü, W. and H. Pottmann (1996). Pipe surfaces with rational spine curve are rational. *Computer Aided Geometric Design 13*(7), 621 – 628.

Luboz, V., R. Blazewski, D. Gould, and F. Bello (2009). Real-time guidewire simulation in complex vascular models. *The Visual Computer 25*(9), 827–834.

Luboz, V., J. Zhai, P. Littler, T. Odetoyinbo, D. Gould, T. How, and F. Bello (2010). Endovascular guidewire flexibility simulation. *Biomedical Simulation 5958*, 171–180.

Macdonald, K. and J. Bjune (2007). Failure analysis of drillstrings. *Engineering Failure Analysis 14*(8), 1641–1666.

Maidla, E. and A. Wojtanowicz (1987). Field comparison of 2-d and 3-d methods for the borehole friction evaluation in directional wells. In *SPE Annual Technical Conference and Exhibition*.

Marck, J., E. Detournay, A. Kuesters, and J. Wingate (2014). Analysis of spiraled-borehole data by use of a novel directional-drilling model. *SPE Drilling & Completion 29*(03), 167–278.

Mason, C. and D. Chen (2007). Step changes needed to modernise T&D software. In *SPE/IADC Drilling Conference*.

McClendon, R. (1985). Directional drilling using the catenary method. In *SPE/IADC Drilling Conference*.

McSpadden, A. and K. Newman (2002). Development of a stiff-string forces model for coiled tubing. In *SPE/ICoTA Coiled Tubing Conference and Exhibition*.

Melzak, Z. A. (2014). *Invitation to geometry*. Dover Publications, Inc.

Menand, S., H. Sellami, M. Tijani, J. Akowanou, and C. Simon (2009). Buckling of tubulars in simulated field conditions. *SPE Drilling & Completion 24*(2), 276–285.

Menand, S., H. Sellami, M. Tijani, O. Stab, D. Dupuis, and C. Simon (2006). Advancements in 3d drillstring mechanics: From the bit to the topdrive. In *IADC/SPE Drilling Conference*.

Miller, J., T. Su, J. Pabon, N. Wicks, K. Bertoldi, and P. Reis (2015). Buckling of a thin elastic rod inside a horizontal cylindrical constraint. *Extreme Mechanics Letters 3*, 36 – 44.

Mitchell, R. F. and R. Samuel (2007, February). How good is the torque-drag model? In *SPE/IADC Drilling Conference*, Number SPE/IADC 105068, Amsterdam, Netherlands, pp. 1–9.

Morgan, R. and E. Walser (2010). *Handbook of Angioplasty and Stenting Procedures*. Springer.

Moulton, D., T. Lessinnes, and A. Goriely (2012). Morphoelastic rods part 1: A single growing elastic rod. *Journal of the Mechanics and Physics of Solids*.

Newman, K. and R. Procter (2009). Analysis of hook load forces during jarring. In *SPE/IADC Drilling Conference and Exhibition*.

Nickerson, H. and G. Manning (1988). Intrinsic equations for a relaxed elastic line on an oriented surface. *Geometriae Dedicata 27*(2), 127–136.

Nizette, M. and A. Goriely (1999). Towards a classification of Euler–Kirchhoff filaments. *Journal of mathematical physics 40*, 2830.

Odijk, T. (2004). Statics and dynamics of condensed dna within phages and globules. *Philosophical Transactions of the Royal Society of London A: Mathematical, Physical and Engineering Sciences 362*(1820), 1497–1517.

Olver, F. W. J., D. W. Lozier, and R. F. Boisvert (2010). *NIST handbook of mathematical functions*. Cambridge University Press.

Perneder, L. and E. Detournay (2013). Steady-state solutions of a propagating borehole. *International Journal of Solids and Structures 50*(9), 1226–1240.

Press, W. H., S. A. Teukolsky, W. T. Vetterling, and B. P. Flannery (2007). *Numerical Recipes: The Art of Scientific Computing* (Third ed.). Cambridge University Press.

Pressley, A. (2010). *Elementary Differential Geometry*. Springer London.

Rezmer-Cooper, I., M. Chau, A. Hendricks, M. Woodfine, B. Stacey, and N. Downton (1999). Field data supports the use of stiffness and tortuosity in solving complex well design problems. In *SPE/IADC drilling conference*.

Russell, R. and L. Shampine (1972). A collocation method for boundary value problems. *Numerische Mathematik 19*(1), 1–28.

Saint-Venant, A.-J.-C. B. d. (1843). Sur le calcul de la résistance et de la flexion des pièces solides à simple ou à double courbure, en prenant simultanément en considération les divers efforts auxquels elles peuvent être soumises dans tous les sens. *Comptes rendus de l'Académie des Sciences 17*, 942–954.

Sampaio, J. H. B. (2008). *Drilling Engineering*. Curtin University of Technology, Department of Petroleum Engineering.

Schneider, P. (2003). *Endovascular skills: guidewire and catheter skills for endovascular surgery*. CRC Press.

Seemann, W. (1996). Deformation of an elastic helix in contact with a rigid cylinder. *Archive of Applied Mechanics 67*(1–2), 117–139.

Sheppard, M., C. Wick, and T. Burgess (1987). Designing well paths to reduce drag and torque. *SPE Drilling Engineering 2*(4), 344–350.

Shi, Y. and J. Hearst (1994). The Kirchhoff elastic rod, the nonlinear Schrödinger equation, and DNA supercoiling. *The Journal of chemical physics 101*, 5186.

Smilowitz, N. R., S. Balter, and G. Weisz (2013). Occupational hazards of interventional cardiology. *Cardiovascular Revascularization Medicine 14*(4), 223 – 228.

Stoop, N., J. Najafi, F. K. Wittel, M. Habibi, and H. J. Herrmann (2011, May). Packing of elastic wires in spherical cavities. *Phys. Rev. Lett. 106*, 214102.

Stump, D. and G. van der Heijden (1999). Matched asymptotic expansions for bent and twisted rods: applications for cable and pipeline laying. *Journal of engineering mathematics 38*(1), 13–31.

Su, T., N. Wicks, J. Pabon, and K. Bertoldi (2013). Mechanism by which a frictionally confined rod loses stability under initial velocity and position perturbations. *International Journal of Solids and Structures 50*(14—15), 2468 – 2476.

Swigon, D., B. D. Coleman, and I. Tobias (1998). The elastic rod model for DNA and its application to the tertiary structure of DNA minicircles in mononucleosomes. *Biophysical journal 74*(5), 2515–2530.

Tan, Z. and J. Witz (1995). On the deflected configuration of a slender elastic rod subject to parallel terminal forces and moments. *Proceedings of the Royal Society of London. Series A: Mathematical and Physical Sciences 449*(1936), 337–349.

Thompson, J. and A. Champneys (1996). From helix to localized writhing in the torsional post-buckling of elastic rods. *Proceedings of the Royal Society of London. Series A: Mathematical, Physical and Engineering Sciences 452*(1944), 117–138.

Thompson, J., M. Silveira, G. van der Heijden, and M. Wiercigroch (2012). Helical post-buckling of a rod in a cylinder: with applications to drill-strings. *Proceedings of the Royal Society A: Mathematical, Physical and Engineering Science 468*(2142), 1591–1614.

Tobias, I., D. Swigon, and B. D. Coleman (2000). Elastic stability of DNA configurations. I. General theory. *Phys. Rev. E 61*, 747–758.

Travers, A. A. and J. M. T. Thompson (2004). An introduction to the mechanics of DNA. *Philosophical transactions. Series A, Mathematical, physical, and engineering sciences 362*(1820), 1265–1279.

Tu, X., S. Manohar, A. Jagota, and M. Zheng (2009). DNA sequence motifs for structure-specific recognition and separation of carbon nanotubes. *Nature 460*(7252), 250 – 253.

van der Heijden, G. (2001). The static deformation of a twisted elastic rod constrained to lie on a cylinder. *Proceedings of the Royal Society of London. Series A: Mathematical, Physical and Engineering Sciences 457*(2007), 695–715.

van der Heijden, G., S. Neukirch, V. Goss, and J. Thompson (2003). Instability and self-contact phenomena in the writhing of clamped rods. *International journal of mechanical sciences 45*(1), 161–196.

van der Heijden, G. and J. Thompson (2000). Helical and localised buckling in twisted rods: A unified analysis of the symmetric case. *Nonlinear Dynamics 21*(1), 71–99.

van der Heijden, G. H. M., A. Champneys, and J. Thompson (2002). Spatially complex localisation in twisted elastic rods constrained to a cylinder. *International Journal of Solids and Structures 39*(7), 1863 – 1883.

Velten, K. (2009). *Principles of Mathematical Modeling*, Chapter 1, pp. 1–46. John Wiley & Sons.

Watson, J. D. (2010). *The double helix: A personal account of the discovery of the structure of DNA*. Hachette UK.

Watson, J. D. and F. H. C. Crick (1953). Molecular structure of nucleic acids: A structure for deoxyribose nucleic acid. *Nature 171*(4356), 737–738.

Weill, A., T. Nguyen, D. Gontard, M. Gamal, D. Roy, J. Raymond, and F. Guilbert (2007). Ri-ws-1 simulateurs informatises de procedures endovasculaires: recueil et analyse d'opinions, fonction de l'experience de l'operateur. *Journal de Radiologie 88*(10), 1583.

Wilson, T. and O. Yalcin (1992). Two double azimuth-double S-shaped wells planned and drilled using torque and drag modeling. In *SPE/IADC Drilling Conference*.

Wu, A., G. Hareland, and M. Fazaelizadeh (2011). Torque & drag analysis using finite element method. *Modern Applied Science 5*(6), 13.

Wu, J. and H. Juvkam-Wold (1995). The effect of wellbore curvature on tubular buckling and lockup. *Journal of Energy Resources Technology-Transactions of The ASME 117*(3), 214–218.

Yang, Y. and L. S. Couchman (1997). Elastic theory of nucleosomal DNA. *Proceedings of the Royal Society of London A: Mathematical, Physical and Engineering Sciences 453*(1957), 225–254.

Yi, Y., B. Lund, B. Aas, A. He, R. Rommetveit, L. Salem, S. Stokka, and F. Bottazzi (2004). An advanced coiled tubing simulator for calculations of mechanical and flow effects; model advancements, and full-scale verification experiments. In *SPE/ICoTA Coiled Tubing Conference and Exhibition*.

Zifeng, L., L. Xisheng, and Z. Daqian (1993). A steady tension-torque model for drillstring in horizontal wells. *Society of Petroleum Engineers*.

Appendix A

A.1 The Kirchhoff-Clebsch-Love Reduction

Restricting ourselves to rods of circular cross section initially straight, this Appendix is a summary of the general ideas of Kirchhoff-Clebsch-Love as presented by Dill (1992) in the framework of modern continuum mechanics.

The position vector of a material point of the undeformed body can be expressed in the form

$$\boldsymbol{q}^0\left(a_1, a_2, s\right) = \boldsymbol{r}^0 + a_1\,\boldsymbol{d}_1^0 + a_2\,\boldsymbol{d}_2^0, \tag{A.1.1}$$

where (a_1, a_2) are the coordinates of the point in the cross section s spanned by the directors $\boldsymbol{d}_1^0(s)$ and $\boldsymbol{d}_2^0(s)$. Due to the combined effects of bending and twisting, the same material point in the deformed configuration is tracked by the position vector

$$\boldsymbol{q}\left(a_1, a_2, s\right) = \boldsymbol{r} + a_1\,\boldsymbol{d}_1 + a_2\,\boldsymbol{d}_2 + b_j\,\boldsymbol{d}_j, \tag{A.1.2}$$

where the b_j's account for the unknown local displacements of the material point. The component b_3 is solely responsible for the wrapping of the cross section, that is a plane cross section does not necessarily remains plane in the deformed body. Considering only configurations in which these local displacement and their material derivatives are small, Kirchhoff's equations are obtained as the first order terms of an asymptotic expansion where the small parameter is the largest of the numbers $a/\ell, a\left\|\boldsymbol{u}\right\|, (1-\alpha)$ with a the radius of the rod cross section and $\ell = s_b - s_a$ the length of the rod in its reference configuration.

Further assuming the tractions on the sides of the body to be small and the rod to be made of a homogenous and isotropic Hookean material, the local displacement is shown (Dill, 1992) to be given by

$$b_1 = -\left(1-\alpha\right)\nu\,a_1 - \nu\,a_1\,a_2\,u_1 + \nu\frac{a_1^2 - a_2^2}{2}u_2, \tag{A.1.3}$$

$$b_2 = -\left(1-\alpha\right)\nu\,a_2 + \nu\,a_1\,a_2\,u_2 + \nu\frac{a_1^2 - a_2^2}{2}u_1, \tag{A.1.4}$$

$$b_3 = 0, \tag{A.1.5}$$

at first order, such that plane cross sections remain plane for rods with a circular cross section. In these expressions ν denotes Poisson's ration. Accordingly, the only non-zero components of the stress tensor read (at first order)

$$\sigma_{31} = -G\,a_2\,u_3, \qquad \sigma_{32} = G\,a_1\,u_3, \qquad \sigma_{33} = E\left(\alpha - 1 + a_2\,u_1 - a_1\,u_2\right), \tag{A.1.6}$$

where E is Young's modulus and G is the shear modulus. The resultant of the contact forces and the resultant couple of these forces are then obtained by integration of these stresses over

the cross section $\mathcal{A}$

$$\boldsymbol{F} = \int\int_{\mathcal{A}} \sigma_{3j}\, \boldsymbol{d}_j \mathrm{d}a_1\, \mathrm{d}a_2, \qquad \boldsymbol{M} = \int\int_{\mathcal{A}} (a_1\, \boldsymbol{d}_1 + a_2\, \boldsymbol{d}_2) \times (\sigma_{3j}\, \boldsymbol{d}_j)\, \mathrm{d}a_1\, \mathrm{d}a_2, \tag{A.1.7}$$

leading to

$$F_3 = A\,(\alpha - 1)\,, \qquad M_1 = B\,u_1, \qquad M_2 = B\,u_2 \qquad M_3 = C\,u_3 \tag{A.1.8}$$

where the axial, bending and torsional stiffnesses are defined as

$$A = E \int\int_{\mathcal{A}} \mathrm{d}a_1\, \mathrm{d}a_2, \qquad B = E \int\int_{\mathcal{A}} a_i^2\, \mathrm{d}a_1\, \mathrm{d}a_2, \qquad C = G \int\int_{\mathcal{A}} a_1^2 + a_2^2\, \mathrm{d}a_1\, \mathrm{d}a_2, \tag{A.1.9}$$

respectively. The surface integrals in equations (A.1.9) correspond to the surface area, the first moment of inertia, and the moment of twist of the rod cross section, respectively.

A.2 Geometric invariants of surface bound curves

Differentiating expression (III.1.5) for the director $\boldsymbol{d}_3$ with respect to the Lagrangian coordinate s, the following expression is obtained

$$\boldsymbol{d}_3' = \alpha\,\alpha'\,\boldsymbol{d}_3 + \alpha^{-1}\left(\boldsymbol{\mathcal{S}}_{uu}u'^2 + 2\,\boldsymbol{\mathcal{S}}_{uv}u'\,v' + \boldsymbol{\mathcal{S}}_{vv}v'^2 + \boldsymbol{\mathcal{S}}_u u'' + \boldsymbol{\mathcal{S}}_v v''\right), \tag{A.2.1}$$

such that, upon projection on the unit normal to the constraint surface, we have

$$\kappa_n = \alpha^{-1}\boldsymbol{d}_3'\cdot\boldsymbol{N}, \tag{A.2.2}$$

$$= \alpha^{-2}\left(\boldsymbol{\mathcal{S}}_{uu}\cdot\boldsymbol{N}\,u'^2 + 2\,\boldsymbol{\mathcal{S}}_{uv}\cdot\boldsymbol{N}\,u'\,v' + \boldsymbol{\mathcal{S}}_{vv}\cdot\boldsymbol{N}\,v'^2\right), \tag{A.2.3}$$

which is equivalent to definition (III.1.18) of the normal curvature.

The geodesic curvature is obtained by projecting $\boldsymbol{d}_3'$ on the unit vector $\boldsymbol{N}\times\boldsymbol{d}_3$, *i.e.*,

$$\kappa_g = \alpha^{-1}\boldsymbol{d}_3'\cdot(\boldsymbol{N}\times\boldsymbol{d}_3), \tag{A.2.4}$$

$$= -\alpha^{-1}\frac{(\boldsymbol{\mathcal{S}}_u\times\boldsymbol{\mathcal{S}}_v)}{\sqrt{E\,G-F^2}}\cdot\left(\boldsymbol{d}_3'\times\boldsymbol{d}_3\right). \tag{A.2.5}$$

From equations (A.2.1) and (III.1.5), we have

$$\begin{aligned}\alpha^2\left(\boldsymbol{d}_3'\times\boldsymbol{d}_3\right) = {}& (\boldsymbol{\mathcal{S}}_{uu}\times\boldsymbol{\mathcal{S}}_u)\,u'^3 + (\boldsymbol{\mathcal{S}}_{vv}\times\boldsymbol{\mathcal{S}}_v)\,v'^3 + (2\,\boldsymbol{\mathcal{S}}_{uv}\times\boldsymbol{\mathcal{S}}_u + \boldsymbol{\mathcal{S}}_{uu}\times\boldsymbol{\mathcal{S}}_v)\,u'^2v' \\ & + (2\,\boldsymbol{\mathcal{S}}_{uv}\times\boldsymbol{\mathcal{S}}_v + \boldsymbol{\mathcal{S}}_{vv}\times\boldsymbol{\mathcal{S}}_u)\,u'v'^2 + (\boldsymbol{\mathcal{S}}_u\times\boldsymbol{\mathcal{S}}_v)\,(u''v' - u'v''),\end{aligned} \tag{A.2.6}$$

such that

$$\begin{aligned}\alpha^2\,(\boldsymbol{\mathcal{S}}_u\times\boldsymbol{\mathcal{S}}_v)\cdot\left(\boldsymbol{d}_3'\times\boldsymbol{d}_3\right) = {}& (\boldsymbol{\mathcal{S}}_u\times\boldsymbol{\mathcal{S}}_v)\cdot\left[(\boldsymbol{\mathcal{S}}_{uu}\times\boldsymbol{\mathcal{S}}_u)\,u'^3 + (\boldsymbol{\mathcal{S}}_{vv}\times\boldsymbol{\mathcal{S}}_v)\,v'^3\right] \\ & + (\boldsymbol{\mathcal{S}}_u\times\boldsymbol{\mathcal{S}}_v)\cdot(2\,\boldsymbol{\mathcal{S}}_{uv}\times\boldsymbol{\mathcal{S}}_u + \boldsymbol{\mathcal{S}}_{uu}\times\boldsymbol{\mathcal{S}}_v)\,u'^2v' \\ & + (\boldsymbol{\mathcal{S}}_u\times\boldsymbol{\mathcal{S}}_v)\cdot(2\,\boldsymbol{\mathcal{S}}_{uv}\times\boldsymbol{\mathcal{S}}_v + \boldsymbol{\mathcal{S}}_{vv}\times\boldsymbol{\mathcal{S}}_u)\,u'v'^2 \\ & + \|\boldsymbol{\mathcal{S}}_u\times\boldsymbol{\mathcal{S}}_v\|\,(u''v' - u'v'').\end{aligned} \tag{A.2.7}$$

Using Gauss equations (Gray, 1996) and Lagrange identity, the coefficients of u'^3, v'^3, u'^2v', $u'v'^2$ on the righthand side of (A.2.7) may be expressed in terms of E, F, G and the Christoffel symbols (Gray, 1996)

$$(\boldsymbol{\mathcal{S}}_u\times\boldsymbol{\mathcal{S}}_v)\cdot(\boldsymbol{\mathcal{S}}_{uu}\times\boldsymbol{\mathcal{S}}_u) = -\left(E\,G-F^2\right)\Gamma^2_{11}, \tag{A.2.8}$$

$$(\boldsymbol{\mathcal{S}}_u\times\boldsymbol{\mathcal{S}}_v)\cdot(\boldsymbol{\mathcal{S}}_{vv}\times\boldsymbol{\mathcal{S}}_v) = \left(E\,G-F^2\right)\Gamma^1_{22}, \tag{A.2.9}$$

and similarly

$$(\boldsymbol{\mathcal{S}}_u \times \boldsymbol{\mathcal{S}}_v) \cdot (2\,\boldsymbol{\mathcal{S}}_{uv} \times \boldsymbol{\mathcal{S}}_u + \boldsymbol{\mathcal{S}}_{uu} \times \boldsymbol{\mathcal{S}}_v) = \left(E\,G - F^2\right)\left(\Gamma^1_{11} - 2\,\Gamma^2_{12}\right), \tag{A.2.10}$$

$$(\boldsymbol{\mathcal{S}}_u \times \boldsymbol{\mathcal{S}}_v) \cdot (2\,\boldsymbol{\mathcal{S}}_{uv} \times \boldsymbol{\mathcal{S}}_v + \boldsymbol{\mathcal{S}}_{vv} \times \boldsymbol{\mathcal{S}}_u) = -\left(E\,G - F^2\right)\left(\Gamma^2_{22} - 2\,\Gamma^1_{12}\right). \tag{A.2.11}$$

Substituting equations (A.2.7–A.2.11) into (A.2.5), the definition (III.1.13) of the geodesic curvature is recovered.

The geodesic torsion is obtained by projecting $\boldsymbol{N}'$ on the unit vector $\boldsymbol{N} \times \boldsymbol{d}_3$, that is

$$\tau_g = -\alpha^{-1}\boldsymbol{N}' \cdot (\boldsymbol{N} \times \boldsymbol{d}_3), \tag{A.2.12}$$

with

$$\begin{aligned}\boldsymbol{N}' = {} & \frac{1}{\sqrt{E\,G - F^2}}\left[(\boldsymbol{\mathcal{S}}_{uu} \times \boldsymbol{\mathcal{S}}_v)\,u' + (\boldsymbol{\mathcal{S}}_{uv} \times \boldsymbol{\mathcal{S}}_v)\,v' + (\boldsymbol{\mathcal{S}}_u \times \boldsymbol{\mathcal{S}}_{uv})\,u' + (\boldsymbol{\mathcal{S}}_u \times \boldsymbol{\mathcal{S}}_{vv})\,v'\right] \\ & + \frac{\left(E\,G - F^2\right)'}{\left(E\,G - F^2\right)^{3/2}}(\boldsymbol{\mathcal{S}}_u \times \boldsymbol{\mathcal{S}}_v).\end{aligned} \tag{A.2.13}$$

Hence, we have

$$\begin{aligned}\sqrt{E\,G - F^2}\boldsymbol{N}' \cdot (\boldsymbol{N} \times \boldsymbol{d}_3) = {} & (\boldsymbol{\mathcal{S}}_{uu} \times \boldsymbol{\mathcal{S}}_v) \cdot (\boldsymbol{N} \times \boldsymbol{d}_3)\,u' + (\boldsymbol{\mathcal{S}}_{uv} \times \boldsymbol{\mathcal{S}}_v) \cdot (\boldsymbol{N} \times \boldsymbol{d}_3)\,v' \\ & + (\boldsymbol{\mathcal{S}}_u \times \boldsymbol{\mathcal{S}}_{uv}) \cdot (\boldsymbol{N} \times \boldsymbol{d}_3)\,u' + (\boldsymbol{\mathcal{S}}_u + \boldsymbol{\mathcal{S}}_{vv}) \cdot (\boldsymbol{N} \times \boldsymbol{d}_3)\,v',\end{aligned} \tag{A.2.14}$$

where the coefficients of u' and v' read

$$\begin{aligned}(\boldsymbol{\mathcal{S}}_{uu} \times \boldsymbol{\mathcal{S}}_v) \cdot (\boldsymbol{N} \times \boldsymbol{d}_3) &= e\,(\boldsymbol{\mathcal{S}}_v \cdot \boldsymbol{d}_3) - (\boldsymbol{\mathcal{S}}_{uu} \cdot \boldsymbol{d}_3)\,(\boldsymbol{\mathcal{S}}_v \cdot N), \\ &= \alpha^{-1} e\,(F\,u' + G\,v'), \end{aligned} \tag{A.2.15}$$

$$\begin{aligned}(\boldsymbol{\mathcal{S}}_{uv} \times \boldsymbol{\mathcal{S}}_v) \cdot (\boldsymbol{N} \times \boldsymbol{d}_3) &= f\,(\boldsymbol{\mathcal{S}}_v \cdot \boldsymbol{d}_3) - (\boldsymbol{\mathcal{S}}_{uv} \cdot \boldsymbol{d}_3)\,(\boldsymbol{\mathcal{S}}_v \cdot \boldsymbol{N}), \\ &= \alpha^{-1} f\,(F\,u' + G\,v'), \end{aligned} \tag{A.2.16}$$

$$\begin{aligned}(\boldsymbol{\mathcal{S}}_u \times \boldsymbol{\mathcal{S}}_{uv}) \cdot (\boldsymbol{N} \times \boldsymbol{d}_3) &= (\boldsymbol{\mathcal{S}}_u \cdot \boldsymbol{N})\,(\boldsymbol{\mathcal{S}}_{uv} \cdot \boldsymbol{d}_3) - f\,(\boldsymbol{\mathcal{S}}_u \cdot \boldsymbol{d}_3), \\ &= -\alpha^{-1} f\,(E\,u' + F\,v'), \end{aligned} \tag{A.2.17}$$

$$\begin{aligned}(\boldsymbol{\mathcal{S}}_u \times \boldsymbol{\mathcal{S}}_{vv}) \cdot (\boldsymbol{N} \times \boldsymbol{d}_3) &= (\boldsymbol{\mathcal{S}}_u \cdot \boldsymbol{N})\,(\boldsymbol{\mathcal{S}}_{vv} \cdot \boldsymbol{d}_3) - g\,(\boldsymbol{\mathcal{S}}_u \cdot \boldsymbol{d}_3), \\ &= -\alpha^{-1} g\,(E\,u' + F\,v'), \end{aligned} \tag{A.2.18}$$

and the definition (III.1.19) of the geodesic torsion is recovered upon substitution of equations (A.2.14–A.2.18) into (A.2.12).

A.3 Closed elastica on the sphere

A.3.1 Components of $\boldsymbol{\varsigma}(\chi)$ in the cylindrical coordinate system

In the cylindrical coordinate system, the scaled position vector and the unit tangent to the elastica axis read $\boldsymbol{\varsigma}(\chi) = \varrho\,\boldsymbol{e}_\varrho + \zeta\,\boldsymbol{e}_\zeta$ and $\boldsymbol{\varsigma}'(\chi) = \varrho'\,\boldsymbol{e}_\varrho + \varrho\,\vartheta'\,\boldsymbol{e}_\vartheta + \zeta'\,\boldsymbol{e}_\zeta$, respectively. The constant vector $\boldsymbol{\mathcal{I}} = \mathcal{I}\,\boldsymbol{e}_\zeta$, aligned with the ζ–axis, may alternatively be decomposed in the Darboux frame $\{\boldsymbol{d}_3, \boldsymbol{N}\times\boldsymbol{d}_3, \boldsymbol{N}\}$ as

$$\boldsymbol{\mathcal{I}} = (\mathcal{M}_3 + \mathcal{F}_g)\,\boldsymbol{d}_3 - (\mathcal{F}_3 + 1)\,\boldsymbol{N}\times\boldsymbol{d}_3 + \varkappa_g\boldsymbol{N}, \tag{A.3.1}$$

since $\boldsymbol{N}\times\boldsymbol{\mathcal{F}} = \mathcal{F}_3\boldsymbol{N}\times\boldsymbol{d}_3 - \mathcal{F}_g\boldsymbol{d}_3$. Hence, projecting this vector on the scaled position vector $\boldsymbol{\varsigma}(\xi)$ leads

$$\boldsymbol{\mathcal{I}}\cdot\boldsymbol{\varsigma} = -\varkappa_g, \tag{A.3.2}$$

$$= \mathcal{I}\,\zeta, \tag{A.3.3}$$

which reduces to the relation (III.1.66.a). Alternatively, the vector product between $\boldsymbol{\mathcal{I}}$ and $\boldsymbol{\varsigma}'$ reads $\boldsymbol{\mathcal{I}}\times\boldsymbol{\varsigma}' = -\mathcal{I}\,(\varrho\,\vartheta'\,\boldsymbol{e}_\varrho - \varrho'\,\boldsymbol{e}_\vartheta)$, in the cylindrical coordinate system, or $\boldsymbol{\mathcal{I}}\times\boldsymbol{\varsigma}' = \varkappa_g\boldsymbol{N}\times\boldsymbol{d}_3 + (\mathcal{F}_3+1)\,\boldsymbol{N}$, in the Darboux frame. Therefore, taking the dot product of both expressions with the scaled position vector leads

$$(\boldsymbol{\mathcal{I}}\times\boldsymbol{\varsigma}')\cdot\boldsymbol{\varsigma} = -\mathcal{I}\,\varrho^2\,\vartheta', \tag{A.3.4}$$

$$= -(\mathcal{F}_3 + 1), \tag{A.3.5}$$

which, taking into account expression (III.1.59.c), reduces to the relation (III.1.66.b).

A.3.2 Magnitude of the constant vector

Equation (III.1.60) may be integrated to obtain

$$(\varkappa_g')^2 = C_1 - \frac{1}{4}\left(\varkappa_g^4 - 2\,\sigma\,\varkappa_g^2\right), \tag{A.3.6}$$

where C_1 is a constant of integration. As a global maximum point, χ_m, of the squared geodesic curvature $\varkappa_g^2$ is a zero of $\varkappa_g'$, this constant reads

$$C_1 = \frac{1}{4}\left(\varkappa_m^4 - 2\,\sigma\,\varkappa_m^2\right), \tag{A.3.7}$$

such that expression (A.3.6) reduces to

$$(\varkappa_g')^2 = \frac{1}{4}\left(\varkappa_m^2 - \varkappa_g^2\right)\left(\varkappa_g^2 + \varkappa_m^2 - 2\,\sigma\right). \tag{A.3.8}$$

As the term $\left(\varkappa_m^2 - \varkappa_g^2\right)$ is always non-negative, the term $\left(\varkappa_g^2 + \varkappa_m^2 - 2\,\sigma\right)$ has also to be non-negative for any $\varkappa_g^2$, that is $\varkappa_m^2 \geq \sigma$. Computing the magnitude of the constant vector $\boldsymbol{\mathcal{I}} = \boldsymbol{\mathcal{M}} - \boldsymbol{N} \times \boldsymbol{\mathcal{F}}$ is then straightforward

$$\boldsymbol{\mathcal{I}} \cdot \boldsymbol{\mathcal{I}} = \left(\varkappa_g'\right)^2 + \frac{1}{4}\left[\varkappa_g^2\left(\varkappa_g^2 - 2\,\sigma\right) + (2+\sigma)^2\right], \tag{A.3.9}$$

which, accounting for expression (A.3.8), reduces to (III.1.67).

A.4 Normal ringed surface

The first partial derivatives of the parameterization (III.2.3) read

$$\begin{aligned}\boldsymbol{\mathcal{S}}_S(S,\beta) = {} & (Q'\,\cos\beta - Q\,U_3\,\sin\beta)\,\boldsymbol{D}_1 + (Q'\,\sin\beta + Q\,U_3\,\cos\beta)\,\boldsymbol{D}_2 \\ & + [1 + Q\,(U_1\,\sin\beta - U_2\,\cos\beta)]\,\boldsymbol{D}_3, \qquad \text{(A.4.1)}\\ \boldsymbol{\mathcal{S}}_\beta(S,\beta) = {} & Q\,(-\sin\beta\,\boldsymbol{D}_1 + \cos\beta\,\boldsymbol{D}_2), \qquad \text{(A.4.2)}\end{aligned}$$

such that, defining $C_j(S,\beta) = \boldsymbol{\mathcal{S}}_S \cdot \boldsymbol{D}_j$, the second partial derivatives follow

$$\begin{aligned}\boldsymbol{\mathcal{S}}_{SS}(S,\beta) = {} & (C_1' - C_2\,U_3 + C_3\,U_2)\,\boldsymbol{D}_1 + (C_2' + C_1\,U_3 - C_3\,U_1)\,\boldsymbol{D}_2 \\ & + (C_3' - C_1\,U_2 + C_2\,U_1)\,\boldsymbol{D}_3, \qquad \text{(A.4.3)}\\ \boldsymbol{\mathcal{S}}_{\beta S}(S,\beta) = {} & -(Q'\,\sin\beta + U_3\,Q\,\cos\beta)\,\boldsymbol{D}_1 + (Q'\,\cos\beta - U_3\,Q\,\sin\beta)\,\boldsymbol{D}_2 \\ & + Q\,(U_1\cos\beta + U_2\sin\beta)\,\boldsymbol{D}_3, \qquad \text{(A.4.4)}\\ \boldsymbol{\mathcal{S}}_{\beta\beta}(S,\beta) = {} & -Q\,(\cos\beta\,\boldsymbol{D}_1 + \sin\beta\,\boldsymbol{D}_2), \qquad \text{(A.4.5)}\end{aligned}$$

and the outward pointing unit normal to the surface is given by

$$\boldsymbol{N}(S,\beta) = \frac{C_3\,(\cos\beta\,\boldsymbol{D}_1 + \sin\beta\,\boldsymbol{D}_2) - Q'\,\boldsymbol{D}_3}{\sqrt{C_3^2 + Q'^2}}. \tag{A.4.6}$$

First fundamental form Equations III.1.3 for the coefficients of the first fundamental form lead to

$$\begin{aligned}E = \boldsymbol{\mathcal{S}}_S \cdot \boldsymbol{\mathcal{S}}_S = {} & (1 + Q\,(U_1\sin\beta - U_2\cos\beta))^2 + Q^2U_3^2 + Q'^2, \qquad \text{(A.4.7)}\\ F = \boldsymbol{\mathcal{S}}_S \cdot \boldsymbol{\mathcal{S}}_\beta = {} & Q^2\,U_3, \qquad \text{(A.4.8)}\\ G = \boldsymbol{\mathcal{S}}_\beta \cdot \boldsymbol{\mathcal{S}}_\beta = {} & Q^2, \qquad \text{(A.4.9)}\end{aligned}$$

with the first partial derivatives $\boldsymbol{\mathcal{S}}_S(S,\beta) = \partial\boldsymbol{\mathcal{S}}/\partial S$ and $\boldsymbol{\mathcal{S}}_\beta(S,\beta) = \partial\boldsymbol{\mathcal{S}}/\partial\beta$ given in equations (A.4.1–A.4.2). Hence,

$$\|\boldsymbol{\mathcal{S}}_S \times \boldsymbol{\mathcal{S}}_\beta\|^2 = E\,G - F^2 = Q^2\left(Q'^2 + (1 + Q\,(U_1 \sin\beta - U_2 \cos\beta))^2\right), \tag{A.4.10}$$

and the normal ringed surface with directrix $\boldsymbol{R}(S)$ and radius function $Q(S)$ has no self-intersection if and only if $Q'(S) \neq 0$ and $1 + Q\,(U_1 \sin\beta - U_2 \cos\beta) \neq 0$. Expressing the components of the Darboux vector as $U_1(S) = \mathcal{K}\sin\Phi$ and $U_2(S) = \mathcal{K}\cos\Phi$ with the directrix curvature $\mathcal{K}$, the latter condition may be rewritten as $1 - Q\,\mathcal{K}\cos(\beta + \Phi) \neq 0$ such that, since $\cos(\beta + \Phi)$ varies between -1 and 1, there will be no self-intersection if $Q\,\mathcal{K} < 1$ and $Q' \neq 0$.

Second fundamental form The coefficients of the second fundamental form therefore read

$$\begin{aligned} e = \boldsymbol{\mathcal{S}}_{SS} \cdot \boldsymbol{N} = {} & \frac{C_3\left[(C_1' - C_2\,U_3 + C_3\,U_2)\cos\beta - (C_2' + C_1\,U_3 - C_3\,U_1)\sin\beta\right]}{\sqrt{Q'^2 + (1 + Q\,(U_1 \sin\beta - U_2 \cos\beta))^2}} \\ & - \frac{Q'\,(C_3' - C_1\,U_2 + C_2\,U_1)}{\sqrt{Q'^2 + (1 + Q\,(U_1 \sin\beta - U_2 \cos\beta))^2}}, \end{aligned} \tag{A.4.11}$$

$$f = \boldsymbol{\mathcal{S}}_{S\beta} \cdot \boldsymbol{N} = -\frac{Q\,((U_1\,\cos\beta + U_2\,\sin\beta)\,Q' + (1 + Q\,(U_1 \sin\beta - U_2 \cos\beta))\,U_3)}{\sqrt{Q'^2 + (1 + Q\,(U_1 \sin\beta - U_2 \cos\beta))^2}}, \tag{A.4.12}$$

$$g = \boldsymbol{\mathcal{S}}_{\beta\beta} \cdot \boldsymbol{N} = -\frac{Q\,(1 + Q\,(U_1 \sin\beta - U_2 \cos\beta))}{\sqrt{Q'^2 + (1 + Q\,(U_1 \sin\beta - U_2 \cos\beta))^2}}. \tag{A.4.13}$$